Pulsed Magnetic Field-Induced Twin Boundary Motion in Ni–Mn–Ga

by

Miguel Augusto Marioni

Submitted to the Department of Materials Science and Engineering
in partial fulfillment of the requirements for the degree of

Doctor of Philosophy

at the

MASSACHUSETTS INSTITUTE OF TECHNOLOGY

[June 2003]
May 2003

Author .....
Department of Materials Science and Engineering
May 21, 2003

Certified by .....
Professor Samuel M. Allen
POSCO Professor of Physical Metallurgy
Thesis Supervisor

Certified by .....
Robert C. O'Handley
Senior Research Scientist
Thesis Supervisor

Accepted by .....
Harry L. Tuller
Chairman, Department Committee on Graduate Students

Pulsed Magnetic Field-Induced Twin Boundary Motion in Ni–Mn–Ga

by

Miguel Augusto Marioni

Submitted to the Department of Materials Science and Engineering
on May 21, 2003, in partial fulfillment of the
requirements for the degree of
Doctor of Philosophy

Abstract

The magnetic field-induced strain (ferromagnetic shape memory effect — FSME) in Ni–Mn–Ga was first reported in 1996 by Ullakko et al. Since then, up to 6% FSME in single-crystal tetragonal-Ni–Mn–Ga samples has been observed in static fields, and up to 3% at 500 Hz.

The present work demonstrates 6% FSME of a Ni–Mn–Ga single crystal of $5 \times 5 \times 9.85\,\mathrm{mm}^3$ in 200 μs by application of a magnetic field pulse. It proves the feasability of actuators operating at frequencies above of 1 kHz at room temperature for this geometry, and that the actuation can be accomplished using compact, air-core Helmholtz coils operated in pulsed mode.

The eddy-current attenuation of 620 μs-long pulses in the samples tested is small, reducing the need for lamination.

The field-induced extension does not begin at the same time as the field. Part of the delay is the time that the field takes to reach the threshold level for actuation. The mass-inertia of the sample results in an additional delay, which depends on the position and number of mobile twin-boundaries in the crystal. The delay is maximum for a single twin-boundary moving from the fixed to the free end of the crystal. For several twin-boundaries distributed uniformly throughout the crystal the delay is shorter. The peak acceleration observed is $50 \pm 10\,\mathrm{m/s}^2$.

For typical twin-boundary energies of the order of $40\,\mathrm{erg/cm}^2$ homogeneous nucleation of partial dislocations was found to be unlikely. Accordingly, twin-boundaries must be seeded through stress.

High-speed video images and photographs have demonstrated that field-induced twin-boundary motion is not uniform along a Ni–Mn–Ga single crystal. Twin boundaries stop when they reach certain positions of the crystal, and remain pinned unless the field is increased. The observed scatter in the data of field-induced extension is related to the existence of pinning sites.

The maximum rate of extension can be expressed as an exponential function of the driving force, and reaches 6 m/s for saturated driving force in the present case.

Thesis Supervisor: Professor Samuel M. Allen
Title: POSCO Professor of Physical Metallurgy

Thesis Supervisor: Robert C. O'Handley
Title: Senior Research Scientist

Acknowledgments

Now that the point has come to write these acknowledgements, I realize that really many people have contributed in one way or the other to this thesis. It is fair to spend perhaps more than one page acknowledging the fact.

I would first like to express my gratitude to my advisors, Samuel M. Allen and Robert C. O'Handley, for their support throughout this thesis work, for their advice, for their excellent human quality, and for caring to foster a good working environment. Thank you as well to my thesis committee, John B. Vander Sande and Yet-Ming Chiang, for their contributions in the way of thoughtful discussions and the time set aside for that. I also gratefully acknowledge the support from the Roberto Rocca Fellowship during my first semester at MIT, and from Midé Corp. (DARPA grant subcontract) and ONR (MURI grant) throughout this work. As well, I would like to take the opportunity to thank the people who encouraged me to come to MIT: Pablo Stickar, Alejandro A. Hnilo, Rubén H. Contreras, Oscar E. Martínez, Luis De Vedia, Rubén Herrera and Alberto Pignotti.

At MIT I had the privilege to interact with many really outstanding people, and this in itself has been a tremendous learning opportunity.

I wish to thank the staff at the Edgerton Center, especially Frederic P. Coté and James Bales, for their patience and advice during the construction of this work's hardware, and my UROP students, especially Afua B. Banful, and Ryan Wagar, Efrain Rodriguez and Meryl R. Del Rosario for their skilled help building a sizeable part of it and taking measurements. David C. Bono has been an invaluable help with the electronics, and I am grateful for that. I am also grateful to Douglas Matson and Anacleto de Figueredo, Yin-Lin Xie, Timothy McClure, and Ariel Martínez for their help with the equipment I used during earlier parts of this work, and to the staff of Adaptamat, especially Emmanouel Pagounis for supplying the Ni–Mn–Ga crystal that most of this work was based on.

My colleagues in the lab deserve a page aside in these acknowledgements. They have been extremely helpful in practical matters, made many interesting discussions

possible, and contributed to making the Magnetic Materials Group such an enriching work environment: Bradley W. Peterson, Marc L. Richard, Jorge Feuchtwanger, Christopher P. Henry, Elizabeth S. Lyons, David C. Bono, David I. Paul, J. K. Huang, Lirong Zheng, Ryoji Hayashi, Hans Nembach, Xue-Jun Jin, Kee-Ahn Lee, Pablo García-Tello, Katherine A. Jenkins, Kelli A. Griffin, Julee Hong, Steven J. Murray and Fernando Castaño. Many thanks!

I would not have been able to navigate the paperwork maze that is a part of academic life without the incredible efficiency and kindness of Gloria Landahl, Ann Jacobi, Kathy Farrell and Angelita Mireles at DMSE. And Rachel Kemper, Robin Lippincott and Jizhao Ma saved me many headaches with their work at the group's office: thank you!

A great many friends here and abroad provided the extra bit of support and motivation when I needed it. I wish to thank you, friends, and I hope you know how much I appreciate your support. And last, but not least, I wish to thank my family, my siblings and my parents especially, to whom this work is dedicated, for their continuous and unconditional support.

When I leave MIT, I will take with me the image of a large number of people who have perhaps contributed more to my formation than all the books on my bookshelves and lectures I've taken. This has been a true learning experience, and I am very happy to have known you all.

Miguel A. Marioni

Cambridge, MA — May 22, 2003

Contents

List of Figures

List of Tables

Chapter 1

Introduction

1.1 The Ni–Mn–Ga ferromagnetic shape memory alloy

Ni_2MnGa is an intermetallic compound of the Heusler structure [1] at temperatures below 1071 K [2]. Ni–Mn–Ga is magnetic like most Heusler structures. Specifically, it is ferromagnetic below a Curie temperature of 379 K [1, 3], and has a magnetization comparable to that of Ni [4, 5] at $4.17\,\mu_B$ per Ni_2MnGa [6]. The saturation magnetization has been shown to reside mostly on the Mn atom [7] (a non-magnetic species in pure metallic form) contrary to what was suggested in the first reports on the subject [1]. $3.36\,\mu_B$ are associated to each Mn atom, and $0.37\,\mu_B$ to each Ni atom (Ga is shown to have a small negative contribution.)

Upon cooling, Ni–Mn–Ga exhibits one or more phase transitions [8–16], and in particular a martensitic transformation [17–21]. The martensitic transformation is generally a condition for the existence of the shape memory effect, because of its diffusionless nature [22], and the fact that it is usually accompanied by a lowering in symmetry [23]. It was recognized that Ni–Mn–Ga could exhibit the shape-memory effect, a possibility that was studied and confirmed in 1993 [21].

The shape-memory effect is driven by the heat flow that is required to induce the necessary phase changes in the shape-memory material. This process is necessarily

slow, especially on cooling, placing important limitations on the use of ordinary shape memory alloys as actuator materials[1]. Ullakko et al. [24,25] and later James et al. [26] realized that the co-occurrence in Ni–Mn–Ga of ferromagnetism and a martensite phase had the potential for magnetic field-induced actuation. This would represent a major advantage over conventional shape-memory alloys, because the upper frequency bound of actuation can be shifted to higher frequencies in this case.

Although the mechanism of actuation [27] was not fully understood, Ullakko et al. [19,28] and Murray et al. [29] succeeded demonstrating a magnetic field-induced strain of 0.2%, which surpassed the strain of the giant magnetostrictor Terfenol-D[2] (0.17%.) The result was remarkable, not only because of the strain level achieved, but because of the manufacturing advantages[3] that Ni–Mn–Ga presents over Terfenol-D.

O'Handley [30] provided an insightful model that described the different driving forces that play a role in field-induced strain in Ni–Mn–Ga. James et al. [31] also showed the existence of a low-energy path connecting the field-induced strain states of the ferromagnetic shape memory alloy. Since then, the development of off-stoichiometry Ni–Mn–Ga single crystals has produced record strains for field-driven actuator materials. In 1999 0.3% strain was reported by Wu et al. [32], 1.3% by Tickle et al. [33], 4% by James et al. [34], 4.3% by Tickle et al. [35]. In 2000 5% and 5.1% were reported by Heczko et al. [36,37], 5.7% by Murray et al. [38] and 6% again by Murray et al. [39,40], almost reaching the theoretical maximum of 6.2% at compositions around $Ni_{50}Mn_{28}Ga_{22}$. A record 9.5% was recently obtained in orthorhombic, 7-layered[4] Ni–Mn–Ga by Sozinov et al. [42].

Research of Ni–Mn–Ga progressed as well in the study of cyclic field-induced strain. 0.5% cyclic strain was reported by James et al. [34] in 1999, and more recently by Henry et al. [43], who showed 6% cyclic field-induced strain in an AC magnetic field of 4kOe.

[1] Actuation at frequencies higher than a few Hz is ruled out except for micro-devices.

[2] A commercially available magnetostrictor, $Fe_2Dy_xTb_{1-x}$.

[3] The Growth of Ni–Mn–Ga crystals has higher yield and is less expensive to produce than Terfenol-D. In addition, Ni–Mn–Ga is not as brittle as Terfenol-D. These are definite advantages for actuator design.

[4] See [41].

In summary, the development of Ni–Mn–Ga as an actuator material is well advanced, and commercial applications are beginning to appear, most notably by Adaptamat of Finland [44–46].

1.2 Motivation for this work

Research on the Ni–Mn–Ga ferromagnetic shape memory alloy was driven largely by the promise of its use as an actuator material with outstanding strain performance and good frequency response.

While there is extensive reference to the magnitude of the field-induced strain in Ni–Mn–Ga, much work remains to be done to understand the dynamic response of twin-boundaries to magnetic fields. Recent work by Glavatska et al. [47] fits the relaxation of the strain induced by the application of a step-like magnetic field in single crystals with functions that approach a saturation value exponentially with time. Characteristic times for this relaxation of the order of 13 min have thus been reported. The dynamic actuation of Ni–Mn–Ga was studied in the aforementioned work by Henry et al. [43]. In the latter case, an AC-magnetic field was used in a 250 W electromagnet[5] with a laminated iron core and up 280 wire turns. The large inductance of the coil limited the frequency at which fields of the necessary intensity[6] could be applied with the power-supplies available. The study of the dynamic properties of Ni–Mn–Ga was thus limited to drive frequencies of 120 Hz [48], and to somewhat higher frequencies (250 Hz) at lower fields.

One motivation for the present work is to overcome the limitations on magnetic driving frequency imposed by the coil inductance, in order to test the performance of Ni–Mn–Ga at frequencies in excess of 1 kHz. The immediate outcome of a result would be the demonstration of the feasibility of Ni–Mn–Ga-based actuators that operate in that frequency range. This is an important point, inasmuch as the biggest challenges perhaps faced by research in the field of ferromagnetic shape memory alloys is the

[5] A 5 kW power-supply drives the magnet, which has 250 W resistive losses.
[6] About 6 kOe.

development of applications.

One way to overcome the limitation imposed by the field-generation is to apply magnetic field pulses, which can be achieved with relative ease by the discharge of a capacitor over a coil of low inductance, and is the method selected in the present work. If the pulse length is short enough its spectral decomposition will cover a wide frequency range with appreciable amplitudes, particularly at the high frequencies of interest. One caveat is the non-linearity in the field-dependence of the driving force, which of course precludes a direct comparison between the pulsed- and AC-field actuation of Ni–Mn–Ga.

The capability of applying short (sub-ms) pulses to Ni–Mn–Ga opens the field to studies of its response mechanisms at time scales characteristic of the kHz-range of actuation, and is a second motivation for this work. This is of interest to the designer of Ni–Mn–Ga-based actuator devices, particularly because applications with medium to high bandwidth requirements crucially depend on the ability of Ni–Mn–Ga to exhibit the ferromagnetic shape-memory effect in ms-range times. So far this frequency range has been dominated by piezo-electric materials in the high end (up to several MHz) and the magnetostrictor Terfenol-D (several kHz), all of which have limited stroke capability.

The third motivation for this work was triggered by a conversation with P. J. Ferreira, then at MIT, on the fundamental relationship between the different deformation mechanisms in metals, namely, dislocation motion, stacking fault expansion and twinning. Experiments made on carbon steel [49] show that with increasing strain rate the deformation goes from being dominated by dislocation motion to the preponderance of stacking fault formation. At very high strain rates twinning becomes the main deformation mechanism. Pulsed magnetic fields allow the possibility of studying the ferromagnetic shape memory alloy Ni–Mn–Ga over a large range of times and peak driving forces. The observation of twinning is not restricted to very large deformation rates in this case, and information about the expansion velocities of the faults that cause twinning could be obtained. Specifically, dislocation velocities as a function of driving force and driving force rates could be obtained at various tem-

peratures, and depending on the choice of crystal composition, for different Burgers vectors.

Finally, early work on high-speed video imaging of the field-induced extension of a Ni–Mn–Ga single crystal (see chapter 3) showed that the field-induced deformation mechanism in Ni–Mn–Ga does not proceed uniformly or at velocities that are monotonic with the driving force, prompting a closer study of the nature of these effects.

1.3 Properties of Ni–Mn–Ga

1.3.1 Structure

Ni–Mn–Ga is an intermetallic compound that has the Heusler structure. This structure has the $Fm\bar{3}m$ symmetry when it fully develops the $L2_1$ ordering in the stoichiometric compound which can be seen in Fig. 1-1. In it atoms take on the following positions:

- Ni atoms occupy $(\frac{1}{4}, \frac{1}{4}, \frac{1}{4})$ and $(\frac{1}{4}, \frac{1}{4}, \frac{3}{4})$ positions plus the positions required by symmetry;
- Mn atoms occupy $(\frac{1}{2}, 0, 0)$ positions plus the positions required by symmetry;
- Ga atoms occupy $(0, 0, 0)$ positions plus the positions required by symmetry.

At high temperatures (above 800°C in the stoichiometric compound [2]) the compound can adopt the $B2$ structure, which is like the structure of Fig. 1-1 but with Mn–Ga disorder.

Ni–Mn–Ga is used as a shape-memory material at compositions slightly off the stoichiometric Ni_2MnGa, generally near $Ni_{50}Mn_{28}Ga_{22}$ [51]. This requires the ordering apparent in Fig. 1-1 to be imperfect.

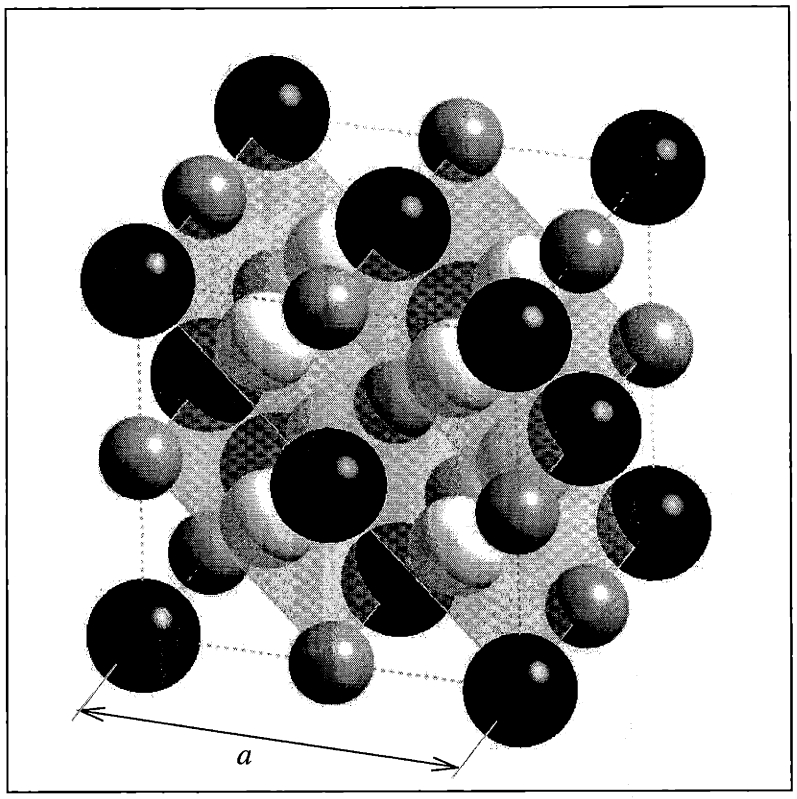

Figure 1-1: $Fm\bar{3}m$ structure of martensitic Ni–Mn–Ga. The white spheres represent nickel atoms, the gray ones manganese, and the black ones gallium. The lattice constant is 5.825 $\AA$ [6,50]. In the figure the (202) planes are indicated as gray planes. After the cubic to tetragonal distortion of the martensitic transformation, which amounts to compressing the above lattice vertically (and expanding it horizontally), these $\{202\}$ planes become twin planes, with $\langle\bar{1}01\rangle$ twinning directions.

1.3.2 Martensitic transformation

Upon cooling, Ni–Mn–Ga exhibits a *martensitic transformation.* This transformation is characterized by being a first order, shear-dominant, lattice-distortive, diffusionless transformation [23]. As a result of the transformation the lattice undergoes a distortion[7] whereby it looses symmetry. In the samples studied in this work, the transition is from cubic to tetragonal ($Fm\bar{3}m \rightarrow I\,4/mmm$), and a schematic of it can be seen in Fig. 1-2. The ratio of the c axis over the a axis (the *tetragonality* γ)

[7]This is referred to as *Bain* strain.

goes from 1 to 0.94 [52].

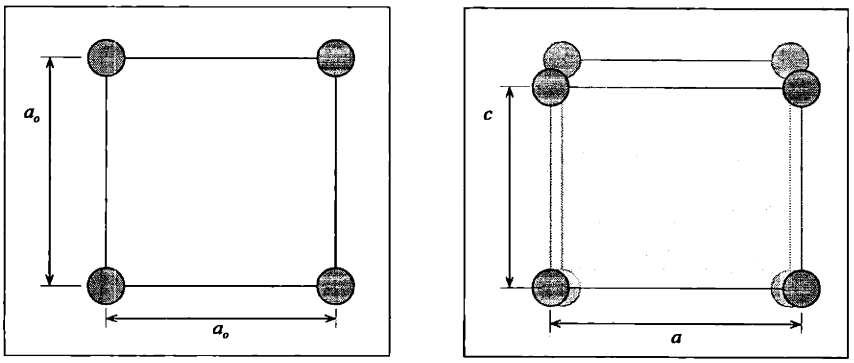

(a) (b)

Figure 1-2: Distortion of a unit cell of austenite upon cooling through the martensitic transformation temperature. (a) At high temperature Ni–Mn–Ga is in the austenitic phase, where it has the $Fm\bar{3}m$ symmetry. Its lattice constant is a_o. (b) Upon cooling, the austenite unit cell undergoes a tetragonal distortion (Bain strain) and the cubic symmetry is broken. One lattice constant becomes c and the other two become a.

In the cubic to tetragonal transformation this work is concerned with, there are three possible $\langle 001 \rangle$ axes of the austenite cell that could become the martensite c axis with the transformation. Accordingly, there will be three different orientations for the tetragonal martensitic cell. These are called martensite *variants* [2, 33, 53].

A variety of methods exist to measure the martensitic transition temperatures. Differential scanning calorimetry[8] and resistivity measurements have been employed extensively [21, 55, 56]. Another convenient way to detect the martensitic transformation is by measuring the low-field magnetization (or equivalently, the low-field susceptibility.)

In Fig. 1-3 sample curves of magnetization vs. temperature for two polycrystalline Ni–Mn–Ga samples can be seen. It can be seen that as the temperature is lowered the magnetization rises quickly below the Curie temperature (T_c) in the cubic symmetric state, called *austenite*. In Fig. 1-3(a) it is seen that the magnetization undergoes a sharp decrease upon continued lowering of the temperature for low-intensity fields,

[8]This method has the draw-back that temperature calibration on cooling can be complicated by nucleation of the reference material (usually In, Zn) [54].

and increases sharply (but less noticeably) for high intensity fields (Fig. 1-3(b).) The temperature at which this happens is the martensite start temperature T_m^s. The transformation does not happen at exactly one temperature. Instead it takes place over a range from T_m^s to T_m^f (the martensite finish temperature.)

The difference between the observed behaviors at low and high fields can be explained by considering the increase in the magnetocrystalline anisotropy resulting from the lattice distortion during the austenite to martensite transformation. In the cubic to tetragonal transformation, the c axis shortens and [001] becomes a magnetic easy axis. At weak field the cubic austenitic cells will distort in mostly random fashion, with no preferential alignment of the easy axis resulting. Consequently, a large fraction of the crystallites will have easy axes misaligned with the field, and because the field is weak, the magnetization will be aligned with the easy axis, eventually away from the field direction. Therefore, the magnetization will drop for the martensite.

When the field is strong, however, the martensitic transformation will yield variants with easy axes that are on average more closely aligned with the field. This means that a larger fraction of the magnetic moments will be aligned with the field and contributing to the overall magnetization. Further, the field can be strong enough to rotate the magnetic moments away from their easy axes and parallel to itself. Therefore, even if (because of other constraints) some variants do not have the easy axis aligned with the field, they will not diminish the magnetization signal.

1.3.3 Actuation mechanism

Twinning

The occurrence of multiple martensite variants concurrently with the loss of cubic symmetry is related to the fact that twinning becomes the preferred deformation mechanism[9]. Figure 1-4 compares two martensite cells with the result of having a

[9]This is so in Ni–Mn–Ga, but not necessarily in other alloy systems. For example in steels and ferrous alloys (eg. Fe–Ni–Co–Ti and Fe–Ni–C) the martensitic transformation can give rise to a variety of morphologies (lath-like, butterfly, thin plate, etc. — see [23]), some of which do not have twinning as the preferred deformation mechanism. It is generally considered that the thin-plate morphology is a sine-qua-non condition for twinning, and thus for the shape memory effect.

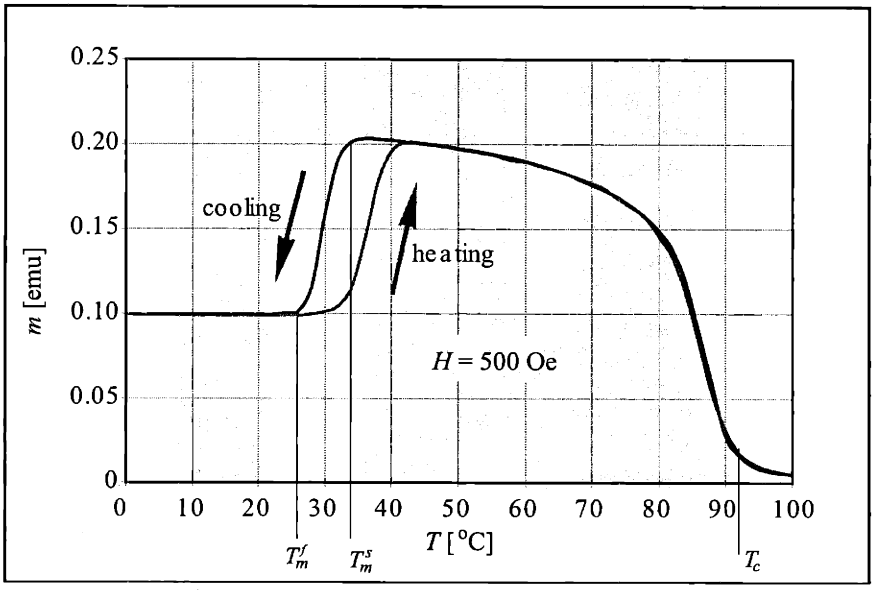

(a)

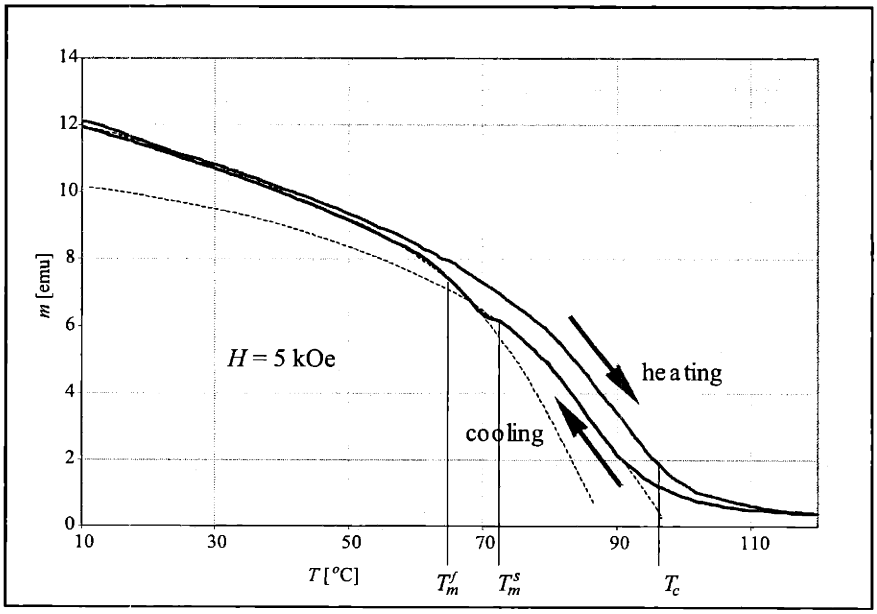

(b)

Figure 1-3: magnetization vs. temperature curves for two polycrystals at two field-levels. The direction of the temperature change is indicated with the arrows (it starts with cooling). (a) 500 Oe field-magnetization for a poly-crystal of Ni–Mn–Ga of composition $Ni_{50}Mn_{29}Ga_{21}$ (courtesy M. L. Richard, 2001.) (b) 5000 Oe field-magnetization for a poly-crystal of Ni–Mn–Ga of composition $Ni_{47}Mn_{32}Ga_{20}$ (courtesy J. Feuchtwanger and R. Ivester, 2002.) The dotted line indicates the magnetization expected in the absence of one of the phases. It is apparent that the low-field curve is better suited for the determination of the martensitic transition temperatures (as well as the Curie temperature.)

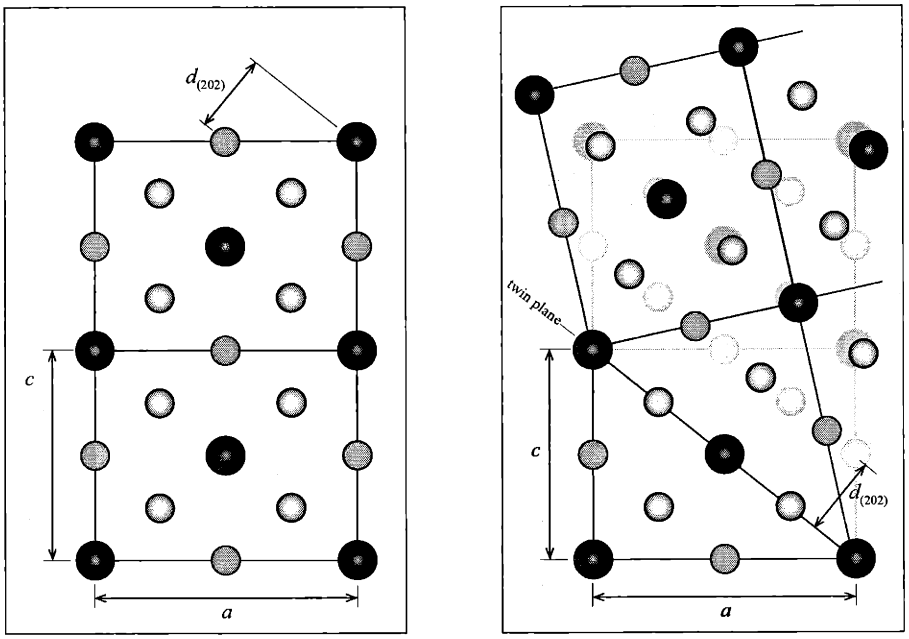

(a) (b)

Figure 1-4: This schematic is a [010] view in the notation of $Fm\bar{3}m$ of two unit cells of martensite. The white circles represent Ni atoms, the gray circles Mn atoms and the black circles Ga atoms. (a) Undistorted cells. (b) A twin-boundary formed through one of the unit cells.

twin plane pass through one of them.

Consider a planar view of a Ni–Mn–Ga unit cell, as shown in Fig. 1-5(a). A fraction of the martensite unit cell is chosen, with a long side $a/2$ and a short side $c/2$. Consider the vertex A of the tetragonal cell of the figure, and the cell diagonal parallel to $\hat{t}$, which has a normal $\hat{n}$. The vertex A does not have a mirror symmetric counterpart on the other side of the cell diagonal. However, a shift by the appropriate amount in direction of $\hat{t}$ brings it to point A' which is mirror symmetric to the opposite corner of the cell, A''.

The shift can be described by the angle Φ of Fig. 1-5. Its length b is the Burgers vector of a partial dislocation that, if expanded, would shift the entire plane (containing point A.) It is easy to see that the shift could be applied on successive planes, and have a magnitude proportional to $\tan\Phi$ in the figure. Thus the deformation would constitute a pure shear, the *twinning shear* ϵ_o. The direction $\hat{n}$ is the twin plane normal[10], and the direction $\hat{t}$ is the twinning direction.

The numerical values of b and ϵ_o are related to the twin plane distance $d_{(202)}$, and the lattice constant a:

$$\begin{aligned} d_{(202)} &= c\cos\beta = a\gamma(1+\gamma^2)^{-1/2} \\ \epsilon_o &\equiv \tan\Phi = (1-\gamma^2)/(2\gamma) \\ b &\equiv d_{(202)}\sin\phi = a\sqrt{1-\gamma^2} \end{aligned} \tag{1.1}$$

Notice that in literature the expression $\epsilon_o = 1-\gamma$ is often seen[11]. This expression coincides with Eq. (1.1) to first order in $1-\gamma$.

Coupling between the magnetic field and the crystal

The twinning deformation provides one requirement for the existence of the ferromagnetic shape memory effect. The other involves the coupling of the mechanical shear

[10]The twin plane is also called first invariant plane. The angle Φ defines the orientation of a plane (corresponding to the segment $\overline{AO}$ of the figure) which is left undistorted after the shear (it becomes $\overline{A'O}$), and is customarily called the second invariant plane.

[11]The difference is that this latter definition is not purely a strain, but also includes a rotation.

to a magnetic field, which is governed by the magnetocrystalline anisotropy K_u, a measure of the work required to turn the magnetization away from the easy axis. Figure 1-6 shows how the twinning shear and the consequent creation of a mirror symmetric version of the original lattice also implies a change in the magnetic easy axis.

Consequently, it is possible that the atoms in the crystal move according to the shear motion described in Fig. 1-5 in order to produce a crystal c axis (the magnetic easy axis) which is better aligned with the field. This process is the magnetic field-induced twin-boundary motion, and is the basis of the ferromagnetic shape memory effect, which is thus not to be confused with the ordinary shape memory effect. Field-induced twin-boundary motion requires the presence of both the twinning mechanism and a large magnetocrystalline anisotropy, and therefore occurs entirely in the martensitic phase.

1.4 Magnetic field-induced processes in Ni–Mn–Ga

1.4.1 Equilibrium orientation of the magnetization

The equilibrium orientation of the magnetization results from the interplay between the Zeeman and anisotropy energy, as was observed by several authors [30, 57, 58]. Consider the diagram in Fig. 1-7(b), depicting the simple case of a magnetic field applied in a direction perpendicular to the magneto-crystalline easy axis. A magnetic field $\mathbf{H}$ (for simplicity plotted perpendicular to the easy axis) exerts a torque on the magnetization vector M_s of a martensite variant. It rotates away from the easy axis direction $\hat{x}$ to a new direction given by θ under the action of this torque. In so doing it lowers the Zeeman energy U_Z but also increases the magneto-crystalline anisotropy energy U_{K_u}. The equilibrium orientation of the magnetization will be given by a the balance of the magnetic and anisotropy-torques, or equivalently, by the condition that

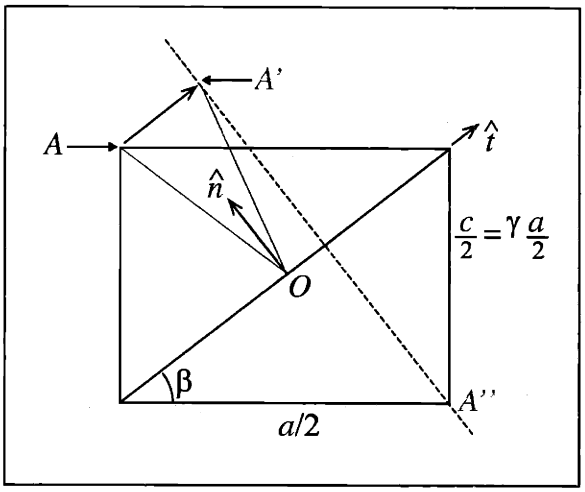

(a)

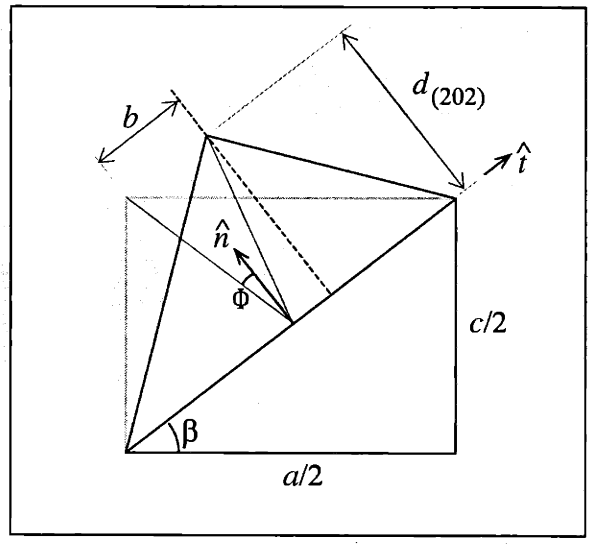

(b)

Figure 1-5: Schematic of a portion of a martensite unit cell from a [010] view in the notation of $Fm\bar{3}m$. In this notation, twinning involves a motion of Burgers vector b along the diagonal yielding a shear strain $\epsilon_o \equiv \tan\Phi$. From the graph, $\gamma \equiv c/a = \tan\beta$, so that $d_{(202)} \equiv \frac{c}{2}\cos\beta = \frac{a}{2}\gamma(1+\gamma^2)^{-1/2}$. Likewise, $\epsilon_o \equiv \tan\Phi = (1-\gamma^2)/(2\gamma)$ and $b \equiv 2d_{(202)}\sin\Phi = \frac{a}{2}\sqrt{1-\gamma^2}$.

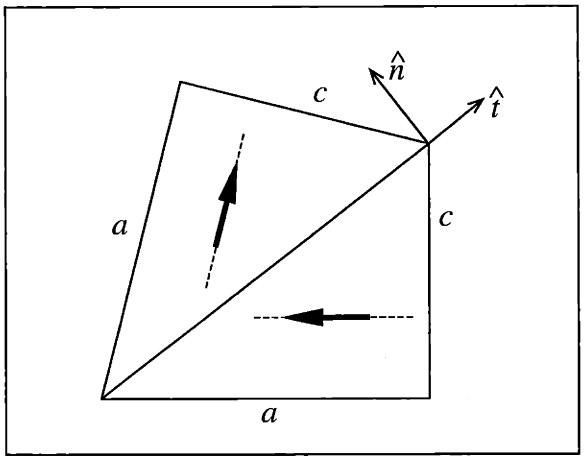

Figure 1-6: Schematic of a twinned unit cell of Ni–Mn–Ga and the change of magnetic easy axes (dashed lines) resulting from twinning. Twinning changes the orientation of the short (c) and long (a) axes of the lattice. The short axis corresponds to the easy axis in Ni–Mn–Ga. In the absence of a magnetic field the magnetic moments are aligned with the easy axes.

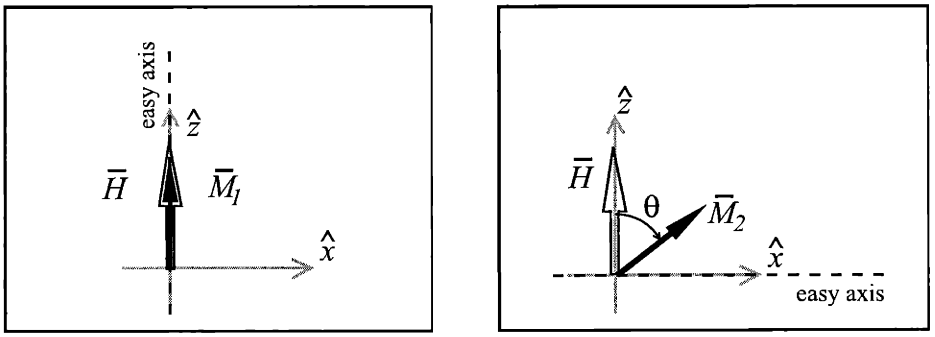

(a) (b)

Figure 1-7: A volume element of ferromagnetic shape memory alloy has a magneto-crystalline easy axis. In the absence of magnetic fields the magnetization aligns with the easy axis. A field applied parallel to the easy axis does not induce the rotation of the magnetization (a) but one applied perpendicularly to it does (b).

the sum $U_\perp$ of the Zeeman and anisotropy energy be at a minimum:

$$U_\perp = (U_Z + U_{K_u}) = -\mathbf{M_2} \cdot \mathbf{H} - K_u \left(\frac{\mathbf{M_2} \cdot \hat{x}}{||\mathbf{M_2}||} \right)^2 = -M_s H \cos\theta - K_u(1 - \cos^2\theta) \quad (1.2)$$

where from Fig. 1-7(b) $\mathbf{M_2} = M_s(\cos\theta\hat{z} + \sin\theta\hat{x})$, and $\mathbf{H} = H\hat{z}$. Here K_u stands for the Magnetocrystalline anisotropy, H is the field intensity, and M_s is the magnetization of Ni–Mn–Ga.

In the situation where a magnetic field is applied perpendicular to the easy axis of variant 2 in Ni–Mn–Ga, the angle for which $U_\perp$ is minimum defines the equilibrium orientation of the magnetic moment of 2. It is easily found that at equilibrium:

$$\cos\theta = \begin{cases} \frac{M_s H}{2K_u} & \text{if} \quad \frac{M_s H}{2K_u} \leq 1 \\ \\ 1 & \text{if} \quad \frac{M_s H}{2K_u} > 1 \end{cases} \quad (1.3)$$

prompting the definition of a *reduced field* η:

$$\eta = \frac{M_s H}{2K_u} \quad (1.4)$$

η is directly proportional to the field and is adimensional. When its value is lower than one, it is numerically equal to cosine of the angle between the magnetization the field. With this the equilibrium magnetic moment of variant 2 is quickly written as:

$$\mathbf{M_2} = \begin{cases} M_s \left(\eta\hat{z} + \sqrt{1 - \eta^2}\hat{x} \right) & \text{if} \quad \eta \leq 1 \\ \\ M_s\hat{z} & \text{if} \quad \eta > 1 \end{cases} \quad (1.5)$$

1.4.2 Driving force for twin-boundary motion

Equation (1.3) indicates that at equilibrium

$$U_{\perp}^{eq} = \begin{cases} M_s K_u (1+\eta^2) & \text{if} \quad \eta \leq 1 \\ \\ -M_s H & \text{if} \quad \eta > 1 \end{cases} \tag{1.6}$$

For the case where the magnetic field is applied parallel to the direction of the magneto-crystalline easy axis (Fig. 1-7(a)) it is easy to see that the equilibrium orientation of the magnetization *is* the easy axis. The energy can then be written in a manner analogous to Eq. (4.23):

$$U_{\parallel} = (U_Z + U_{K_u}) = -\mathbf{M}_1 \cdot \mathbf{H} - K_u \left(\frac{\mathbf{M}_1 \cdot \hat{z}}{||\mathbf{M}_1||} \right)^2 \tag{1.7}$$

which is at equilibrium when:

$$U_{\parallel}^{eq} = -M_s H - K_u \tag{1.8}$$

Note that:

$$\lim_{H \to 0} U_{\perp}^{eq} = \lim_{H \to 0} U_{\parallel}^{eq} = -K_u \tag{1.9}$$

which indicates that both $U_{\perp}$ and $U_{\parallel}$ use the same reference energy.

In ferromagnetic shape memory alloys, a twin variant 2 can be transformed into its reciprocal twin, variant 1, through the twinning shear. When this happens, the magneto-crystalline easy axes change accordingly, as is represented in Fig. 1-7. In Fig. 1-7(b), a field is applied perpendicular to the easy axis of a twin variant, called 2 for the sake of argument. A twinning shear transforms variant 2 into variant 1 and also realigns the magnetic easy axis, leading to the configuration depicted in Fig. 1-7(a).

Using Eq. (1.9) the twinning process is thus seen to be accompanied by an energy

drop of magnitude

$$\Delta G = U_{\parallel}^{eq} - U_{\perp}^{eq} = \begin{cases} -K_u(2\eta - \eta^2) & \text{if} \quad \eta \leq 1 \\ \\ -K_u & \text{if} \quad \eta > 1 \end{cases} \tag{1.10}$$

This is the driving force for twin-boundary motion. In Fig. 1-8 Eq. (1.10) is plotted in terms of the reduced field η, in units of the magnetic field K_u. Note that the driving

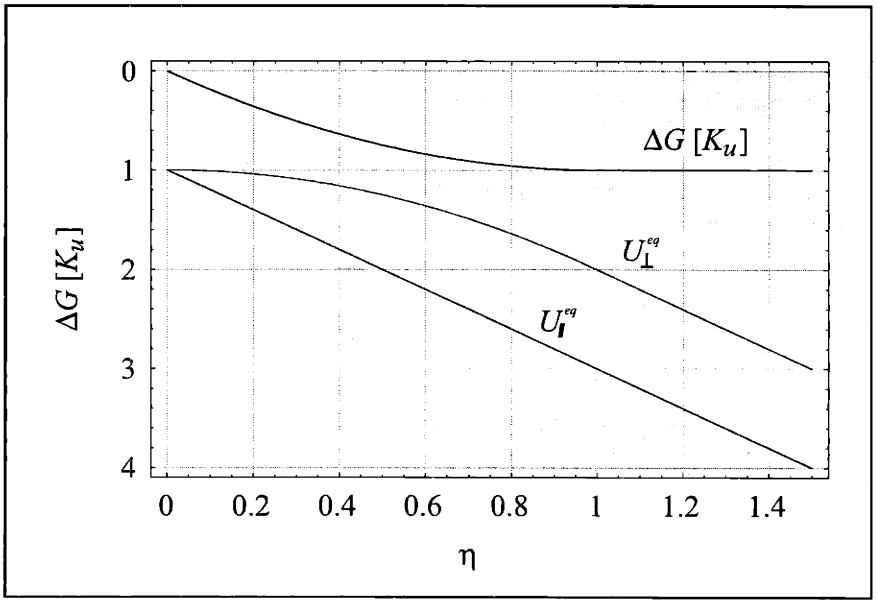

Figure 1-8: Energies for the equilibrium orientations of the magnetization, $U_{\parallel}^{eq}$ and $U_{\perp}^{eq}$ in variant 1 and 2 respectively as a function of the reduced field η in units of K_u. Also plotted is the difference between the two, which is the driving force for twin-boundary motion.

force is linear with the field for small fields. At larger field the quadratic term in H becomes more important, until saturation is reached when the reduced field η reaches 1. The field at which saturation occurs is the *saturation field*, $H_s = 2K_u/M_s$. No increase of driving force for twin-boundary motion is obtained from increasing the field beyond the saturation field.

Magnetic pressure on the twin-boundary

The driving force for twin-boundary motion can be likened to a magnetic pressure on the twin-boundary σ_m making use of the equivalence of the work done by a magnetic field and a stress to shear a portion of the Ni–Mn–Ga crystal by the twinning strain.

$$\epsilon_o \sigma_m = \Delta G \tag{1.11}$$

This expression is useful to obtain a comparison between the action of a field and a stress that produces the same result.

Chapter 2

Experiment

2.1 Setup

2.1.1 Overview

The experiment described in this work subjects a Ni–Mn–Ga single crystal to a pulsed magnetic field. Figure 2-1(a) shows a schematic view of the apparatus used. The pulsed-magnetic field is generated in an oscillating LCR-circuit where the inductance L is a Helmholtz coil (Fig. 2-1(b).) To achieve sub-millisecond probing times a special coil designed ad hoc is used (see Sec. 2.1.2.) A high-voltage power supply[1] charges up two capacitors (240 μF total capacitance) on open circuit to a programmed voltage.[2] The pulse is fired when an SCR switch[3] is closed, discharging the capacitors into the series inductance and resistance load.

A ferromagnetic shape memory alloy single crystal is placed inside the coil, and held fixed in position at one end. The other end of the crystal is free. A stabilized He-Ne laser illuminates the free end of the crystal, to which a mirror is affixed, and

[1] Bertan, Series 105.

[2] For convenience the potential difference is limited to 3000 V. A larger voltage requires a more powerful power supply, but also special capacitors able to withstand such potential differences without short-circuiting.

[3] Silicon controlled rectifier (SCR) model ABB 5stp28I4200. This diode is rated at maximum current of 52 kA (10 ms) and 3700 V, and has a critical rate of on-state current rise of 1 kA/μs.

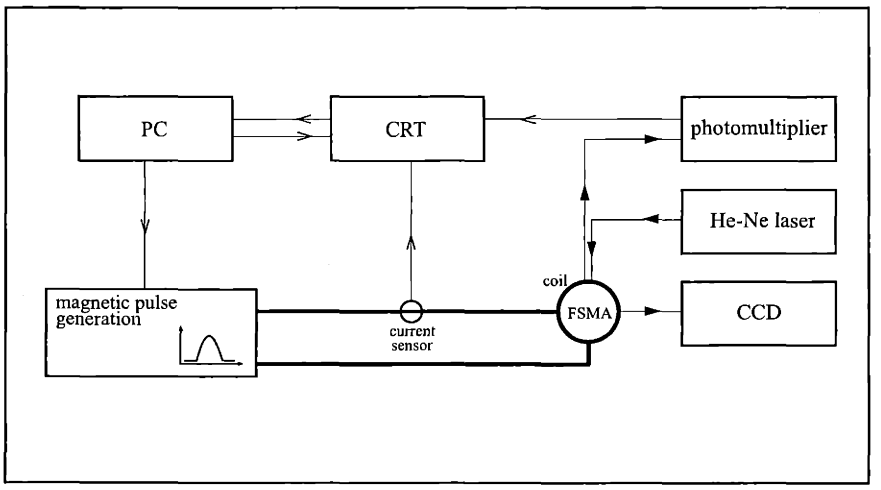

(a)

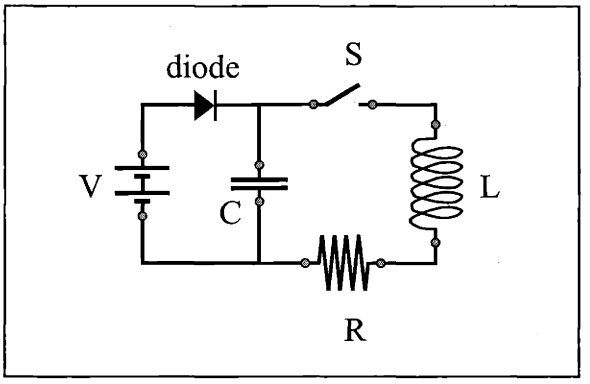

(b)

Figure 2-1: (a) Schematic of the experiment setup. A capacitor bank is charged to a programmed voltage and subsequently discharged across a Helmholtz coil, generating a magnetic field pulse. A Ni–Mn–Ga crystal is placed in the coil and its field-induced extension is detected optically. Coil current and extension signals are acquired with an oscilloscope and subsequently read. (b) Schematic of an LCR-circuit used to generate a magnetic field pulse. Typical values for the components are 240 μF of capacitance (charged up to 3000 V with the switch S open), an inductance of 0.158 mH, and resistance of about 0.195 Ω. The configuration used in the experiments here described is able to reach peak field values of 27 kOe in a magnetic field-swing lasting 620 μs.

a photo-sensitive device[4] captures the reflection. When the crystal extends the free end is displaced, and the reflection off the mirror at its end occurs in a different spot. This results in a change of the light intensity that reaches the detector, and allows inferring the displacement from a detector signal change.

Concurrently a current detector[5] placed in the LCR-circuit senses the current level, which can be related to the field inside the coil.

The detector signals can be then be acquired and digitized. It is convenient for this to use an oscilloscope[6], since it can acquire at high rates. The appropriate digital filters can then be applied to the data.

2.1.2 Magnetic coil for magnetic-field pulses

Depending on the combination of L, C and R parameters, the pulse generated will have the characteristics of an over- or under-damped system respectively. The overall resistance R of the system will be the sum of the coil's resistance and the resistance of all wires in the circuit.

Coil design

Consider the schematic in Fig. 2-2. Two coaxial loops of radius a carrying a current i and separated by a distance d will generate a magnetic field of a spatial uniformity that will depend on d and a. From this point of view the optimal configuration has $a = d$, and is usually referred to as a Helmholtz configuration. [59] Instead of single-wire loops, coils of n wires were used, henceforth referred to as sub-coils. To estimate the LCR-system's characteristics an expression for the components, inductance, capacitance and resistance is needed.

[4]This can be a photodiode or a photomultiplier (see Sec. 2.1.4.)

[5]Person Electronics current monitor mod. 4418. The detector output is 1 mV/A, and is ±1% accurate.

[6]In this experiment: HP54602B (150 MHZ) with an HP54657A interface.

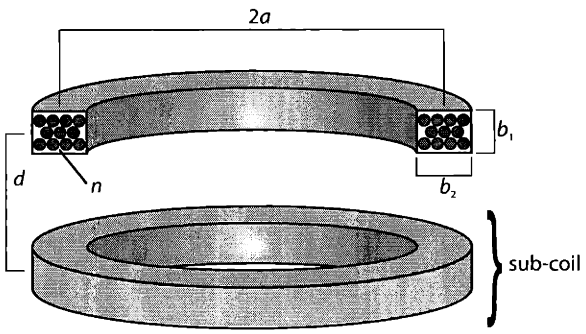

Figure 2-2: Schematic of a pair of coaxial loops or sub-coils of radius a, separated by a distance d that form a coil used for generating pulsed magnetic fields. Each loop can be replaced by a group of n loops forming a sub-coil of cross section $b_1 \times b_2$. The uniformity of the field is optimal for a choice of $d = a$. This particular configuration is called a *Helmholtz*-configuration.

Inductance

The inductance can be obtained from the expression for the inductance L_s of each identical sub-coil s and the mutual inductance M_{ss} as:

$$\begin{aligned} L &= 2L_s + 2M_{ss} = \\ &\simeq 2\frac{4an^2\pi}{c^2}\left(1 - y_1 + \frac{b^2 y_2}{16a^2} + \frac{b^2 \log(\frac{4\sqrt{2}a}{b})}{24a^2}\right) + \frac{4a\pi}{c^2}\left(\frac{5-2\sqrt{5}}{5}K - \sqrt{5}E\right) \end{aligned} \tag{2.1}$$

where n is the number of loops in each half-coil, a is the coil radius, b is the side of a square of area equal to the cross section of the half-coils, and y_1, y_2, E and K are numerical constants. A more detailed explanation of the origin of the expression for L of Eq. (2.2) as well as corrections that account for the fact that the coils are composed of n discrete wires can be found in Sec. A.1.

Resistance

The resistance of the system is the sum of the coil resistance R_c and the resistance of the leads, R_l. The former can be computed from the AWG number of the wires that compose the sub-coils simply as

$$R = (2\pi a n \rho_{coil}) \times 2 \tag{2.2}$$

where ρ_{coil} is the resistance per unit length of the wire of given AWG number. The resistance of the leads is computed in a similar way as

$$R = (l_{lead}\rho_{leads}) \times 2 \tag{2.3}$$

where l_{lead} is the length of the leads and ρ_{leads} is their resistance per unit length.

Capacitance

The capacitance of the system is capacitance of the capacitor bank. Two capacitors of 120 μF are used either in parallel or in series, so as to provide 60, 120 and 240 μF of total capacitance respectively.

Capacitor discharge

With the above values for the components of the LCR-system, it is possible to compute the current as a function of time during the capacitor discharge. The discharge is governed by Eq. (2.4) for the capacitor charge $q = q(t)$:

$$\begin{aligned} L\frac{\partial^2 q}{\partial t^2} + R\frac{\partial q}{\partial t} + \frac{1}{C}q &= 0 \\ \frac{\partial q(0)}{\partial t} &= 0 \\ q(0) &= C\,V_0 \\ q(\infty) &= 0 \end{aligned} \tag{2.4}$$

where $V(0) \equiv V_0$ was been used. The solutions to this equation are well known:

$$\begin{aligned} q(t) &= C\,V(0)\frac{\lambda_1\lambda_2}{\lambda_1 - \lambda_2}\left(e^{\lambda_1 t} - e^{\lambda_2 t}\right) \\ \lambda_{1,2} &= -\frac{1}{t_L}\left(1 \pm \sqrt{1 - \frac{{t_L}^2}{{t_C}^2}}\right) \end{aligned} \tag{2.5}$$

where for convenience one defines characteristic times

$$\begin{aligned} t_L &= 2L/R \\ t_C &= \sqrt{L\,C} \end{aligned} \tag{2.6}$$

The relative size of t_L and t_C will define the type of capacitance discharge that Eq. (2.5) describes. Three kinds of behavior can be recognized:

$$\text{if} \quad t_L < t_C \quad \text{then the system is over-damped}$$

if $t_L = t_C$ then the system is critically-damped

if $t_L > t_C$ then the system is under-damped

Here the focus is on the over- and under-damped circuits. In the former case the current i_{over} is given by:

$$i_{over} = -\frac{C\,V_0}{t_C}\,\frac{t_L/t_C}{\sqrt{1-(t_L/t_C)^2}}\,\sinh\left(\sqrt{1-\left(\frac{t_L}{t_C}\right)^2}\,\frac{t}{t_L}\right)\,e^{-t/t_L} \tag{2.7}$$

and for the under-damped system the current i_{under} will be:

$$i_{under} = -\frac{C\,V_0}{t_C}\,\frac{t_L/t_C}{\sqrt{(t_L/t_C)^2-1}}\,\sin\left(\sqrt{\left(\frac{t_L}{t_C}\right)^2-1}\,\frac{t}{t_L}\right)\,e^{-t/t_L} \tag{2.8}$$

Eqs. (2.7–2.8) allow the computation of the magnetic field at the center of the Helmholtz pair, given by:

$$H = \mu_0\left(\frac{4}{5}\right)^{\frac{3}{2}}\frac{i}{a} \tag{2.9}$$

where $i = 2n\,i_{over}$ or $i = 2n\,i_{under}$ depending on whether an over- or under-damped system is considered (n being the number of turns in each sub-coil.)

Design and experiment requirements

The choice of the coil parameters follows the following design and experiment requirements:

1. Peak magnetic fields topping 10 kOe are needed to insure that twin-boundaries will have sufficient driving force to move;

2. The pulse duration and the time to reach peak field have to be under 1 ms, because it is desired to study the regime where AC measurements are impractical [60];

and the following restrictions:

1. The peak current must not exceed 10 kA, because the components must be rated to withstand it[7];

2. The onset current-increase rate has to be smaller than the slew rate of the slowest component, in this case the silicon controlled rectifier.

Expressions for these design targets can be found from Eq. (2.7) and Eq. (2.8). One obtains for the peak current:

$$\begin{aligned} i_{over}^{peak} &= -\frac{C\,V_0}{t_C}\exp\left(-\frac{\operatorname{arccosh} t_C/t_L}{\sqrt{1-(t_L/t_C)^2}}\right) \\ i_{under}^{peak} &= -\frac{C\,V_0}{t_C}\exp\left(-\frac{\arccos t_C/t_L}{\sqrt{-1+(t_L/t_C)^2}}\right) \end{aligned} \tag{2.10}$$

The peak current is reached at time t_{over}^{peak} and t_{under}^{peak}:

$$\begin{aligned} t_{over}^{peak} &= t_L\left(\frac{\operatorname{arccosh} t_C/t_L}{\sqrt{1-(t_L/t_C)^2}}\right) \\ t_{under}^{peak} &= t_L\left(\frac{\arccos t_C/t_L}{\sqrt{-1+(t_L/t_C)^2}}\right) \end{aligned} \tag{2.11}$$

Finally, the derivative of the current at pulse onset will be:

$$\begin{aligned} \frac{di^{peak}}{dt}_{over} &= -\frac{C\,V_0}{{t_C}^2} \\ \frac{di^{peak}}{dt}_{under} &= -\frac{C\,V_0}{{t_C}^2} \end{aligned} \tag{2.12}$$

The expressions are formally the same for both over- and under-damped systems. Along with the approximation that the factor $\exp\left(-\frac{\operatorname{arccosh} t_C/t_L}{\sqrt{1-(t_L/t_C)^2}}\right)$ in the above equations can be assumed to be of the order of unity in most practical cases, the equations

[7]Most components are not rated as high, but are able to withstand short sparse pulses.

lead to the following trends:

$$\begin{aligned} i^{peak} &\propto \sqrt{\tfrac{C}{L}}\,V_0 &&\simeq C^{1/2}\,V_0\,a^{-1/2}\,n^{-1} \\ B^{peak} &\propto \tfrac{n}{a}\sqrt{\tfrac{C}{L}}\,V_0 &&\simeq C^{1/2}\,V_0\,a^{-3/2} \\ \frac{\partial B}{\partial t}(0) &\propto \tfrac{n}{a}\tfrac{V_0}{L} &&\simeq V_0\,a^{-2}\,n^{-1} \\ t^{peak} &\propto \tfrac{L}{R} &&\simeq n \end{aligned} \tag{2.13}$$

Below is a list of the parameters that can be chosen to affect the pulse characteristics:

1. The coil radius, which must be larger than 3/4" to leave room for the optics, and provide enough homogeneity over the sample length of about 9.85 $\pm$ 0.01 mm.

2. The number of turns per coil;

3. The wire gauge, ranging from AWG2 to AWG20;

4. The lead length and wire gauge. The latter is taken to be AWG2;

5. The capacitor capacitance, which can be any of $\{60, 120, 240\}\,\mu$F;

Figure 2-3 shows a comparison of experimental and calculated pulse profiles.

2.1.3 Coil materials

The coil windings were made of #15 HAPT NEMA MW 35-C copper wire (resistance = $0.0104\,\Omega\mathrm{m}^{-1}$, diameter = 1.45 mm) provided by MWS, according to the design choice for the coil.

The support for the wire windings was machined from Delrin. Besides being non-magnetic and non-conductive (and thus not coupling magnetically to the coil nor supporting induced currents) it has good stiffness and relatively light weight[8].

The coil used in the experiments of Chapter 3 is depicted in Fig. 2-4. With peak currents in excess of 3 kA loose wires tend to deform and eventually cause the coil to

[8]Some fiber-glass epoxies have better mechanical properties but are hazardous to machine.

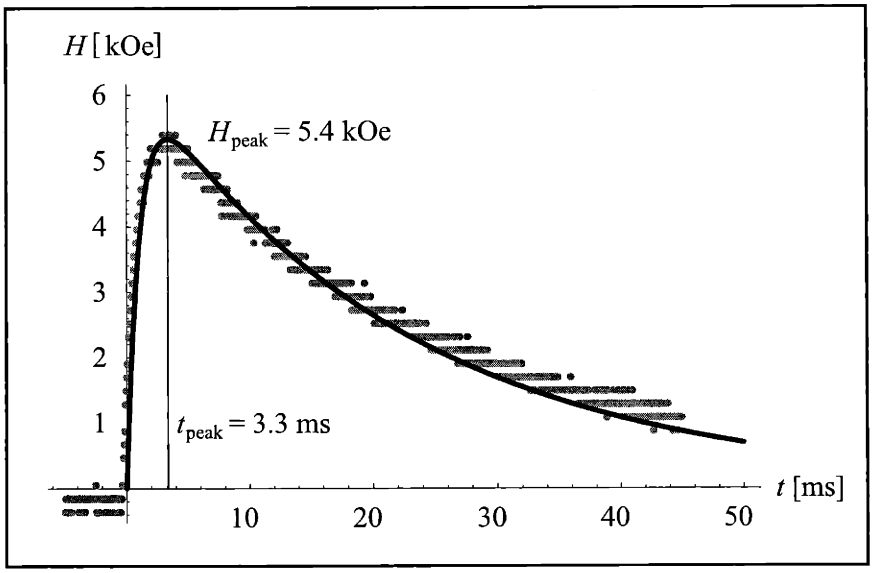

Figure 2-3: Over-damped oscillatory circuit for pulse generation: simulation and experiment. Prototype coil with $n = 25$. The gray dots correspond to measured values of the magnetic field, whereas the black line is the model result. No fitting parameters are used.

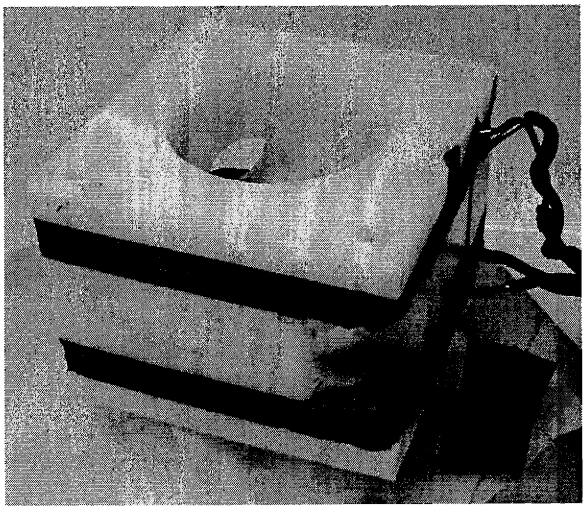

Figure 2-4: Coil used in the experiments reported in Chapter 3.

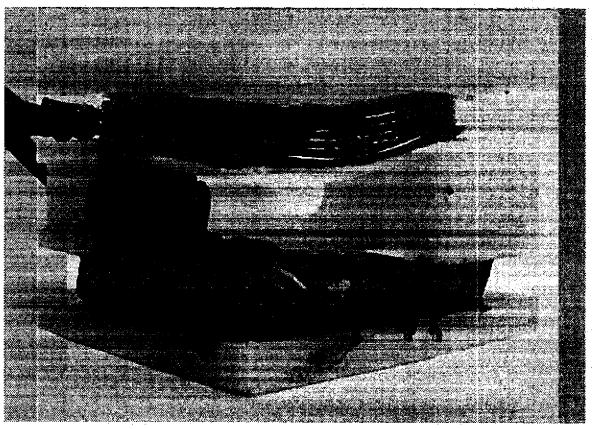

Figure 2-5: Coil prototype with windings bent by the field.

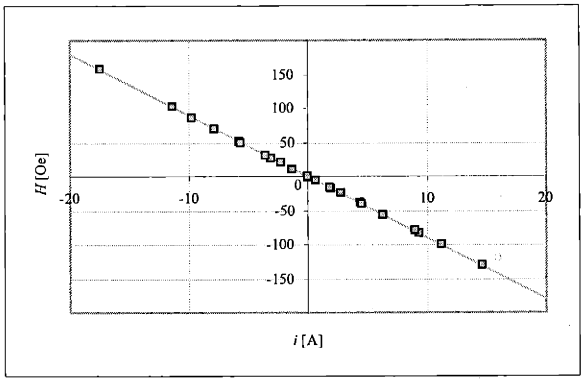

Figure 2-6: Calibration curve for the coil used in Chapter 3. It is $H = -8.94\text{Oe}\,\text{A}^{-1}i - 0.28\text{Oe}$.

break (Fig. 2-5.) Therefore, once mounted the copper windings were covered with a two-part epoxy.

Calibration

As was indicated in Sec. 2.1.1 the field is inferred from the measured value of the coil current. The coil used in Chapter 3 was calibrated at low fields, measuring the field[9] at the center of the coil with DC currents of up to 20 A. Figure 2-6 shows the calibration curve. $H = -8.94\frac{Oe}{A}i - 0.28$ was obtained.

2.1.4 Real-time detection of the crystal extension

Concept

The extension of the crystal is measured optically. Doing so has two advantages over the methods methods employed elsewhere [48, 61]. First, it allows for the sample to be free on one end, so that the driving force is purely magnetic and no stresses are applied. Second, the inertia of any measurement device that would otherwise have to be attached to the end of the sample does not affect the measurement. As reported by Henry [48] the mass of any attached device contributes to resonance frequencies in the AC measurement of the extension.

The basis of the method is indicated in Fig. 2-7. As the free end of the crystal

[9]Lakeshore 450 Gaussmeter.

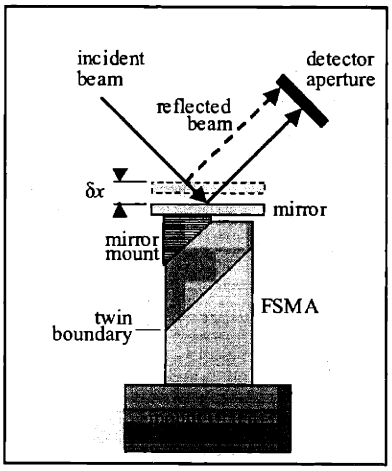

Figure 2-7: Optical measurement of the extension.

moves under the action of the magnetic field, the incident light is deflected at a different spot on the mirror and causes a different total light intensity to reach the detector aperture. Due to the small displacements involved (about 0.7 mm for a crystal length of about 9.85 $\pm$ 0.01 mm) a high sensitivity is needed. To achieve this the detector signal is amplified with a pre-amplifier[10] in differential mode. The baseline subtracted is provided by a low-noise, low-drift 16-bit DAC-voltage reference (see Sec. A.1.3) which is programmed by the position calibration software.

The accuracy of the measurement is limited by the oscilloscopes used to acquire and digitize the field and extension information (see footnote 6 on page 39), which operate with 8 bits. Therefore the detector signal must be amplified to full scale in the oscilloscope. In practice there is a limitation to ± 6 V, the linear output range of the amplifier.

Unfortunately, the relatively small magnitude of the detector signal changes implies that the measurements will be sensitive to various sources of noise.

Mechanical vibrations are thus to be avoided whenever possible. Because ultimately the signal detected depends on the relative position of sample and detector, both are sources of noise. The vibrations affecting the sample can be minimized by using massive mounts (see Fig. 2-8), and by bringing the detector closer to the mirror[11]. On the other hand the electronics of the detector are sensitive to the rapidly varying stray fields from the coil, and should be kept far from it. The problem is circumvented by using optic fibers. They are encased in a cylinder that can be moved right up to the mirror on the sample, through a hole in the coil. At the tip of the cylinder there are holes through which the fibers protrude maintaining an angle of about 90°, which gives optimal sensitivity to the extension of the sample. One fiber transmits the light from the He-Ne laser and the other one captures the reflection at a close distance from the mirror and leads the light to a shielded detector, located at a convenient distance (see Fig. 2-9.)

[10] Stanford Research, low noise preamplifier mod. # SR560.

[11] Vibrations cause the incident beam to be reflected off different angles. The displacement on the detector is thus proportional to the distance between mirror and detector.

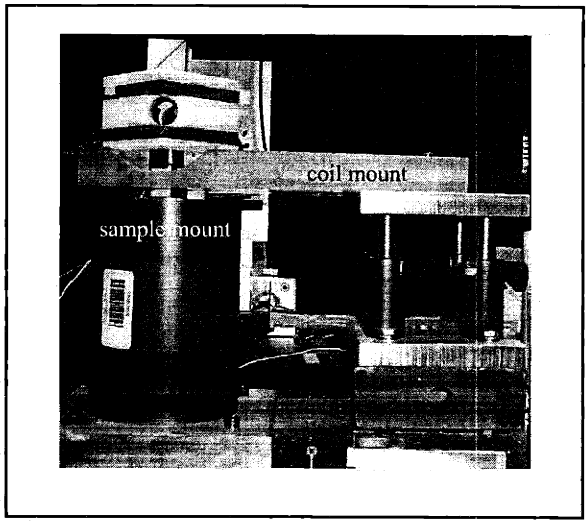

Figure 2-8: To minimize noise introduced by mechanical vibrations, the sample and the coil are mounted on separate platforms. The coil platform rests on a lead brick lying on rubber dampeners.

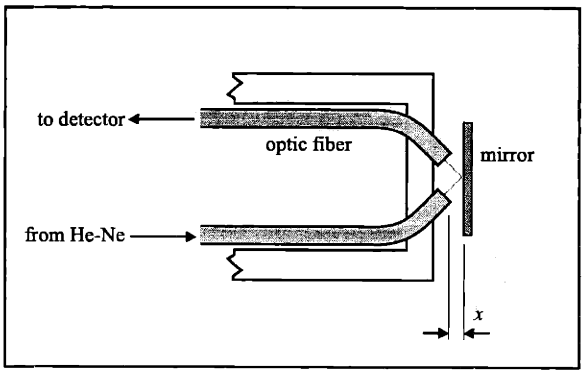

Figure 2-9: A "probe" made of two optic fibers as part of the optical extension detection apparatus. One fiber shines light from a stabilized He-Ne laser onto the mirror affixed to the sample. The reflection falls on the receiving fiber, which leads it to the detector. This configuration effectively puts the aperture of the detector very close to the sample, while keeping the electronics far from the pulsed-field disturbances.

Vibrations can also affect the optics directly on two accounts. Firstly, the plastic fibers used slightly change their transmission if bent, so the transmission of vibrations to the fibers must be avoided. This can be accomplished simply by taping the fibers to rigid mounts. Secondly, the support used to lead the fibers into the coil via the calibration stage is subject to vibrations that change the relative distance between the sample- and the fiber tip. The effect of these can be suppressed by placing the fibers and the sample holder inside a Delrin tube that connects them. In this fashion, even if vibrations are transmitted to the optics (or the sample), they do not affect the relative distance between the fibers and the mirror attached to the sample tip.

Bandwidth and detector choice

It is necessary to consider possible bandwidth limitations of the system. The preamplifier after the detector has a 4-pole 300 kHz filter at the input, to reduce most of the high frequency noise observed. This means that signal changes occurring over times much smaller than about 3 μs will not be discernible. The coaxial cables' bandwidths are not relevant, since at frequencies of 300 kHz their transmission is essentially one[12]. The oscilloscope used has a bandwidth of 150 MHz which will not be limiting. The detectors need to be considered. Photodiodes are desirable over photomultipliers, because they have a more steady output. However, they have a lower gain, and their signal needs to be amplified by larger factors. Both a photodiode and a photomultiplier have a preamplifier[13] which amplifies the signal before transmitting it to the next stage of amplification[14] and acts as a 50 Ω source impedance for the coaxial cables that are used for transmission. This implies that the coaxial cables (50 Ω, with $\tilde{3}$0 pF/foot) would start acting as filters in the GHz range, and can be neglected.

The detector preamplifiers[15] have a gain-bandwidth product (amplification factor *times* cut-off frequency) of 70 MHz. This means that increasing the amplification fac-

[12]The coaxial cables (which have a typical stray capacitance of about 30 pF/m) will have a corner frequency (-3 dB point) in the GHz range.

[13]This is at a prior stage to the preamplifier mentioned above.

[14]Therefore the noise picked up during the transmission will be smaller than the trsanmitted signal.

[15]The pre-amplifier uses a LH0032 Op-Amp from National Instruments

tor reduces the cut-off frequency. The converse is of course true. Photodiodes required too high an amplification factor, in the sense that the resulting cut-off frequencies were of the order of a few kHz. Therefore, a photomultiplier[16] was employed, with which the cut-off frequency could be maintained at about 5 MHz. Figure 2-10 shows the frequency response of the photo-multiplier plus preamplifier[17]. A flat response is observed below 5 MHz.

Calibration

Changing the distance x between the sample mirror and the tip of the optic fiber probe (see Fig. 2-7 and Fig. 2-9) produces a change in the detector signal. To avoid vibrations in the sample to the greatest extent possible, it has to be fixed firmly and not be moved it during the calibration. The change in x therefore achieved by moving the optic probe instead. This is accomplished with a stepper motor[18] attached to a micrometer stage[19] and conveniently controlled with a *Labview* program and serial port modules[20]. Schematically the detector profile over distance looks as indicated in Fig. 2-11, presenting two useful ranges. Typical calibration curves can be seen in Fig. 2-12. The effective range is controlled by changing the amplification factor at the preamplifier.

Possible signal changes caused by thermal drift of the electronics generally develops over the course of several hours, and can be minimized by allowing the equipment to thermalize overnight and measuring immediately after calibrating. A different source of drift comes from the laser intensity. Although it does not vary measurably over the course of the experiment, it could vary in the time-span between obtaining the calibration curve and triggering the pulse. The problem is alleviated by using a stabilized He-Ne laser[21].

[16]Hamamatsu R268 photomultiplier.

[17]The plot is a simulation made for illustration purposes. The measured curve coincides with the simulation in all aspects except that the measured peak is slightly higher in reality. This does not affect the flatness of the response below 10 MHz.

[18]Superior Electric M062-CS09, a synchronous stepper motor with 200 steps per revolution.

[19]Parker Positioning Systems Daedal Division 4454, 0.001 mm per division.

[20]Weeder Technologies, WTSMD-M.

[21]Melles-Griot, mod. 05-STP-911-249.

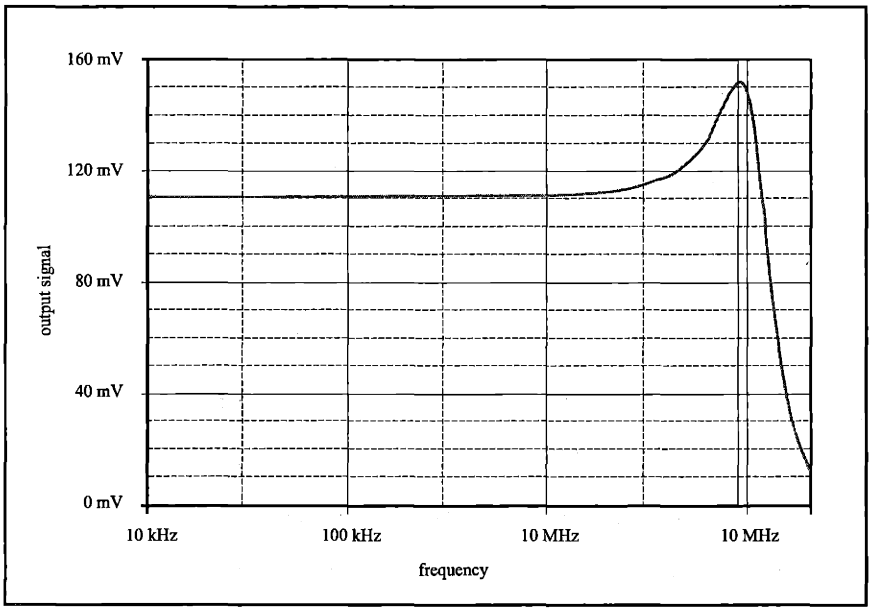

Figure 2-10: Simulation of the photo-multiplier plus preamplifier frequency response with a 10 mV input signal amplitude (courtesy D. Bono.) The measured frequency response coincided with the simulation, except for the height of the peak displayed here, which was larger in reality. The flatness of the response below 10 MHz is not affected by this fact.

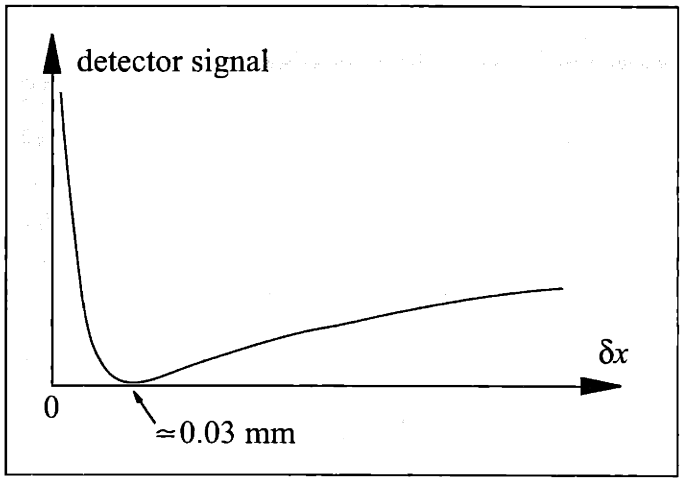

Figure 2-11: Schematic of the detector signal variation with distance between mirror and probe, δx.

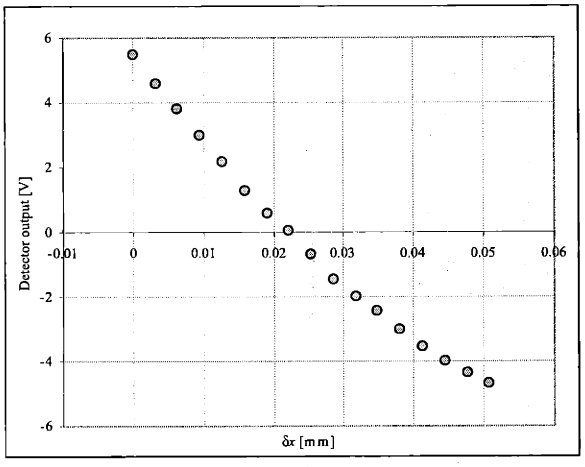

(a)

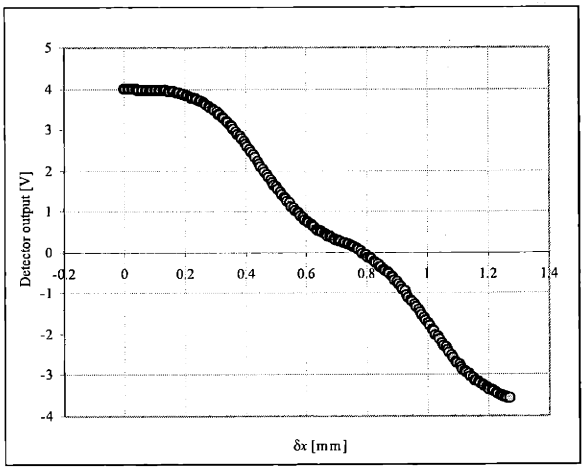

(b)

Figure 2-12: Typical calibration curves showing the different calibration ranges possible. (a) was used for a 260 V pulse, and (b) was used for a 2 kV pulse.

2.1.5 Pre- and post-magnetic field-pulse images

Twin bands

The extension of the crystals can also be confirmed by photographing it before and after applying the magnetic field-pulse. Although any temporal resolution is lost, it can be seen if the extension proceeds uniformly or if twin-boundary motion is localized in twin bands.

The crystal can either be removed from the holder and photographed with a high-resolution camera, or alternatively left in place and photographed with a low-resolution CCD camera (before and after the pulse) through the cylindrical hole of the coil. Although the CCD camera used yields lower quality images, it has the advantage that the real-time pulsed-field measurement can validate checking that there was no unexpected motion of the sample holder. The resolution is mostly sufficient to distinguish individual twin-boundaries. Some examples can be seen in Fig. 4-11.

2.2 Sample preparation

2.2.1 Single crystal characteristics

Throughout this work Ni–Mn–Ga single crystals are employed, which in the austenitic phase have the $Fm\bar{3}m$ structure depicted in Fig. 1-5. They were supplied by Ames Laboratory (Iowa) and by Adaptamat (Helsinki, Finland) respectively, and processed in similar fashion.

The composition of the Adaptamat crystal was determined with EPMA and can be seen in Table 2.1. Good homogeneity is seen along the length of the crystal (Fig. 2.2.1.) Other characteristics of the crystal are given in the Table 2.1.

The crystals were oriented and cut[22] into beams with square cross section, with the faces along $\langle 001 \rangle$. The crystal used in the experiments of Chapter 3, henceforth the

[22]EDM - spark erosion.

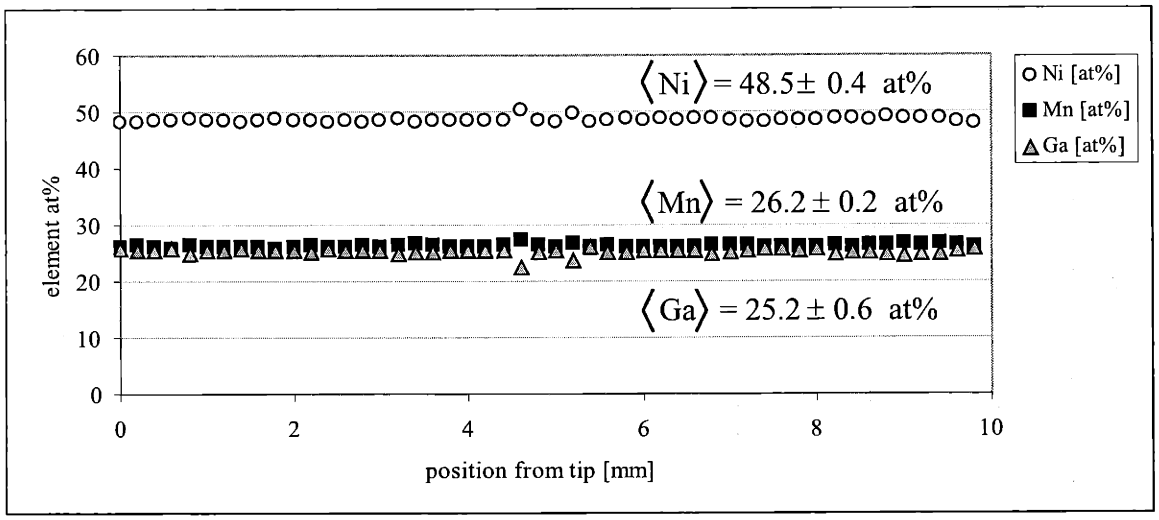

Figure 2-13: Composition profile along the length of the Adaptamat crystal used in the experiments reported in Chapter 3, obtained with EPMA. A good homogeneity is apparent.

Table 2.1: Selected properties of a Ni–Mn–Ga crystal used in the pulsed-field experiments.

Material property	Value
Average Nickel content	48.5 ± 0.4 at%
Average Manganese content	26.2 ± 0.2 at%
Average Gallium content	25.2 ± 0.6 at%
Magnetocrystalline anisotropy	1.9×10^6 erg cm^{-3}
Saturation magnetization	484 emu cm^{-3}
Mass density	8.1 g cm^{-3}
Resistivity	$62 \times 10^{-8}\,\Omega$ m
Curie temperature	95°C
Martensite start temperature	32°C
Threshold magnetic field for twin-boundary motion	1500 Oe
Stiffness	700 MPa

Adaptamat sample, has a cross section of 5.08 mm × 5.08 mm. The as-received length was 16.00 mm. Once cut the crystals were polished. The Adaptamat crystals were electro-polished as supplied from the factory, whereas some of the Ames Laboratory samples were electro-polished[23] and yet others mechanically polished. One Ames sample was also hot polished, that is, mechanically polished above 60°C, so that it would be austenitic and devoid of multiple martensite variants.

$(202)_{Fm\bar{3}m}$-twin planes intersect the crystal faces at 0° and 45° angles respectively. As can be easily seen, this orientation gives the largest extension for given volume fraction transformed.

The first step in preparing the samples is therefore to *activate* these twin planes, because as-received crystals oftentimes do not exhibit large field-induced strain. This process is sometimes called *training* the crystal. A strong (about 8 kOe) magnetic field applied in direction normal to one of the faces of the crystal, perpendicular to its long axis, ought to provide driving force for twin-boundary motion, unless the crystal was in a single-variant state with its [001]-axis coincident with the field direction. Because this field-induced variant reorientation is sometimes incomplete, compressive stress along the long direction of the sample, and subsequently a stress perpendicularto two other faces can be applied, and the process can then be repeated until applying a magnetic field along the sides that were compressed shows evidence of twin-boundary motion.

The necessity of mechanical stress cycling before field-induced twin-boundary motion can be obtained suggests that magnetic fields are capable of moving twin-boundaries but not of creating them (cf. Sec. C.1.1.)

It must be pointed out that the mechanically polished samples did not appear to show twin-boundary motion to the extent that electro-polished samples did.

It is necessary to consider a potential source of artifacts in the measurement of the extension, shown in Fig. 2-14. It is apparent that if the tip of the crystal is deformed during twin-boundary motion as in Fig. 2-14(b), then the mirror could tilt, producing a change of the detector signal that is not calibrated. To avoid these

[23]In nital 20%.

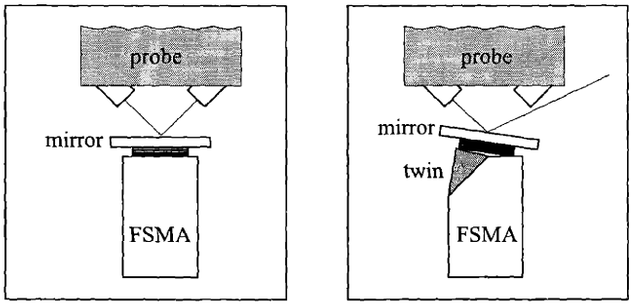

(a) (b)

Figure 2-14: (a) The configuration prior to twin-boundary motion. If the mirror tilts as in (b) a large signal change arises that cannot be accounted for by the calibration.

problems a corner is polished off at the tip of the crystal[24], so that the flat bevel is parallel to the active twin planes. The mirror is mounted on this bevel, insuring that the situation depicted in Fig. 2-14(b) will not occur.

2.2.2 Annealing

Repeated actuation of the samples caused the appearance of cracks. Two main factors were found to augment the likelihood of crack appearance. First, samples that were mechanically polished, especially with sharp edges, were observed to crack more quickly[25] upon repeated actuation. Secondly, especially (but not exclusively) when different twin systems coexisted in the crystal (see Fig. 2-15), repeatedly sweeping twin-boundaries through it caused cracks to appear. This occurred when the sample was twisted inside a strong ($\geq$ 1500 kOe) magnetic field in two perpendicular planes, or when the sample was cooled down from the austenite phase. The compression of the crystals and the application of a strong field in the same direction did not totally rid the crystal of spureous twin systems. Eventually, the crystals would show no field-induced extension.

[24] A jig made for this purpose is used, that allows to adjust two axes of the sample under a microscope so that the twin planes are aligned with the jig plane to better than 1°.

[25] The composition in the samples where this fact was most often observes was slightly higher in Mn, about 28%, and lower in Ga, about 22%, than in the Adaptamat sample.

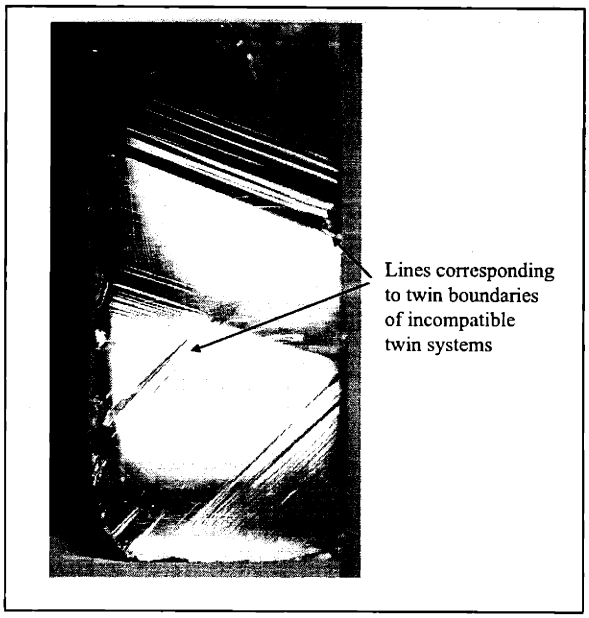

Figure 2-15: Picture of a Ni–Mn–Ga single crystal which developed incompatible twin systems after cooling from austenite in the absence of driving forces which could select one system instead of the other.

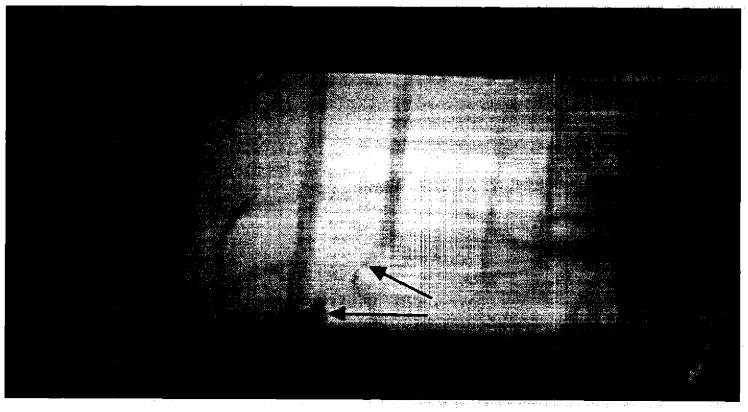

Figure 2-16: Picture of an Adaptamat crystal showing twin bands stopping at cracks that developed over the course of the experiments (arrows.) The bands shown were induced by a pulsed magnetic field from a 300 V discharge.

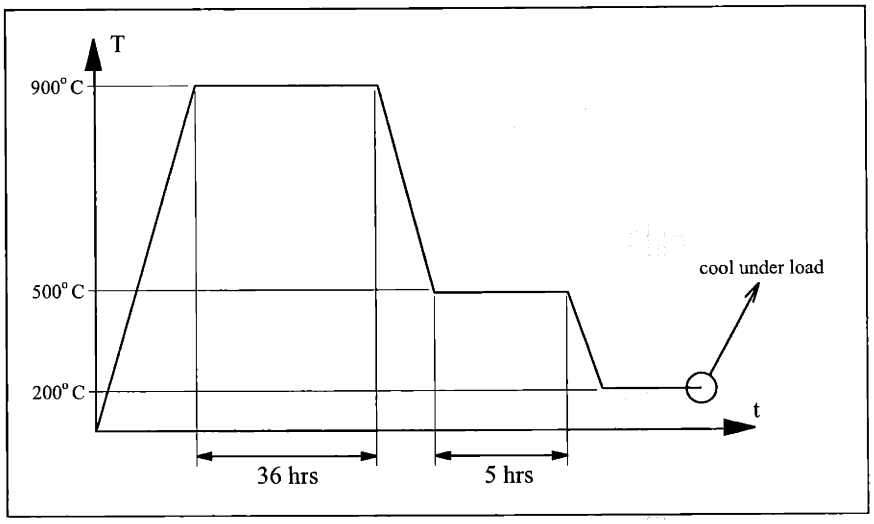

Figure 2-17: Annealing treatment used for the samples that showed greatly diminished field-induced twin-boundary motion. The treatment was done in 1.5 atm of Ar (at 900°C.) It succeeded in restoring twin-boundary mobility.

Figure 2-16 shows an Adaptamat crystal with twin bands stopping at cracks which developed over the course of the experiments.

To remedy these problems, the crystals are annealed in Ar-atmosphere, with the process depicted in Fig. 2-17. The crystals were first wrapped in W-wire[26] and encapsulated in a quartz capsule filled with pure Argon gas. They were then brought up to 900°C and kept at that temperature for about 36 hours. The crystal was subsequently cooled to 500°C, at which it is known to rapidly acquire the $L2_1$ order. After about 5 hours the capsule was cooled down further to about 200°C, at which point the sample was removed from the capsule and immediately put under a moderate[27] compressive stress along its long direction. The sample was allowed to cool through the martensite transformation temperature in this configuration and then removed for further use in experiments.

[26] After annealing at elevated temperatures for several hours an increased Silicon concentration in the crystals (and Manganese loss) has been observed. At 900°C the W-wire would act as a barrier for direct diffusion of Mn and Si.

[27] Between 1 and 8 MPa.

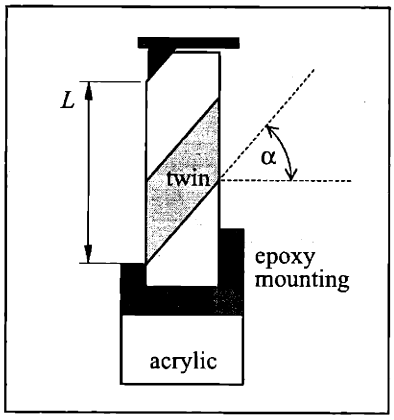

Figure 2-18: Schematic of the mounting of the crystal, showing the active length L defined by the epoxy constraint.

2.2.3 Mounting

Insuring a strong mounting of the crystal is essential, because the torque applied by the field to the magnetic moments transfers to the mass of the crystal through the anisotropy energy. This in turn would cause the sample, which essentially is in a cantilever configuration, to swing at its end, causing similar artifacts[28] as in Fig. 2-14. The crystal was first bonded to an acrylic cylinder with a special glue (Weld-on #45) which has excellent adhesive characteristics between acrylic and metals. Subsequently, a ring of epoxy (Devcon S-70) was applied to provide additional support on the sides of the crystal (see Fig. 2-18.) The region of the crystal not constrained by the epoxy was the active length of the crystal.

The active length L defines a volume of material that can be transformed from one variant to the other through the action of the field. This is the *active volume.*

2.3 Resetting

After the crystal was subjected to a magnetic field-pulse, a fraction of its volume is in a state where the magneto-crystalline easy axis is close to the direction of the pulse field. Clearly, further actuation (in the same direction) is not possible once the crystal's easy axis is aligned with the field. The crystal must be reset, that is, its volume must become a twin variant with a magnetic easy axis parallel to the direction where the actuating field is going to be applied.

In practice this is done by placing the crystal between the pole pieces of an electromagnet, with its long axis parallel to the field lines. The field is then increased to about 8 kOe and maintained at that level for about 1 minute. After this, the field was ramped down to zero, and the sample was ready to be placed in the pulsed-field experiment. It is important not to twist the crystal inside the magnetic field, lest incompatible twin variants are introduced (seen in Fig. 2-15.) This procedure was able to rid the sample of visible twin bands, and produce consistent results.

[28] A second oscilloscope acquiring the extension signal over 10 ms can register the characteristic ripple produced by this oscillation. Its presence reveals that the mounting of the crystal is defective.

2.4 Processing of the acquired data

The data acquired from the oscilloscope was copied into a spreadsheet or other software to be analyzed. It was filtered, and some characteristics of the extension vs. time were computed.

2.4.1 Digital filtering

Three basic filter types were considered: moving average, exponential smoothing, and polynomial interpolation. In Fig. 2-19 and Fig. 2-20 some representative examples of the filters considered for processing the data can be seen. The filter parameters are already optimized to remove most of the apparent noise, and retain a significant degree of detail. The filters considered include a moving average filter (Fig. 2-19(b))with 50 points averaging[29], an exponential smoothing filter[30] (Fig. 2-19(b)), and a polynomial interpolation[31] (Fig. 2-19(c).) This method is appealing for the simplicity in calculating the time derivatives, but has large numerical evaluation errors.

While the three filters have similar performance, the moving average type is chosen for the simplicity of its implementation. One direct consequence of the filtering is that fine details (signal differences of few least-significant-bits of the oscilloscope with persistence of no more than few μs) in the data are not identifiable. Nevertheless, it is possible to obtain reasonable values of the rate of extension.

2.4.2 Crystal extensional acceleration

The accuracy in the computation of the rate of extension however, is not high enough to warrant a precise determination of the crystal extensional acceleration through derivation with respect to time. Nevertheless, an approximate[32] lower bound for the

[29]This corresponds to $50\,\mu$s.

[30]The value of the filtered extension is computed as in the moving average, but weighing each point by the the value of a Gaussian bell centered at the center of the interval. In practice the weights $\exp(-0.07(t_i - t_{center})^2)$ were used, where t_{center} corresponds to the time for which the filtered value is sought, and t_i are the times of the other contributions.

[31]Grades of up to 19 were considered.

[32]In the sense that the values for the rate of extension are obtained from filters. Otherwise the acceleration calculated here is an average of various *instantaneous* accelerations, and therefore

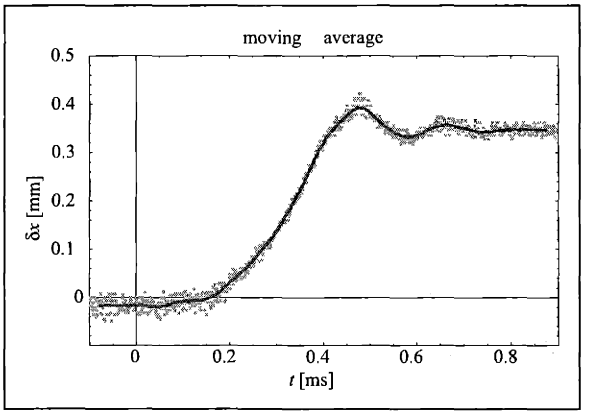

(a)

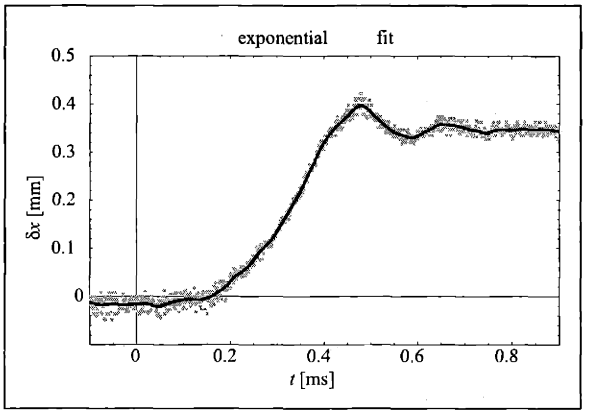

(b)

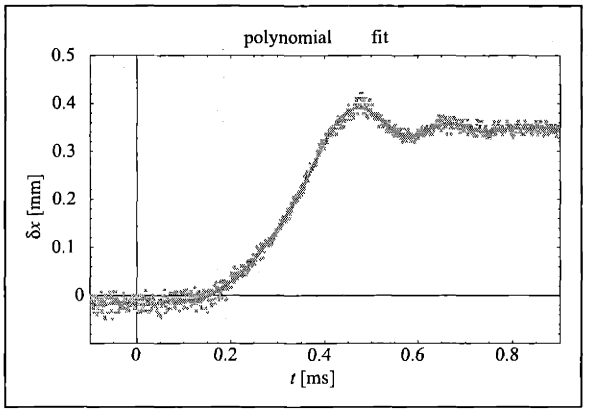

(c)

Figure 2-19: Filters applied to a representative extension data series: (a) moving average filtering, (b) exponential smoothing, and (c) polynomial interpolation.

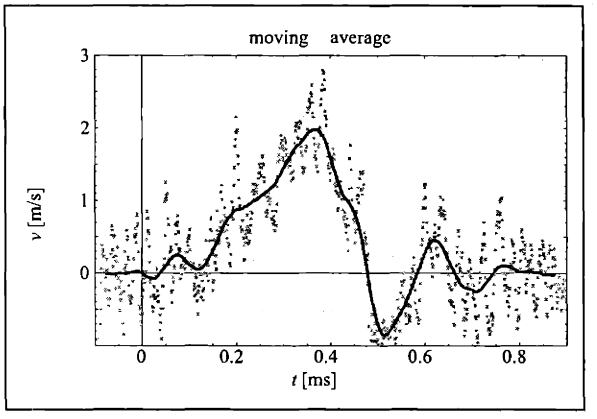

(a)

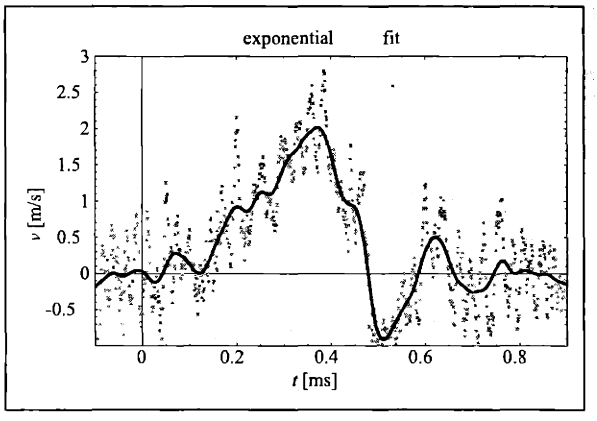

(b)

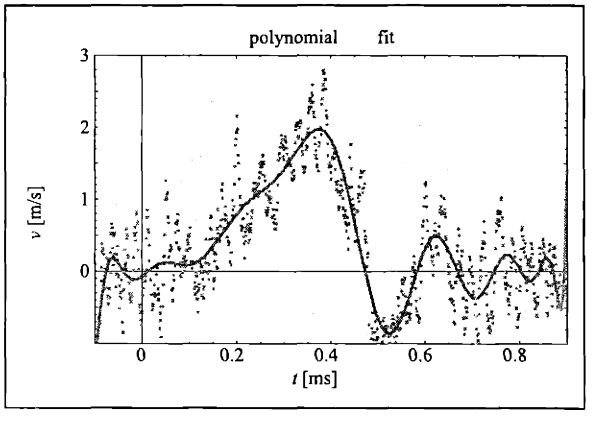

(c)

Figure 2-20: Filters applied to a representative rate of extension data series. The rate of extension was computed as the slope of a moving regression, and is shown as dots. The various continuous curves are (a) the moving average filter, (b) the exponential smoothing, and (c) the polynomial interpolation.

maximum acceleration from the rate of extension data can be obtained.

$$a \simeq \frac{v_{max}}{t(\text{peak } v) - t(\text{onset})} \simeq 50 \pm 10 \frac{\text{m}}{\text{s}^2} \tag{2.14}$$

a is an effective acceleration.

The values of the acceleration should be considered only order-of-magnitude estimates, which are nevertheless usefull in setting bounds for the performance of Ni–Mn–Ga in actuator devices.

2.4.3 Determination of the onset time for the extension

Determining the onset of the extension is important to estimate the driving forces required to initiate twin-boundary motion when the fields are rapidly varying. In this experiment, and particularly for low-voltage pulses (under 300 V) the noise level at the beginning of the extension complicates its accurate assessment. In order to identify trends in the data, a consistent algorithm for determining the onset of the deformation is needed. Several methods are possible (see Fig. 2-21.)

- Method 1: The final extension is computed as the average of the last 200 data points (the field corresponding to these points has already subsided.) The extension points with values between 25% and 75% of the number calculated are then selected, corresponding to the points where the velocity is highest, and a linear regression for those points is computed. The onset time t_1 in this method is then the intercept of the regression with $\delta x = 0$.

- Method 2: The time t_2 at which the extension reaches a set fraction (10% in this case) of the final displacement (computed as before) is found.

- Method 3: The time t_3 at which the extension reaches a set threshold value (in this case 0.005 mm) is found.

smaller than the maximum.

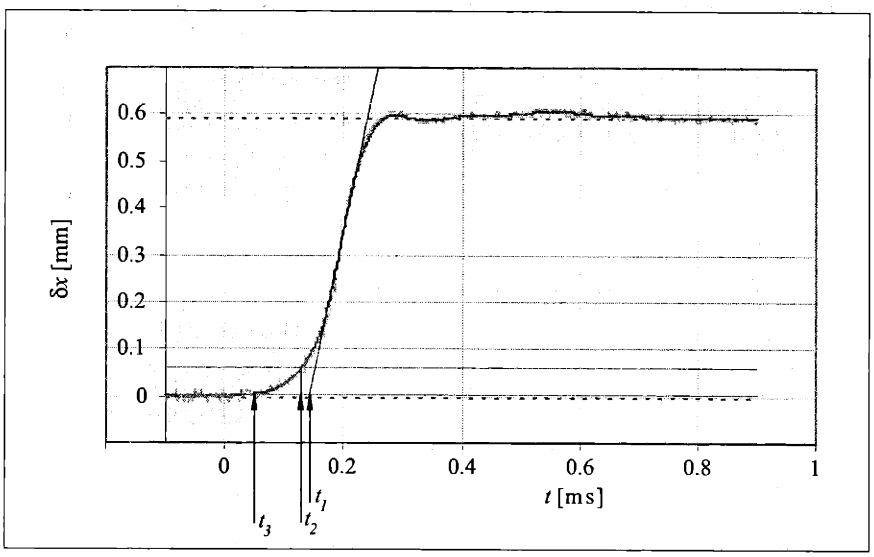

Figure 2-21: Example of extension data for a 2 kV pulse showing the various methods for determining the onset of the extension. The oblique line corresponds to the linear regression of the data between 25% and 75% of the final extension. In method 1 the intercept of this line with the abscissae is the onset time t_1. The gray horizontal line at $\delta x \simeq 0.59\,\text{mm}$ corresponds to the threshold level set for method 2, and the time at which it intercepts the extension curve is the onset time t_2 in this method. Likewise, a horizontal line at $\delta x \simeq 0.005\,\text{mm}$ is the threshold level for method 1. The intercept of this line with the extension curve yields the onset time t_3 in the method.

Method 3 is the most adequate, because it consistently sequences the pulse onset times with their amplitude. Method 1 fails for more noisy data (low extensions), and method 2, although scaling the threshold extension so that it roughly adapts to the noise-level of the measurement, is not the basis for a good comparison of the data.

Naturally, the exact value of the onset time will be affected by the noise level at low extension values. Consequently an uncertainty of several μs has to be adscribed to the onset time values (in practice, 10–50 μs.) This limits the precision of the onset driving force determination. It is obtained from the value of the field correspoding to the onset time, and therefore the uncertainty in the field goes like $\Delta H \simeq \left|\frac{\partial H}{\partial t}\right| \Delta t_o$. This value is large for the high intensity pulses where $\left|\frac{\partial H}{\partial t}\right| \geq 80\,\mathrm{kOe\,ms^{-1}}$, and large as well for pulses of very low intensity, where signal-to-noise ratio is poor.

2.5 Pulsed-field measurement procedure

The following illustrates the basic steps that compose a pulsed field experiment.

In order to minimize thermal drift during the experiment, the oscilloscope, DAC-voltage reference and preamplifier are left turned on at least overnight. The laser is thermally stabilized and it is not critical that it be left on for long periods of time. The photo-multiplier, however, is constantly kept at the operating voltage (425 V) to avoid contaminants from settling on the electrodes, which introduces significant noise and drift in the detector output. As well the small preamplifier directly attached to the photo-multiplier is kept on constantly.

1. The experiment is carried out in a darkened environment, as otherwise some light could enter the detector through the probe.

2. Reset the sample if necessary.

3. Measure the temperature[33]. To that end a thermocouple is attached to the center of the coil.

[33] All the present experiments were made at room temperature of 23°C ± 1°C.

4. Place the sample into the guide matching the marks on the guide and on the sample holder, to insure that the orientation is the same for all experiments. Fasten it firmly.

5. Set the optic probe close to the mirror, and retract it to a reference distance[34].

6. Set the DAC-voltage reference so that the detector signal is at the maximum of the operational range of the preamplifier.

7. Retract the probe by successive steps of known amplitude and record the detector intensity obtained, thus obtaining the calibration curve[35].

8. Define the expected extension for the planed experiment, and position the probe at least at that distance from the sample mirror[36].

9. Obtain a photograph of the sample.

10. Set up the oscilloscopes to acquire in two different time ranges, one to monitor the pulse response and another (longer) one to detect or rule out long-wavelength vibration artifacts.

11. Charge up the capacitors to the desired voltage and trigger the system (SCR and oscilloscopes.)

12. Save and post-process the acquired data.

13. Obtain a photograph of the sample.

[34]This is done to avoid possible backlash in the micrometer stage.

[35]The waiting time between steps needs to adjusted especially for low-voltage pulse experiments, to allow the small vibrations from the stepper motor to die out.

[36]The sample extends, thus reducing the distance between probe and mirror.

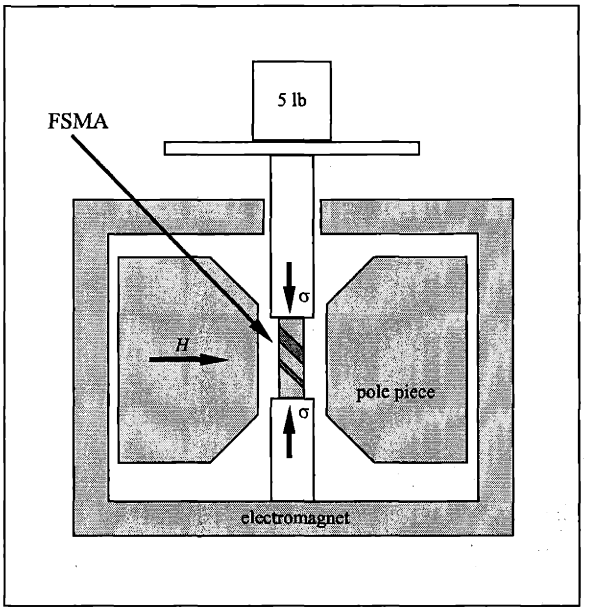

(a) Front view.

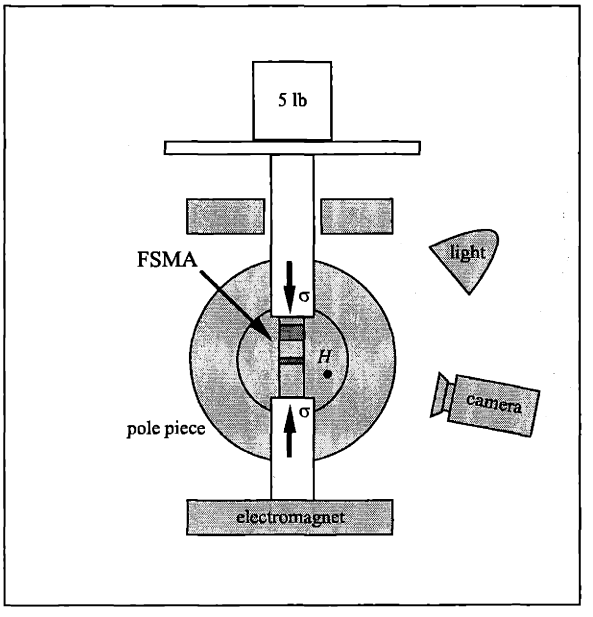

(b) Side view.

Figure 2-22: Schematic of the quasi-static field experiment setup, that was used to video tape the field-induced extension of a single crystal at high speed. The arrangement is that of Murray et al. [61].

2.6 High-speed images of the twin-boundary motion process

The first attempt to record the dynamic nature of the twin-boundary motion was made as part of this work with the device used to obtain quasi-static field-induced extension [61], depicted in Fig. 2-22. A Ni–Mn–Ga single crystal is placed between the pole pieces of an electro-magnet capable of producing 8 kOe field intensities. The crystal is in a single variant state with the [001] axis vertical, and is compressed with a small weight, to prevent it from slipping when the field is turned on. It is illuminated with a halogen lamp[37] and the video camera[38] is set up facing the side of the crystal that points out of the magnet (that is, out of the plane of Fig. 2-22.)

The magnetic field is ramped up to about 6 kOe and a rate of about 1 kOe/s. When the fieldramp begins the camera is triggered. It dumps the acquired frames to a memory bank, which can then be downloaded to a tape and digitized. 1000 frames per second were recorded for 20 s. Figure 3-13(a) shows a typical frame acquired with this method:

[37] It is turned on only during the image acquisition, so as not to heat up the sample.
[38] Redlake MASD Ektapro Model 1012 High Speed Video System.

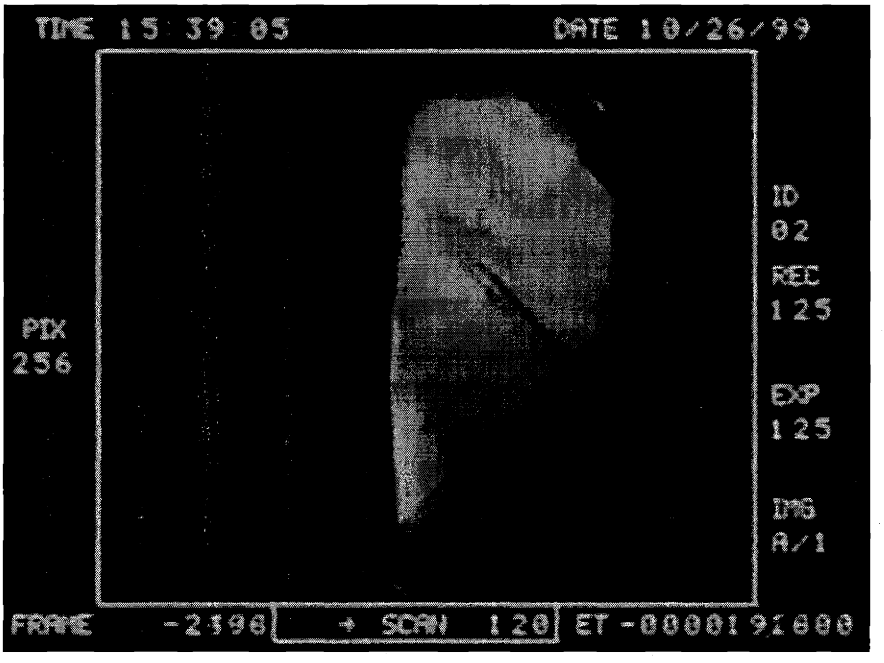

Figure 2-23: Frame obtained from the high speed (1000 fps) imaging of a Ni–Mn–Ga single crystal while the field was ramped up to about 6 kOe.

Chapter 3

Results

This Chapter presents the data obtained from pulsed magnetic field experiments performed on a sample of single-crystalline Ni–Mn–Ga from Adaptamat, and the images taken with a high-speed video system from a different single crystal from Ames Laboratory.

The Adaptamat sample was prepared as described in Sec. 2.2 in Chapter 2. Upon repeated actuation cracks developed in the crystal. When that occurred the crystal was cut into smaller pieces that were free of such cracks. The crystal's length is indicated accordingly when necessary. The cross section remains constant and is 5.08 mm × 5.08 mm for the samples used here (Adaptamat.)

The first section of this Chapter presents the results of a single pulse from a 2 kV capacitor discharge. Essentially all the unfavorably oriented twin variants are rearranged by the magnetic field. Then data from field-induced twin-boundary motion for a series of low-intensity magnetic field pulses is presented. In this case a threshold behavior for the extension of the sample can be observed. Next these data are compared with a similar set obtained for high-intensity pulses. In the subsequent section plots of the driving force- or magnetic pressure-response characteristics of the crystal are shown that include all the pulses' data. Following this images documenting individual twin-boundary motion are shown. Finally, the dependence of the onset time with the driving force is addressed.

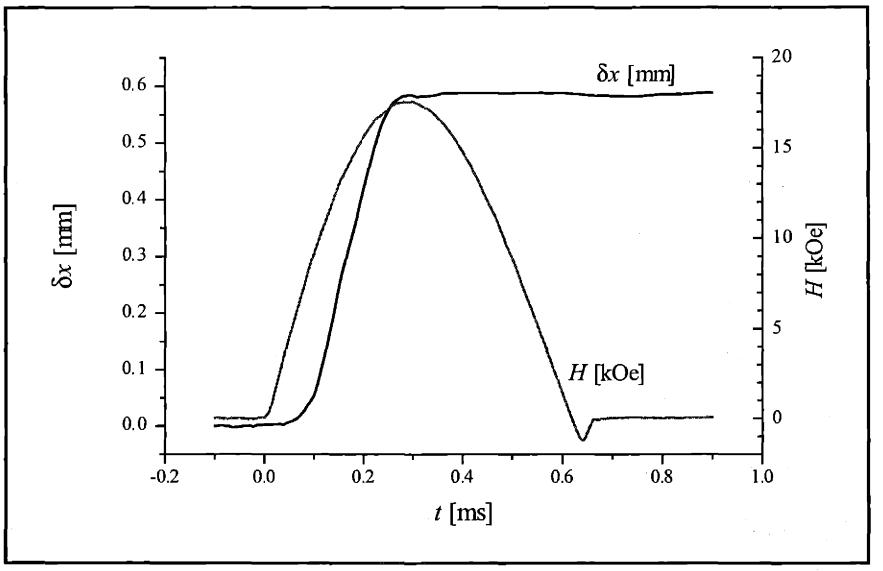

(a)

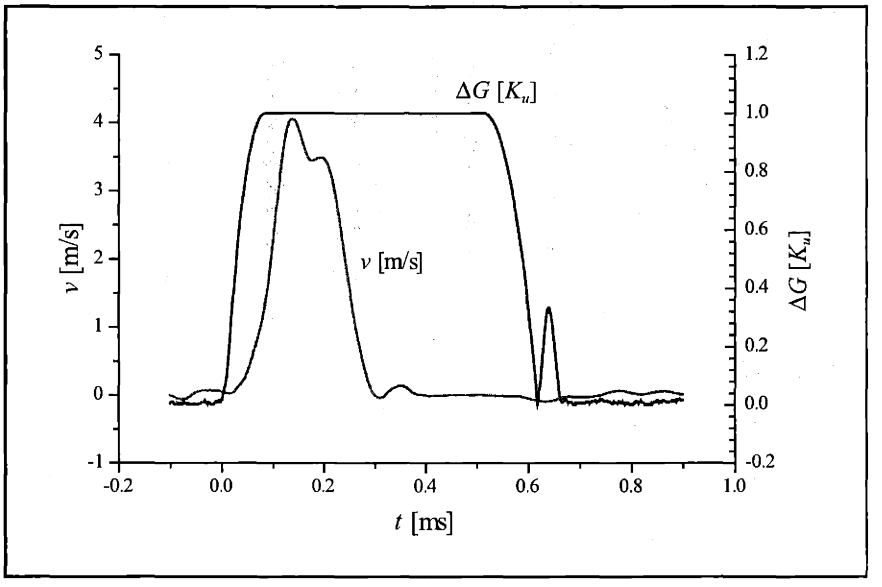

(b)

Figure 3-1: Pulsed magnetic field experiment results for a 2 kV capacitor discharge. (a): Displacement (left axis) and field intensity (right axis) are plotted vs. time. The final displacement reaches 0.586 mm and the peak field is 17.6 kOe. (b): driving force (inferred from the field) and rate of extension of the crystal (inferred from the extension) vs. time, corresponding to Fig. 3-1(a). To compute the driving force the values for the magnetocrystalline anisotropy and saturation magnetization from Table 2.1 were used. The driving force is linear with the field for $H \ll 2K_u/M_s$, as is expected from Eq. (1.10). For $H \geq 2K_u/M_s$, the driving force saturates, reaching a maximum value of $-K_u$.

3.1 Extension from a 2 kV discharge pulse

Following the steps described in Sec. 2.5 it is possible to obtain curves of field intensity and extension as a function of time by processing the acquired voltage data as shown in Sec. 2.4. Figure 3-1(a) shows a measurement from the magnetic pulse resulting from a 2 kV discharge. The evolution of the magnetic field follows the profile expected for an under-damped oscillatory system. It rises quickly initially, at a rate of 87 Oe/μs, and gradually levels off until it reaches a peak of 17.6 kOe after 300 μs. Beyond this point the field decreases. A negative excursion is observed before the damping is complete. Note, however, that the driving force for twin-boundary motion does not change sign throughout the duration of the pulse[1].

The sample extension does not occur concurrently with the magnetic field because there is a finite stress or magnetic pressure that has to be overcome before the twin-boundaries move. Instead, it begins $40 \pm 4\,\mu$s after the onset of the field, when $H \simeq 3.9\,$kOe. This threshold field is considerably larger than the field at which an extension is recorded in the DC case, (1.5 ± 0.2)kOe (see Sec. 2.4.3 for more information.)

The extension reaches a final value of 0.588 mm at $t = 365\,\mu$s. This corresponds to a strain of 5.95%. The near coincidence of the peak extension with the peak field is coincidental, as the analysis of additional pulses in the following sections will show.

Using a value for the twinning strain of 6.2% (see Sec. 1.3.3) and an active[2] crystal length of $9.85 \pm 0.01\,$mm, the measured extension suggests that approximately (96 ± 4)% of the active crystal volume transformed from one variant to the other through the action of the field. The magnitude of the extension observed suggests that what is limiting further extension in this example is that essentially all of the unstable (under the field) variant was transformed.

In this experiment the nearly total transformation from one variant to the other

[1] Field of opposite signs will stabilize opposing 180°-domains, but favor the same variant, thus inducing the same extension.

[2] See Fig. 2-18.

was achieved at the expense of 480 J of energy for the pulse generation.[3] It is interesting to point out that only a small fraction of this energy can drive the twin-boundary motion. The maximum energy density that can be coupled into the material, which is numerically equal to the magnetocrystalline anisotropy $K_u = 1.9 \times 10^6\,\mathrm{erg\,cm^{-3}}$, is about 50 mJ. Joule heating of the resistors accounts for the large remaining fraction of energy. Ultimately, the lower bound for the dissipated energy will be given by the static[4] (as in pinning defects) and dynamic (as in phonon and electron scattering) hindrances to twin-boundary motion. While these are negligible in comparison with the energy dissipated on the circuit's resistance, they can cause a temperature increase in the crystal which could push it out of the operation range[5].

The rate of extension of the crystal v is the derivative with respect to time of the crystal extension. As discussed in Sec. 2.4.1 the rate of extension is approximated by the slope of a moving linear regression of extension. The resulting set of curves for the rate of extension vs. time can be seen in Fig. 3-1(b). On the same time axis the driving force is plotted, which is obtained from Eq. (1.10) and the values for K_u and M_s of Table 2.1.

Because the driving force saturates so quickly, its profile over time has a step-like shape. Even though the field does not reach its peak until about 300 μs from the pulse onset, the driving force reaches 90% of its saturation value after only $59 \pm 3\,\mu$s. The rate of extension reaches its peak value of 4 m/s in $139 \pm 10\,\mu$s. A direct relation between this rate of extension and the speed of the twin-boundaries cannot be established *a priori* because their exact number is unknown while the pulse lasts. Photographs of the crystal before and after the application of the pulsed magnetic field give information only about the macroscopic regions where one type of variant is clearly predominant.

Notice that the extension reaches its peak value smoothly. It would appear to

[3] From $U = \frac{1}{2}CV^2$, which gives the energy required to load a capacitance C to a voltage V.

[4] If the twin-boundary is not displaced past the "static" pinning obstacle, of course no work will be done. The work required to free the pinned twin-boundary from the obstacle is meant here.

[5] That is, temperatures below the martensitic transition temperature. This problem was apparent during AC measurements [48].

decrease after first reaching the peak. This decrease is also reflected in the rate of extension as a small dip immediately after the peak. Accuracy at such level of detail in the deceleration process is not warranted by the precision of the present experiment. Further, the twin-boundaries are expected to move in a jump-like fashion, each "jump" occurring when partial dislocations overcome pinning defects and expand without hindrance forming a mono-layer twin. Through subsequent nucleation of partial dislocations the twin-boundary would advance rapidly (see Sec. 4.2.3.) The present experiment is not suited to measure these processes.

In Fig. 3.1 the above data is plotted as extension vs. field and vs. driving force. As the field (driving force) increases, so does the extension, until the final value is reached. There are no external restoring forces in this experiment, therefore the extension does not decrease. Notice that in this example the extension occurs essentially at constant driving force, because the driving force very quickly reaches the saturation value of K_u. This is apparent in the vertical segment of the deformation curve in Fig. 3-2(b).

3.2 Actuation without driving force saturation

The sample's extension for select magnetic field pulses of increasing amplitude is now explored. From Sec. 1.4.2 it is known that the driving force for twin-boundary motion is not linear with the field. The deviation from linearity increases as the Zeeman energy $M_s H$ approaches the anisotropy limit, $2K_u$. Figure 3-3 shows the maximum driving force for pulses of increasing initial capacitor voltage. Because the (peak) field scales with the initial capacitor voltage (Eq. (2.13)), the plot is an indication of the linearity of the (maximum) driving force with the field. From the initial points depicted in Fig. 3-3 it is seen that in this series of measurements the driving force remains close to linear with the field. Figure 3-4 shows the measured extensions (3-4(a)) and corresponding driving forces (3-4(b)). The plots for the extension are similar in shape to those of Fig. 3.1. As the peak driving force or (equivalently) the magnetic pressure increases, the extension increases as well. This monotonic response

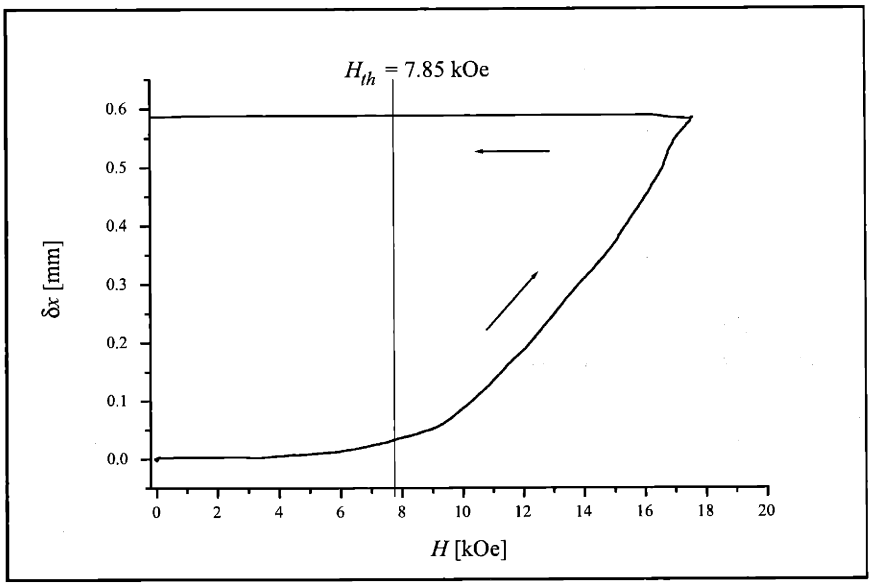

(a)

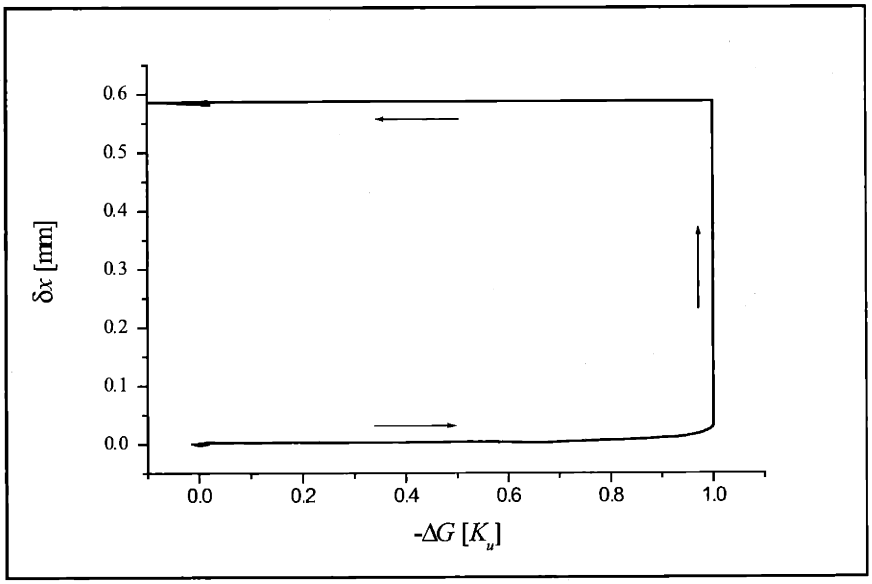

(b)

Figure 3-2: Pulsed magnetic field experiment results for a 2 kV capacitor discharge, from Fig. 3.1. (a) extension vs. field. It increases from zero to 0.586 mm as the field increases (see arrow) and then remains essentially at that value while the field decreases to zero. (b) extension vs. driving force. It increases from zero to 0.586 mm. During the major part of the extension process the driving force is saturated and thus constant.

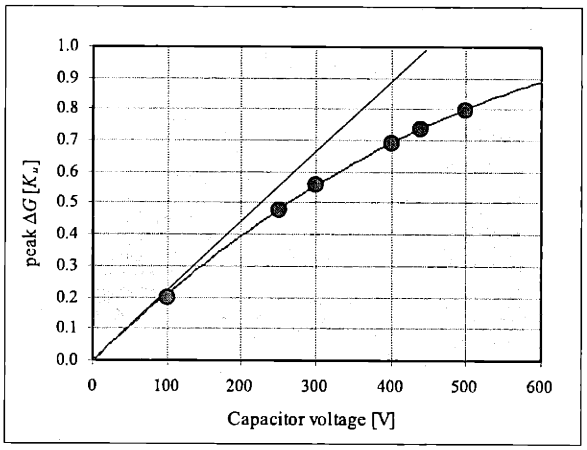

Figure 3-3: Peak driving force for twin-boundary motion (discrete points) attained during the discharge of the capacitor bank charged to the indicated voltage. The resulting pulses are discussed in this section. The continuous straight line represents the first order approximation to the driving force from Eq. (1.10). The continuous curved line represents the Eq. (1.10). The data is fitted well by assuming that the peak $H = 8.75\,\mathrm{kOe\,V^{-1}} \times V$, where V is the voltage to which the capacitors are charged. Because the magnetic field scales with the capacitor bank voltage, the plot correctly describes the departure from linearity with field for the more intense pulses.

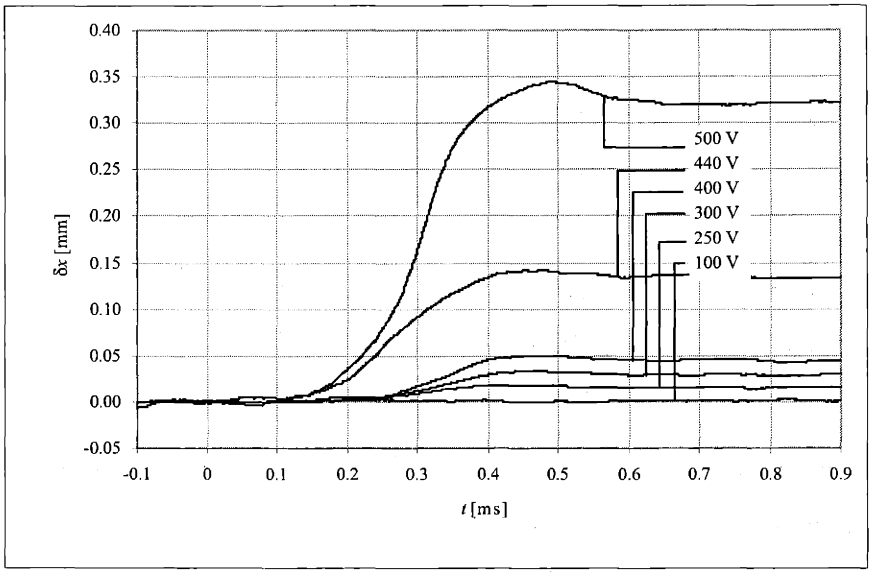

(a) Crystal extension

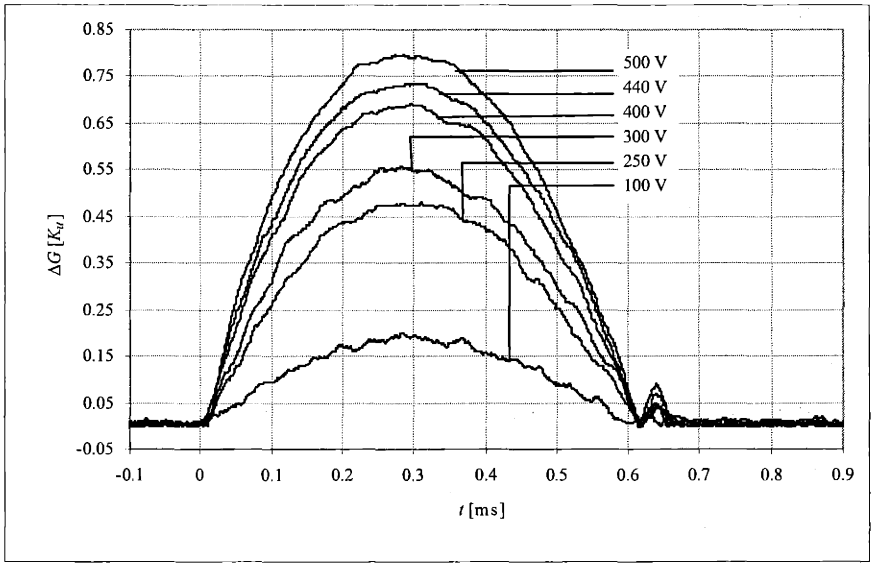

(b) Driving force for twin-boundary motion

Figure 3-4: (a) Plots of the extension vs. time and (b) the corresponding driving force vs. time for the magnetic field pulses generated with discharges ranging from 100 to 500 V. The driving force for these pulses does not saturate. This implies that the driving force is close to linear with the field, so that the peak driving force is to first approximation proportional to the capacitor voltage. A 100 V pulse does not cause twin-boundary motion at 0.2 $K_u$driving force, or about 0.6 MPa. A 200 V discharge generates a peak driving force of about $0.5K_u \simeq 1.5$MPa, which is enough to generate an extension. It is apparent that increasing the pulse amplitude also increases the displacement.

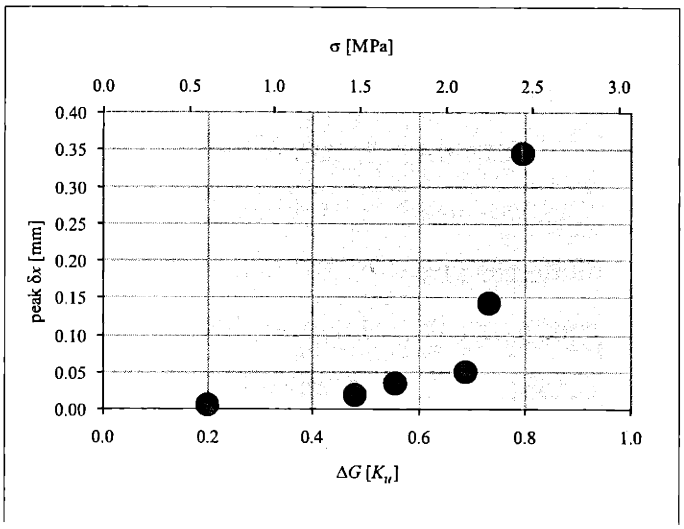

Figure 3-5: Plot of the peak extension vs. the driving force (i.e. magnetic pressure on the twin-boundary), from the curves plotted in Fig. 3-4. It can be seen that although monotonic, the extension is not linear with the magnetic pressure. A threshold-like behavior is apparent.

is not linear however, as is seen more clearly from Fig. 3-5. Pulses of similarly spaced driving force give rise to extensions that are small and close together at low driving forces, and larger and further appart for large driving forces. The net field-induced extension vs. driving force appears to be threshold-like, with the threshold driving force located at $\Delta G \simeq 0.5\,K_u = 1.5\,\mathrm{MPa}$, which corresponds to a field of 2.2 kOe. From Fig. 3-4(a) two onset times for the extension appear to exist. For the 440 V and 500 V pulses the extension commences at about 140 μs, whereas for the pulses of 400 V and below the extension sets in around 260 μs.

Consider the 250 V pulse, which has a peak driving force of $0.48\,K_u$. The extension appears to begin for this pulse at 252 ± 4 μs from the onset of the field when the driving force exceeds $0.47\,K_u$. The fact that an extension is observed (it peaks at 0.018 mm) for this pulse implies that $|\Delta G| \geq 0.47\,K_u$ can drive the twin-boundaries.

The 500 V discharge is now considered having this in mind. It is apparent that the twin-boundary motion begins at a driving force of about $0.32\,K_u$, which is smaller than in the previously mentioned case. Moreover, it stops when ΔG becomes smaller than about $0.45\,K_u$, some 500 μs after the pulse begins. This is surprising, because when time $t \in [500, 540]$ μs the driving force remains above the $0.32\,K_u$ threshold, and the extension would be expected to continue.

Consider in turn the 300 V discharge. Twin boundary motion begins in this case when ΔG exceeds $0.56\,K_u$, and peaks after ΔG has reached its maximum value, at a level of $0.41\,K_u$. Notably, this value is smaller than the value at onset of the extension.

These results suggest that twin-boundary motion observed in these experiments is not solely a function of the driving force. In principle it would be possible to associate an inertia to the twin-boundaries, a matter subject to discussion in Sec. 4.2.2.

3.3 Actuation with driving force saturation

Consider now the case where the driving force is close to the anisotropy energy (K_u.) Figure 3-6(a) shows the extension vs. time for the pulses of driving force plotted vs. time in Fig. 3-6(b). In this series of experiments a crystal of length 9.85 ± 0.01 mm

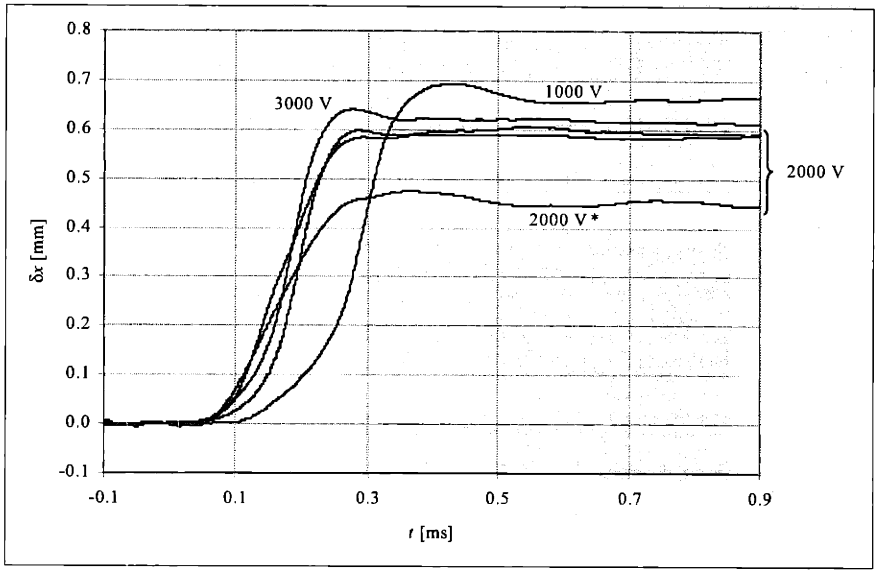

(a) Extension

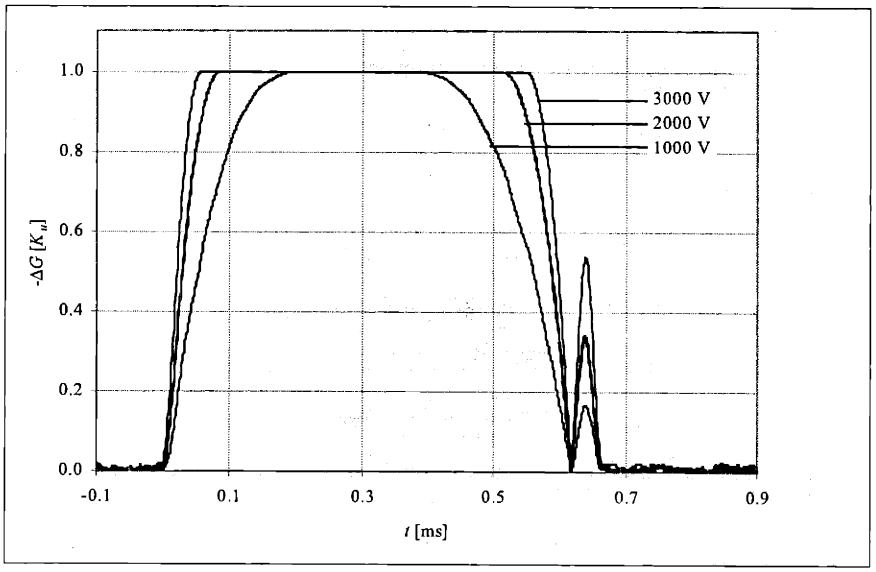

(b) Driving force

Figure 3-6: (a) Plots of the extension vs. time and (b) the corresponding driving force vs. time for the magnetic field pulses generated with discharges ranging from 1 to 3 kV. It is apparent from (b) that the driving force saturates. It's profile resembles a step function, and each pulse has a slightly different rise time or initial slope. The length of the crystals is 9.85 $\pm$ 0.01 mm, except for the second pulse labelled 2000 V*, obtained with a 8.00 $\pm$ 0.01 mm long crystal.

was utilized, except for one of the 2 kV pulses (labelled 2000 V*) for which the length was 8.00 ± 0.01 mm., see Fig. 3-6.

In this case the driving force is no longer close to proportional to the field, and it is apparent that the driving force flattens when it reaches K_u. The field quickly becomes intense enough to force the alignment of the magnetization with it, so that the driving force becomes equal to the magnetocrystalline anisotropy for a range of fields[6], and the profile is a nearly square pulse. The extension essentially stops while the driving force is above the threshold value at extension onset. As mentioned in Sec. 3.1, this is attributable in part to the fact that almost all the active volume[7] of the crystal has been transformed.

The three 2 kV pulses have the same driving force profile to within measurement uncertainties (see Fig. 3-6(b).) From Fig. 3-6(a) the corresponding extensions are different, most notably between the second pulse (the first one for 2 kV) and the two following ones. While the extension of the second pulse is 0.449 ± 0.002 mm the final value of the following two pulses is higher (0.587 ± 0.002 mm and 0.591 ± 0.002 mm.) Thus, the second pulse's extension is about 77% of that of pulses 3 and 4. The difference is not unexpected given the difference in active lengths for both cases (8.00 ± 0.01 mm vs. 9.85 ± 0.01 mm.)

The five pulses here described saturate the driving force (thus peaking at K_u.) They do so with different threshold times, and at varying speeds, so that the driving force-saturation lasts different time amounts. The first pulse of this series, obtained from a 1 kV discharge, reaches saturation of the driving force 200 μs after pulse onset, about 140 μs after the 3 kV pulse reaches saturation, and remains at saturation for about 210 μs, almost 290 μs less than the latter. This notwithstanding, it reaches a final extension of 0.664 ± 0.002 mm, surpassing the final extension for the 3 kV pulse (0.614 ± 0.002 mm.)

The extension onset times for the different pulses seem to coincide at 50 ± 5 μs for all but the least intense pulse of the series. The latter begins its extension at

[6] i.e., for $|H| > 2K_u/M_s$.
[7] See Sec. 2.2.3.

$100 \pm 5\,\mu$s from pulse onset. This seems consistent with the the driving force profile in Fig. 3-6(b).

3.4 Crystal extension and time derivatives

Cumulative plots of the extension vs. the peak field and driving force are presented in Fig. 3-7. It is apparent that in Fig. 3-7(a) the final extension increases sharply once the peak field exceeds a threshold of about 2 kOe. It reaches saturation around 0.66 mm near 8.7 kOe, corresponding to the field-induced variant transformation of the full volume, essentially.

Fig. 3-7(b) shows the data vs. the driving force. A threshold driving force at about half the anisotropy is observed in Fig. 3-7(b) as before in Fig. 3-5, but the trend is developed beyond the small-intensity pulses.

Since fields in excess of 7.85 kOe saturate the driving force, the abscisae of active driving force for twin-boundary motion are bounded to the interval $[0.49, 1.0] \times K_u$, that is, fields within $[2.24, 7.85]$ kOe. The extension is bound between $\delta x = 0$ and $\delta x = 0.66$ mm. In this range, the final extension increases with the peak driving force.

Fig. 3-7(b) displays scatter in the data. Specifically, pulses with essentially the same peak driving force give rise to different final extensions. The strict monotonicity of the final extension is therefore lost.

The rate of extension generally proceeds as exemplified by Fig. 3-1(b) and Fig. 3-8. It rises from zero to a peak value and then subsides. It can be seen from Fig. 3-1(b) that the peak occurs at earlier times for large peak field s than for low ones. 2 kV pulses and higher subside before the field reaches its peak value, indicating that by then the extension is complete. Similar peak rate of extensions are attained by the 1 kV pulses and higher, with one exception for one 2 kV pulse, which also has a broader peak. In Fig. 3-9 the cumulative plot of the peak rate of extension[8] vs. driving force is shown for various pulses. Upper and lower bounds for the mobility can be sketched on the plot, and show a minimum and maximum mobility at given field levels, which

[8]The peaks of the rate of extension vs. time curves, such as Fig. 3-8.

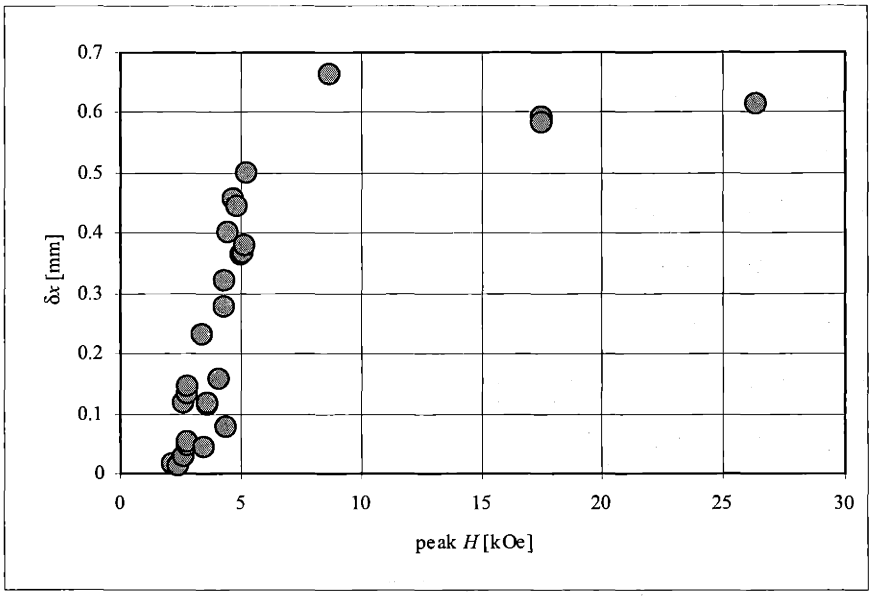

(a)

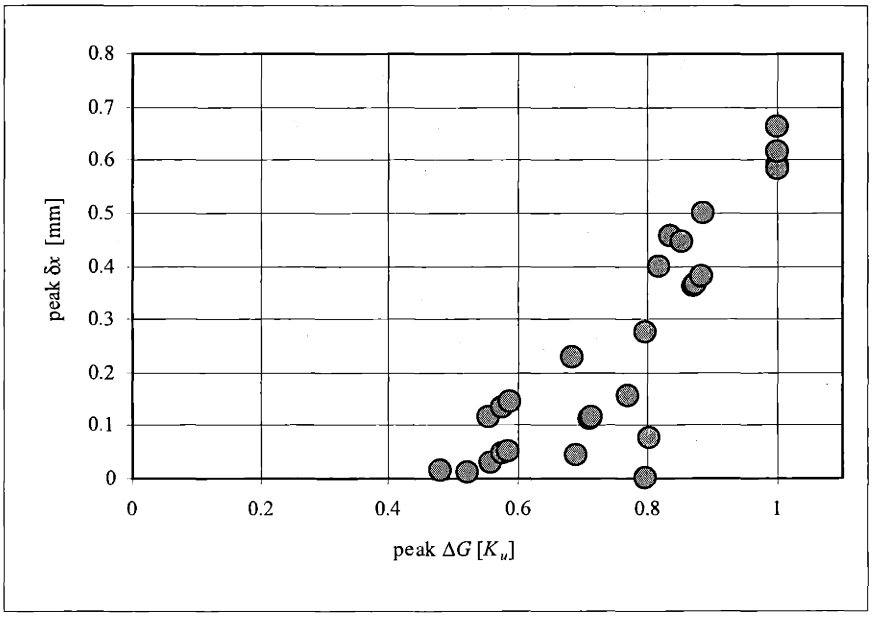

(b)

Figure 3-7: Peak extension for various pulses, in terms of (a) the peak field and (b) the peak driving force.

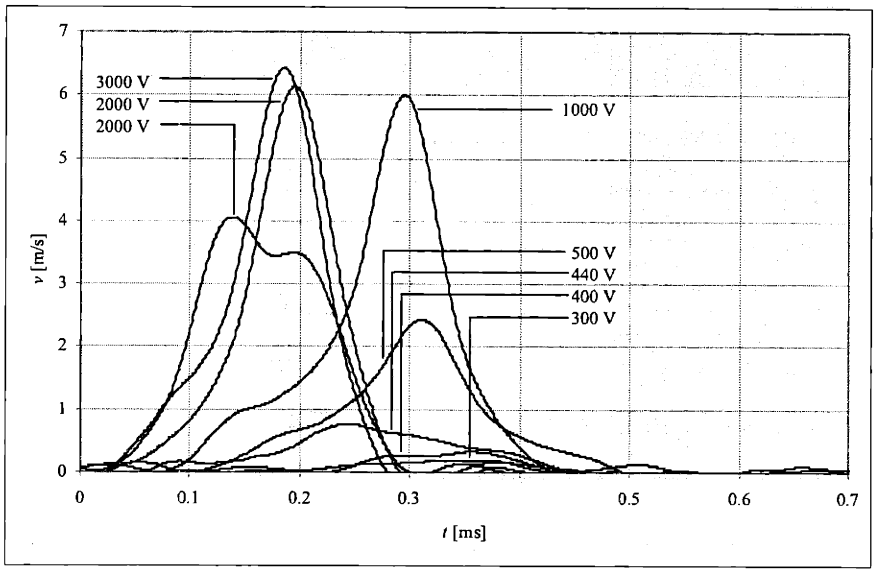

Figure 3-8: Rate of extensions obtained from the data plotted in Fig. 3-4(a) and Fig. 3-6(a).

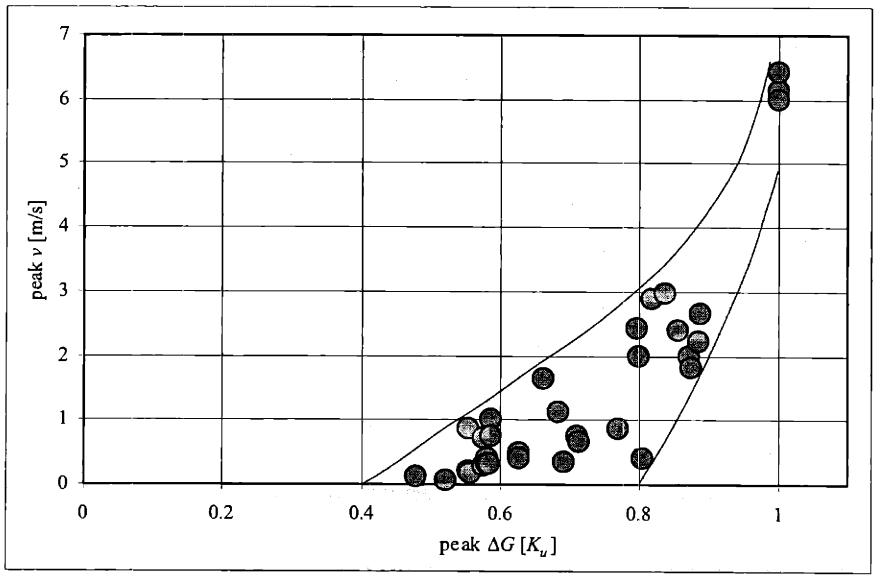

Figure 3-9: Cumulative plot of the peak rate of extension vs. the peak driving force. The envelopes drawn for the data give bounds for the mobility of the twin-boundaries in this crystal.

increase with the driving force.

As was mentioned earlier, it is technically important for applications to have an order of magnitude estimate of the effective acceleration of the extension. As discussed in Sec. 2.4.2 one such estimate can be obtained from from Eq. (2.14). Figure 3-10 plots these effective accelerations vs. the driving force. If can be seen that the maximum effective acceleration is $50\,\mathrm{m\,s^{-2}}$ (about $5\,g$) and that it remains essentially zero for small driving force. For a driving force greater than $0.42\,K_u$ the effective acceleration augments with the driving force, at a rate of approximately $25\,\mathrm{m\,s^{-2}}$ per K_u ergs of energy input until saturation of the driving force is reached. Alternatively, it is possible to say that the effective acceleration increases by $80\,\mathrm{m\,s^{-2}}$ per MPa of driving force, where the expression of Eq. (1.11) was used to write the driving force as a magnetic pressure. In Sec. 4.2.2 possible reasons for the existence of this inertia are discussed.

The accumulation of points at $-\Delta G = K_u$ shows that parameters other than the driving force influence the effective acceleration.

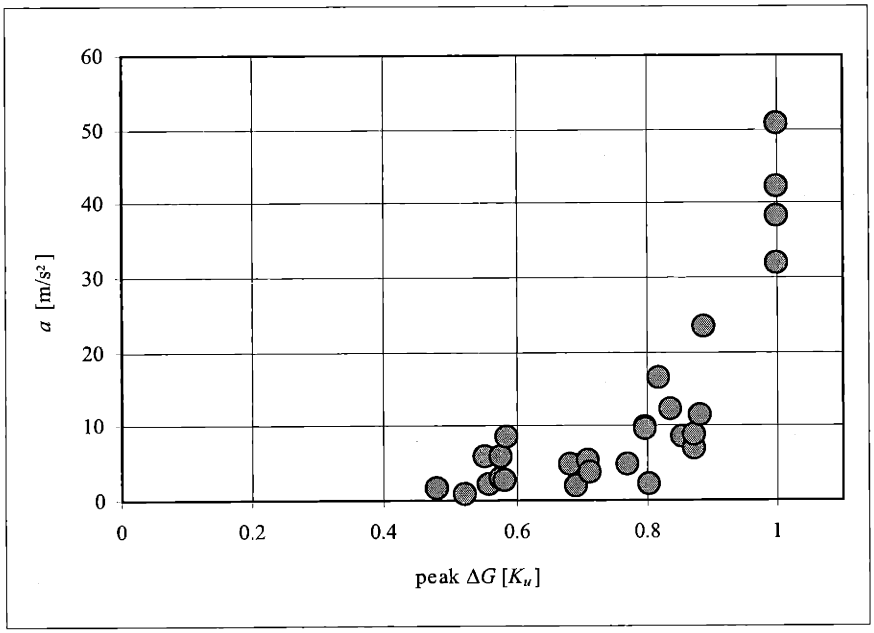

Figure 3-10: Effective acceleration as per Eq. (2.14) for pulses of varying peak driving force.

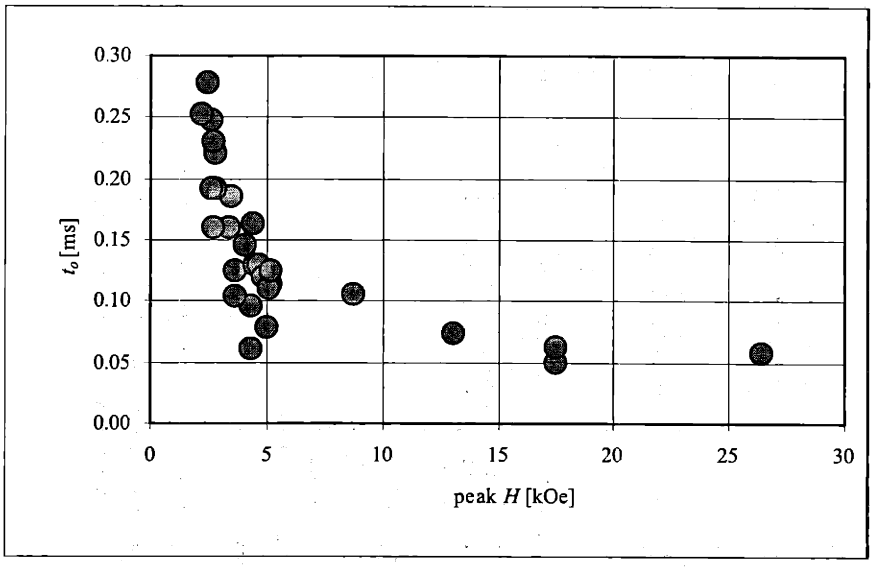

(a)

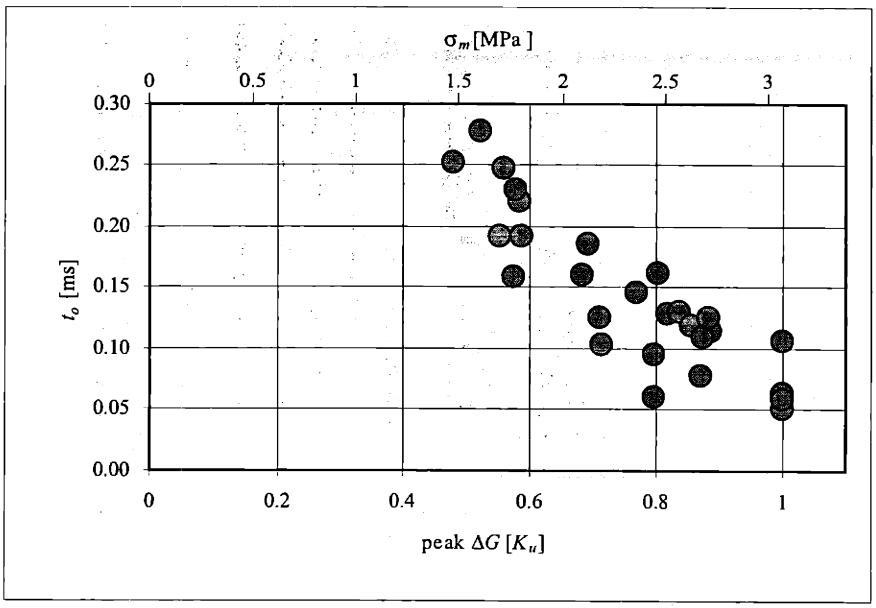

(b)

Figure 3-11: Plots of the onset time (t_o) vs. peak field (a) and vs. peak driving force (b). The onset time was found as the time at which the extension first exceeded the threshold extension of 0.005 mm.

3.5 The extension onset

It is desired to determine the characteristics of the extension onset. To that end a value of 0.005 mm was chosen as the extension that allows us to determine consistently when the extension has begun (see Sec. 2.4.3.) Fig. 3-11(a) shows the onset time vs. the peak field and the peak driving force respectively, for various pulses.

Note that the onset time varies with each field-pulse. It takes on values from 50 μs to 280 μs. The lowest onset times ($< 100\,\mu$s) are observed for peak fields above 5 kOe.

In Fig. 3-11(b) the same data is shown, but plotted as onset time vs. driving force (or magnetic pressure.) The general trends in the onset time observed before in terms of the field are manifest as well in this case. For very small driving forces (below about $0.47 \times K_u$) no points are registered, indicating that a weak driving force is not capable of moving twin-boundaries.The onset time tends to decrease with peak driving force, showing that mobility of the twin-boundaries is high enough to respond to a driving force which rises with increasing speed. This can be seen better in Fig. 3-12, where it is also apparent that the onset time at higher driving forces tapers off.

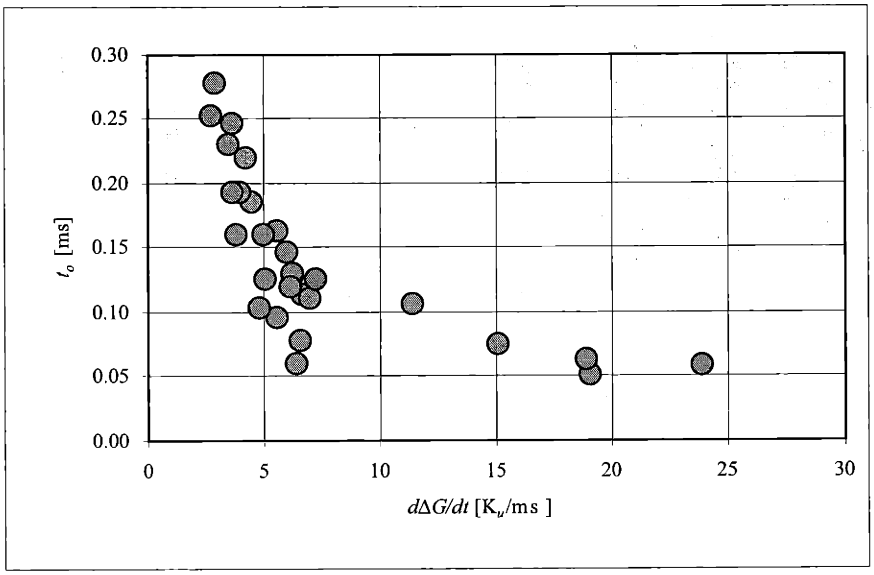

Figure 3-12: Plot of the onset time vs. the peak rate of driving force increase.

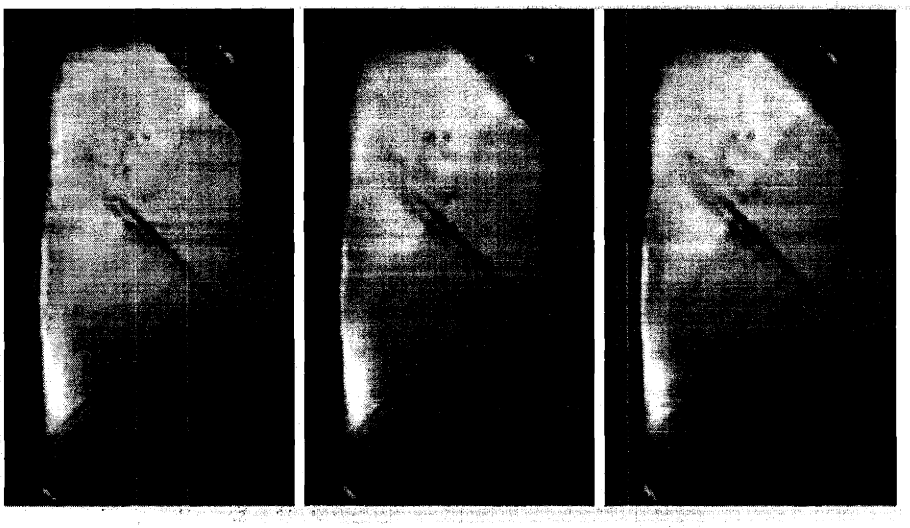

(a) Initial frame (b) +1 s ± 0.1 s (c) +2 s ± 0.1 s

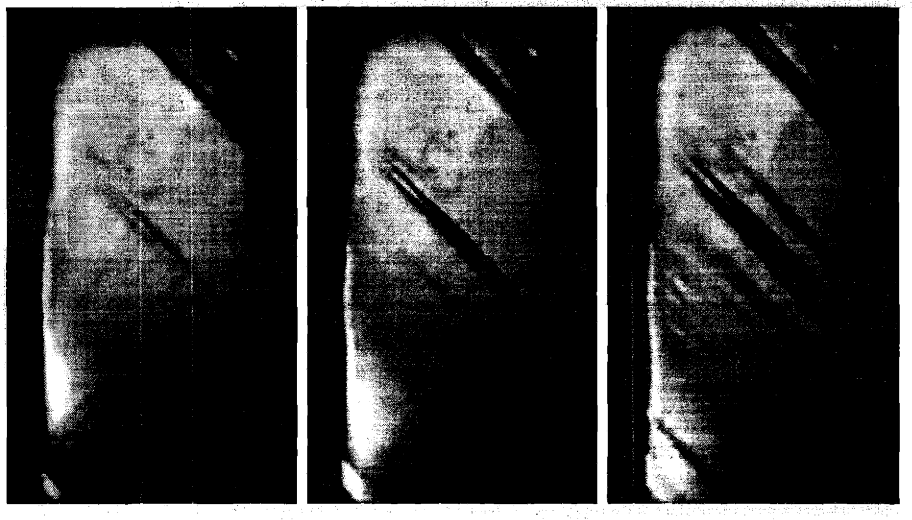

(d) +3 s ± 0.1 s (e) +4 s ± 0.1 s (f) +5 s ± 0.1 s

Figure 3-13: Selected images from a high-speed (1000 fps) movie of the twin-boundary motion in a single crystal of Ni–Mn–Ga under the action of a field that was ramped up from 0 to about 6 kOe in 6 s (see Sec. 2.6.)

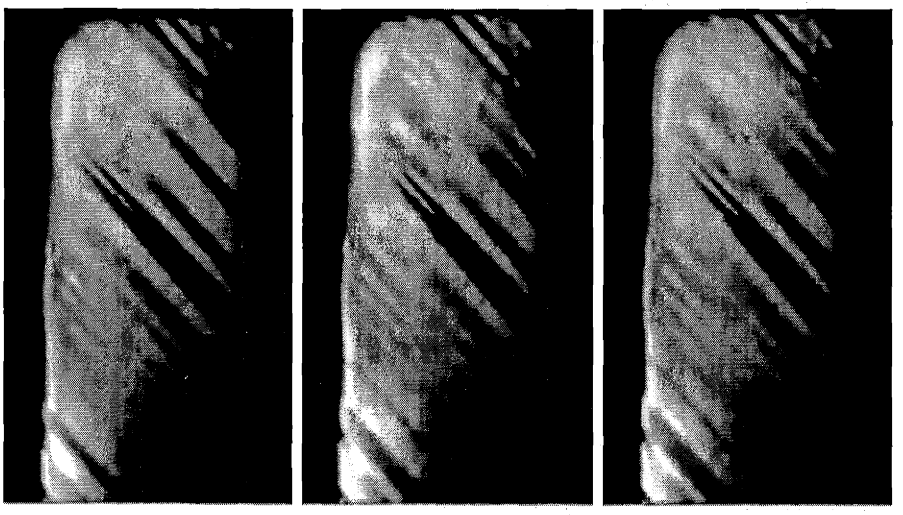

(h) +6 s ± 0.1 s (i) +7 s ± 0.1 s (j) +8 s ± 0.1 s

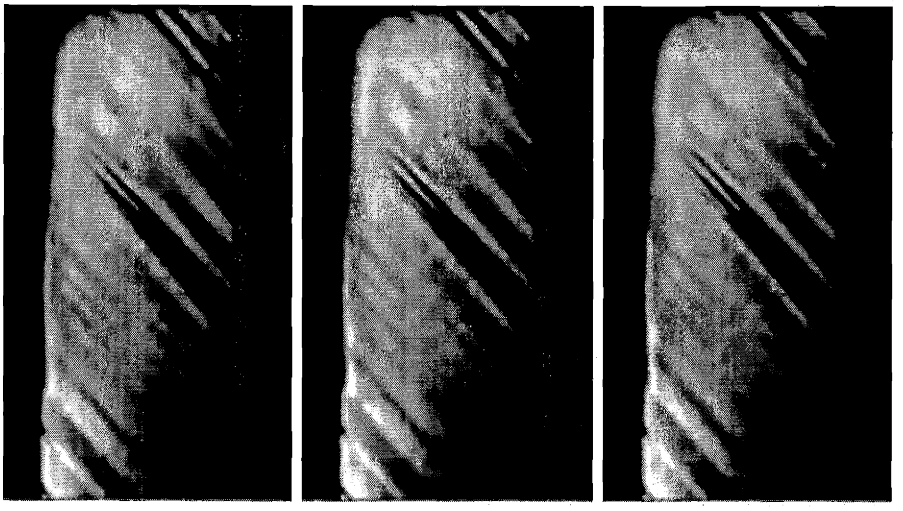

(k) +9 s ± 0.1 s (l) +10 s ± 0.1 s (m) +11 s ± 0.1 s

Figure 3-13: (cont'd.) Selected images from a high-speed (1000 fps) movie of the twin-boundary motion in a single crystal of Ni–Mn–Ga under the action of a field that was ramped up from 0 to about 6 kOe in 6 s (see Sec. 2.6.)

3.6 Discrete twin-boundaries

The transformation of one variant to the other by the action of a magnetic field (or a stress for that matter) in general does *not* take place uniformly along the length of the crystal. In fact, it seems to proceed in discrete locations of the crystal, which results in alternate regions of reciprocal twins that appear as characteristic bands on the sides of the crystal. This was observed early on in the development of this work, and is most clearly seen in the succession of images from the high-speed video in Fig. 3-13.

Greater control of the field than in the set of images from Fig. 3-13 is achieved with the pulsed-field experiments. In Fig. 3-14 the evolution of the extension of the Adaptamat crystal used for the pulsed-field experiments of the previous sections is shown. The images were obtained without resetting the crystal after every pulse, in contrast to what was done previously.

It is observed that initially the field-pulse is able to generate two thin twin bands. A second and third pulse of identical shape and amplitude causes these twin bands to thicken and two new ones to appear each time. Subsequent pulses mostly thicken existing twin bands, but no new ones appear except on one occasion (Fig. 3-14(i)) where the pulse height was slightly larger. It is apparent that particularly cracks in the crystal can stop the motion of a twin-boundary and pin it. Notably, a stable configuration is reached after several pulses (Fig. 3-14(l)): it does not change if additional pulses (of the same intensity are applied.)

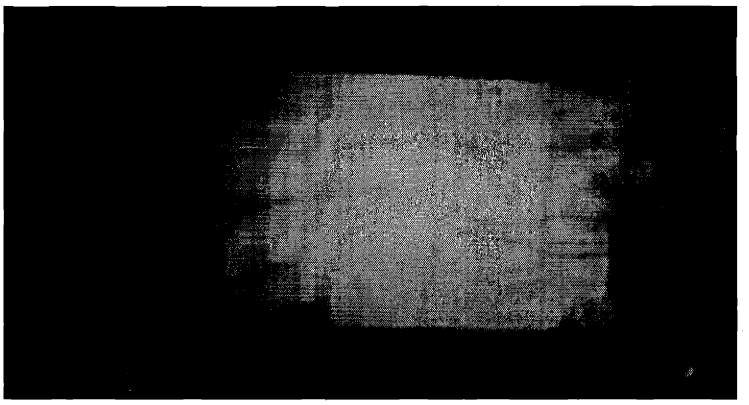

(a) Reset crystal (starting point)

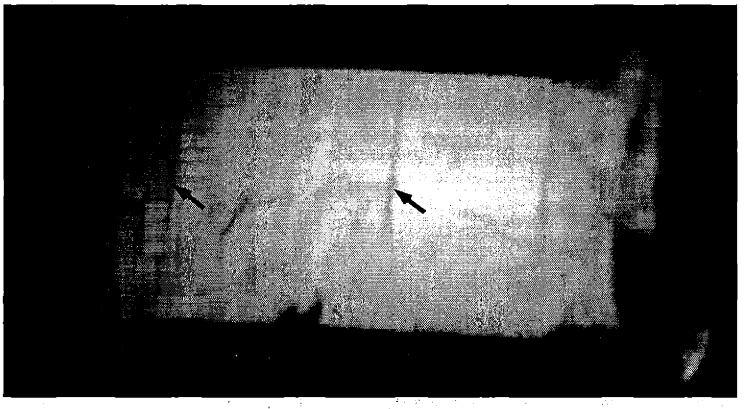

(b) Pulse 1: 2.2 kOe peak field.

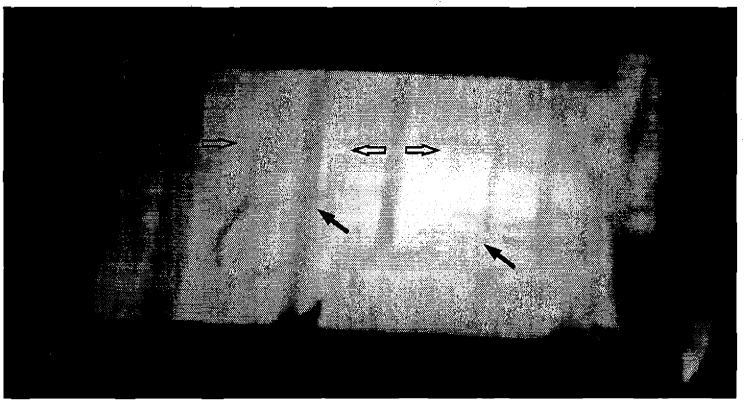

(c) Pulse 2: 2.2 kOe peak field.

Figure 3-14: Images of the evolution of individual twins for a series of field-pulses generated with $300 - 320$ V discharges. The solid arrows indicate twin bands that were not observed after the previous pulse. The empty arrows indicate motion of a twin-boundary in the direction of the arrow as compared with the previous pulse.

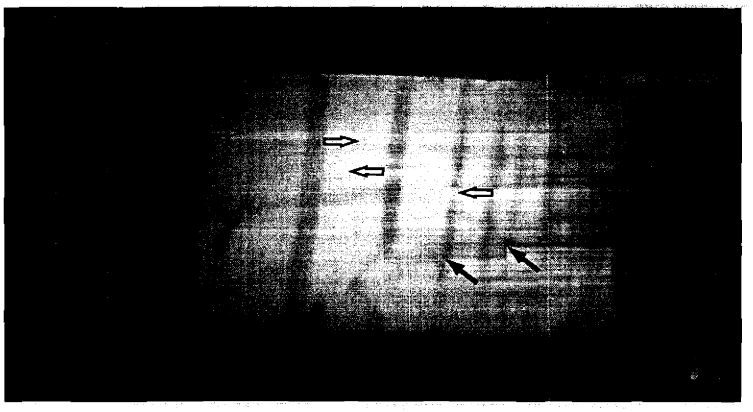

(e) Pulse 3: 2.2 kOe peak field.

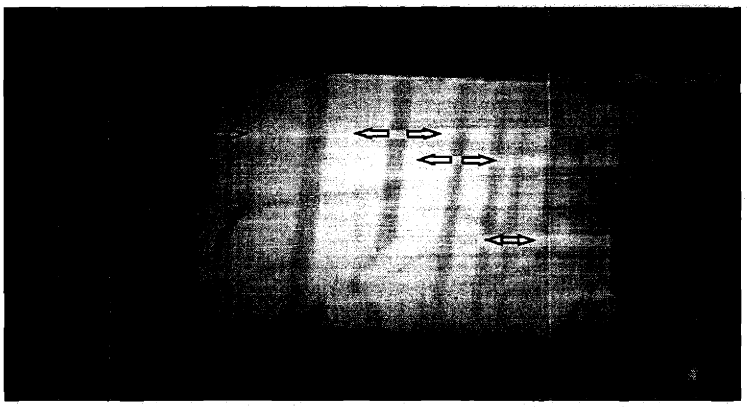

(f) Pulse 4: 2.2 kOe peak field.

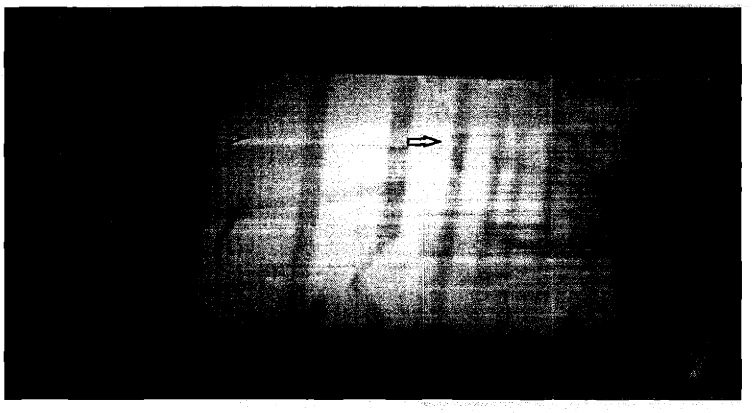

(g) Pulse 5: 2.2 kOe peak field.

Figure 3-14: (Cont'd.) Images of the evolution of individual twins for a series of field-pulses generated with $300 - 320$ V discharges. The crystals were *not* reset after each pulse. The solid arrows indicate twin bands that were not observed after the previous pulse. The empty arrows indicate motion of a twin-boundary in the direction of the arrow as compared with the previous pulse.

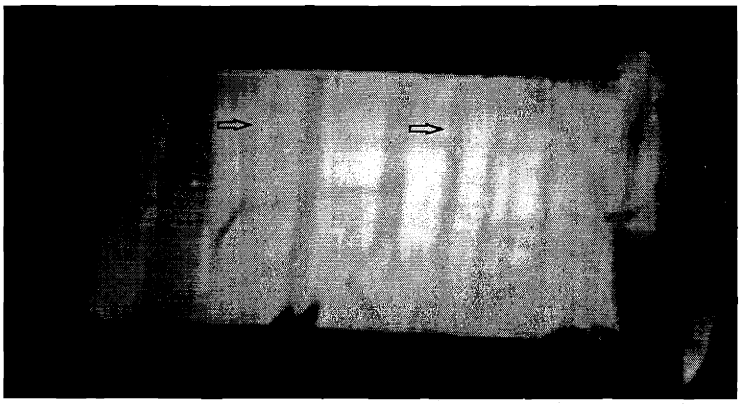

(h) Pulse 6: 2.2 kOe peak field.

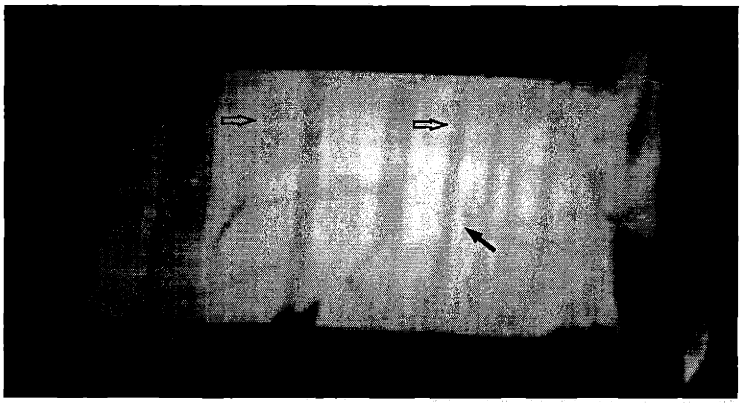

(i) Pulse 7: 2.5 kOe peak field.

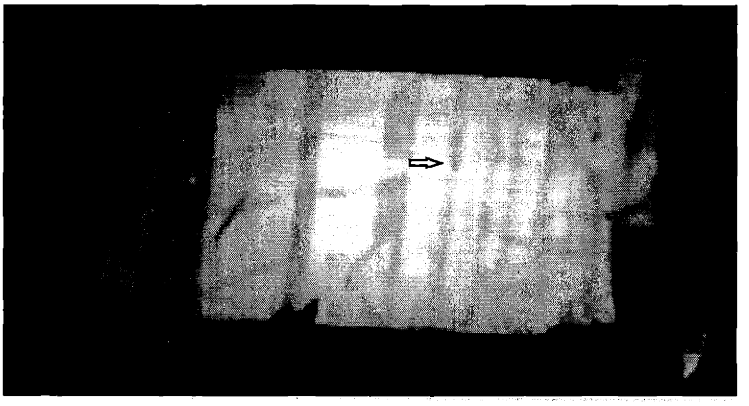

(j) Pulse 8: 2.2 kOe peak field.

Figure 3-14: (Cont'd.) Images of the evolution of individual twins for a series of field-pulses generated with $300 - 320$ V discharges. The crystals were *not* reset after each pulse. The solid arrows indicate twin bands that were not observed after the previous pulse. The empty arrows indicate motion of a twin-boundary in the direction of the arrow as compared with the previous pulse.

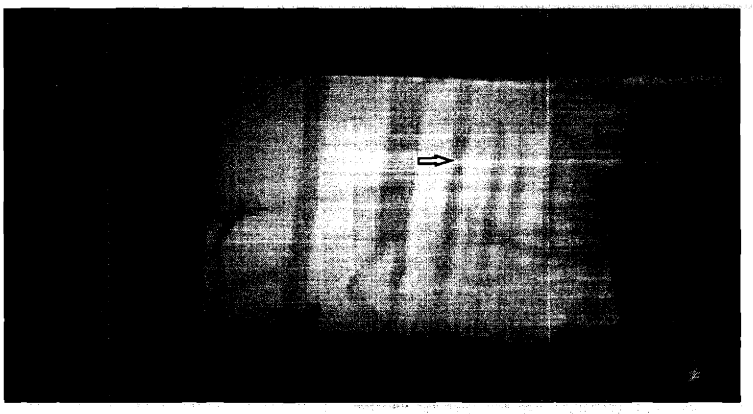

(k) Pulse 9: 2.2 kOe peak field.

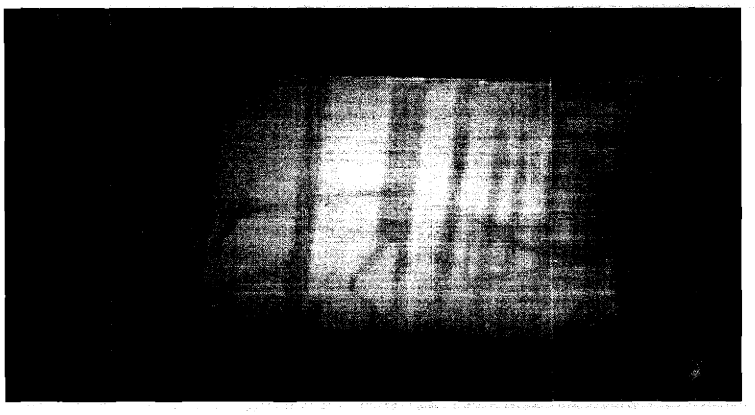

(l) Pulse 10: 2.2 kOe peak field.

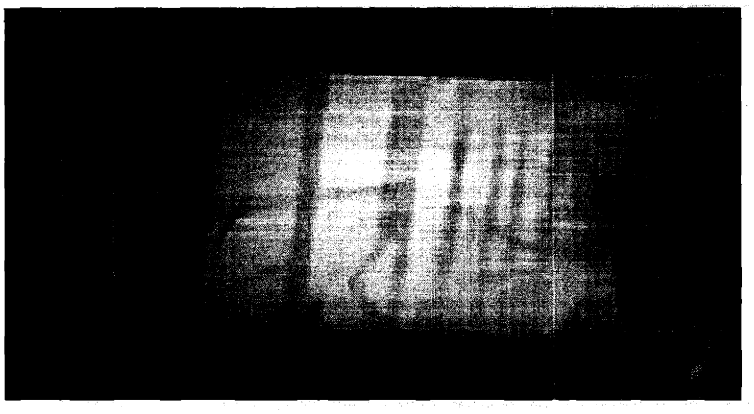

(m) Pulse 11: 2.5 kOe peak field.

Figure 3-14: (Cont'd.) Images of the evolution of individual twins for a series of field-pulses generated with $300 - 320$ V discharges. The crystals were *not* reset after each pulse. The solid arrows indicate twin bands that were not observed after the previous pulse. The empty arrows indicate motion of a twin-boundary in the direction of the arrow as compared with the previous pulse.

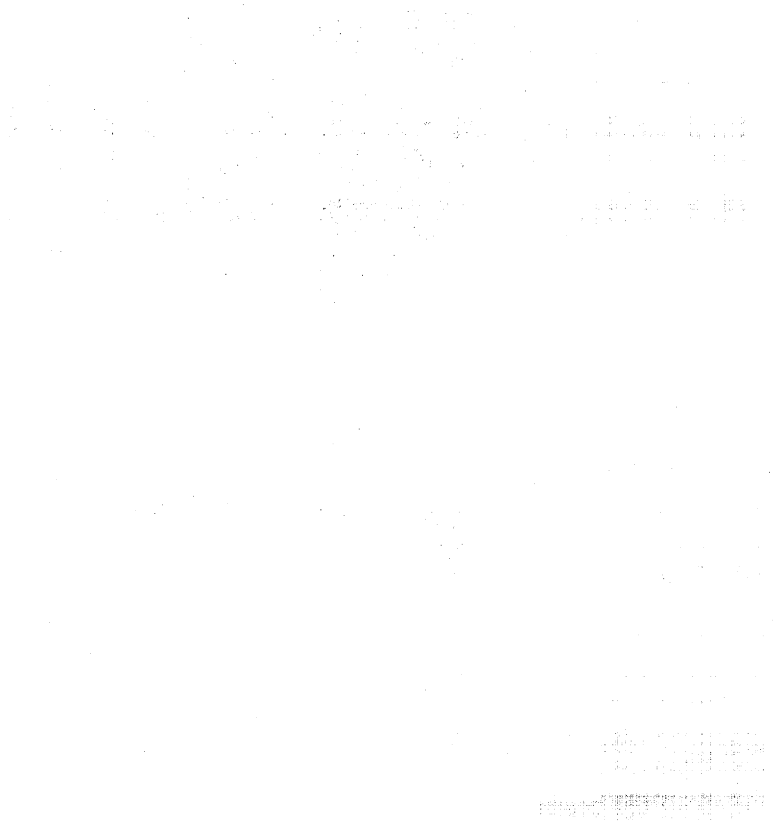

Chapter 4

Discussion

This Chapter discusses the results reported in Chapter 3. In Sec. 4.1 the results of Chapter 3 and their relation to the quasi-static field-induced twin-boundary motion reported by Murray et al. [61] are commented on. In Sec. 4.2.1 the effect of eddy currents on the value of the magnetic field inside the crystal is discussed. In Sec. 4.2.2 the influence of the system's mass on the onset of the extension is considered, and in the following Sec. 4.2.3 the same problem is discussed from the point of view of nucleation of partial dislocations as the rate-limiting process during twin-boundary motion. Following this, data on the rate of extension from the previous section is discussed in terms of the influence of crystal defects (Sec. 4.2.5.) In Sec. 4.3 the implications of the pulsed-field experiments here described are indicated.

4.1 Quasi-static driving forces vs. dynamic driving forces

In Fig. 3.1 the extension vs. field and extension vs. driving force for a pulsed-field experiment has been shown. Consider now Fig. 4-1, where the quasi-static extension from [39, 61] is superimposed over data for the real-time extension for 600 V and 2000 V pulses. It is apparent that the final extensions attained by the pulsed- and quasi-static actuation are of comparable magnitude. Note in particular the empty

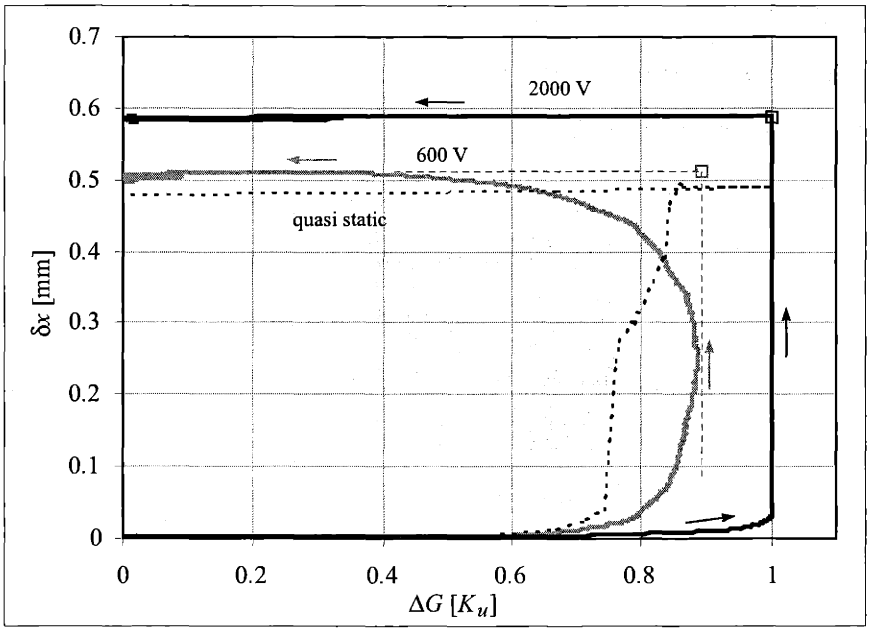

Figure 4-1: Plots of the extension (δx) vs. peak driving force (peak ΔG) for a 2 kV pulse (black) and a 600 V pulse (gray.) Superimposed are prior results of Murray et al. [61] (dotted line.) In all cases the field was increased from 0 following the arrows, and a extension then developed. In the absence of restoring forces the extension does not decrease to zero with the driving force. The empty squares indicate the maximum extension for the peak field.

squares, indicating the extension that is obtained using as abscisa the peak driving force. The curve for the 600 V pulse reports a strain at driving forces for which the 2 kV pulse does not yet show a response. Moreover, in both cases the extension seems to be smaller at given driving force than in the quasi-static case during the initial stage of the deformation. This kind of behavior is common to all pulsed-field data obtained here, and could be due to a number of factors:

- Eddy currents reduce the effective field inside the material. In this case, the field inside the sample could *a priori* lag behind the field outside of it. Since the latter one is measured, the difference between the curves in Fig. 4-1 could be explained with the use of a distorted abscissa. The problem is addressed in Sec. 4.2.1 below.

- The sample's mass causes the response to be inertial. As the twin-boundaries sweep across the sample, the atoms are displaced according to the twinning strain. As of yet untransformed material opposite the fixed end of the sample is displaced. This untransformed mass slows down the extension, because it can not adjust instantaneously to the value expected for the driving force at that moment. In Sec. 4.2.2 this effect is discussed.

- The partial dislocations responsible for the transformation of variants have to form and then move. In this scenario, barriers to the motion of the partial dislocations are overcome at a rate that depends on the barrier height (and in principle also on the temperature), so that in any case the dislocation break-away requires time to occur. A distribution of such barriers could exist. These barriers can be classified according to two broad categories. On the one hand are barriers associated with the Peierls energy, and with the energy associated with the formation of a partial dislocation loop[1]. These are intrinsic to the material. On the other, there is a spectrum of defects that pin existing partial dislocations and preclude further motion, which are extrinsic in nature. These are considered in Sec. 4.2.3.

[1] As mentioned before, twinning occurs as partial dislocations sweep across the twin plane.

A new perspective of the difference between quasi-static and dynamic actuation is provided by Fig. 4-2, which presents the *final* extension (data points) as a function of the peak driving force, together with the quasi-static extension (solid line.) Note that the extensions for the various pulses are obtained from a sample that is reset after each actuation.

In the quasi-static case the twin-boundaries presumably have time to reach a configuration where they are at equilibrium for the given driving force. For the set of final extensions for pulsed fields, on the other hand, it is not possible to say *a priori* that the twin-boundaries have reached equilibrium positions[2]. In fact, it has been shown [47] recently that the time dependence of the field-induced strain (at constant field) in Ni–Mn–Ga can be fitted by functions that have an exponential time dependence of the form $\exp(-t/\tau)$, where τ is of the order of 10 minutes. Consequently, the data sets in Fig. 4-2 are inherently different. In the end, it is a matter of mobility of the twin-boundaries whether or not they can follow the rapidly varying driving force during a magnetic field pulse (see Sec. 5.2.5.)

While the pulsed-field data in Fig. 4-2 has more scatter than the quasi-static data, there is a reasonable match between both data series, suggesting[3] that the final values of the displacement are weakly dependent on the rate at which the field is applied.

4.2 Factors that can control the extension process

4.2.1 Eddy currents and the field inside the ferromagnetic shape memory alloy

The values for the field inside the Helmholtz coil are obtained from the measured current, using the calibration procedure of Sec. 2.1.3. A Ni–Mn–Ga sample placed at the center of the coil is not necessarily exposed to the same field. While constant magnetic fields are not shielded by a conductor, time-varying fields do generate eddy

[2]Note the possible effects on the extension enumerated at the beginning of this section.

[3]If the final extension depended strongly on the rate at which the field is applied, a greater disparity between the two data-sets of Fig. 4-2 would be expected, especially at high fields.

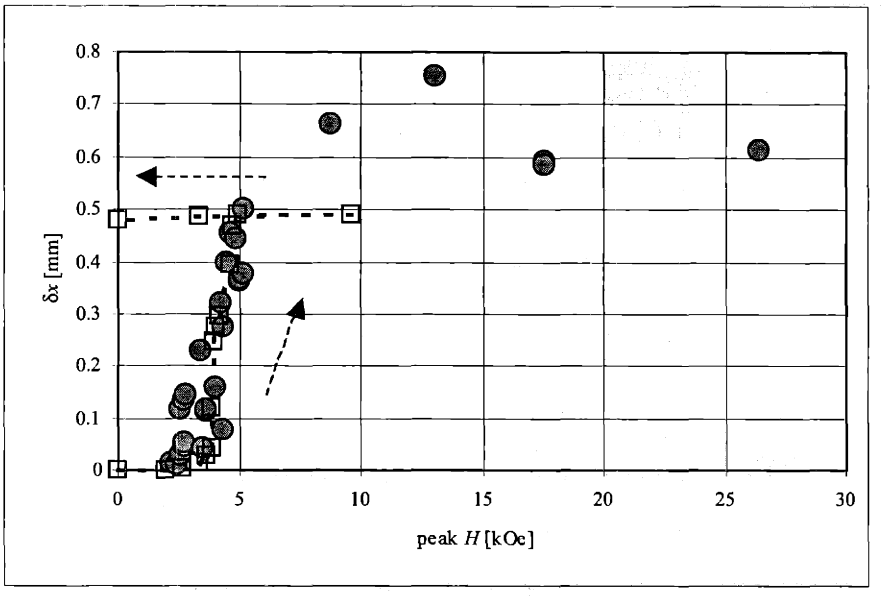

(a)

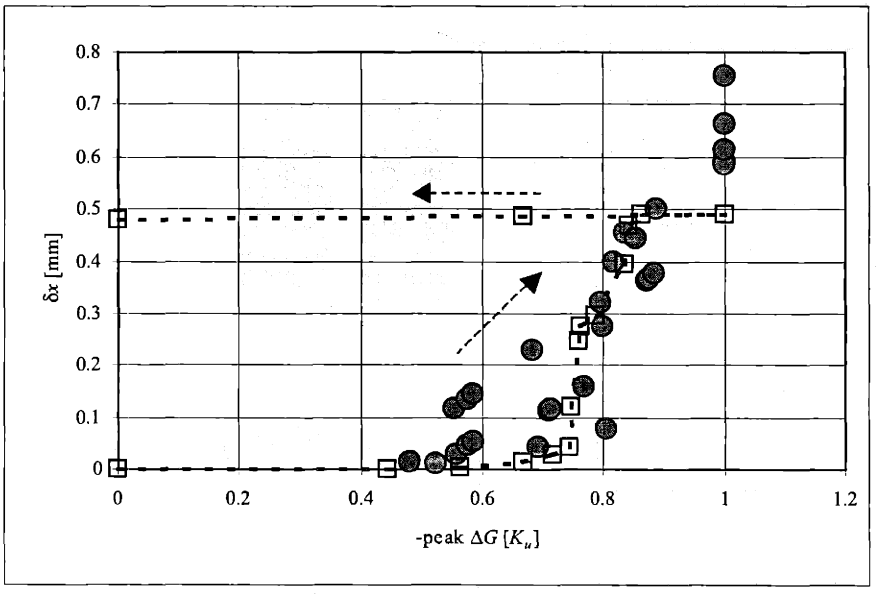

(b)

Figure 4-2: (a) Plots of the final extension δxvs. peak field H and (b) vs. peak driving force ΔG for various pulses (gray circles.) Note that after each pulse the crystal was reset. Superimposed are the results of Murray et al. [61] for quasi-static fields (empty squares and dotted lines.) The arrows indicate the direction in which the field in the quasi-static case was slowly varied (about 10 min between points.)

currents in it, and thus modify the applied field [62]. Ni–Mn–Ga's conductivity cannot be neglected (see Tab. 2.1) and could result in eddy currents inside the sample when the field varies with time. The effect has to be analyzed. A typical descriptor of the effect is the *skin depth*, the distance over which an electro-magnetic (EM) wave of given frequency in a linear conductive medium attenuates to $1/e$. It is defined as

$$\delta = \frac{c}{\sqrt{2\pi\mu\sigma\omega}} \quad \text{(cgs)} \tag{4.1}$$

where c is the speed of light, μ is the permeability in the material, σ is the conductivity in the material and ω is the frequency of the EM-wave (see App. B.1.) It is clear that the skin depth decreases with increasing frequency. A wave with frequency[4] $\omega_\tau = 2\pi/(2\times 620\,\mu\text{s})$ is thus expected to be attenuated by a factor $1/e$ after traversing 6.2 mm of Ni–Mn–Ga[5]. Nevertheless, the time-dependence of the field generated in the pulsed-magnetic field experiment is not fully characterized by a sinusoidal EM-wave. The exact description of the magnetic field inside the crystal requires considering the sample's finite dimensions and the non-linear susceptibility. Because of the non-linearity, superposition of plane waves cannot be used *a priori* to obtain a solution. However, a qualitative understanding of the effect of eddy currents in the experiment can be gained from a simplified problem, as follows. Consider a semi-infinite volume of ferromagnetic shape memory alloy with easy axis aligned along the $\hat{z}$ axis, and extending over all $x \geq 0$, y, z. A field applied in the $\hat{z}$-direction will not change the magnetization (its ferromagnetic part, that is) because it is already aligned with the field. In this case the susceptibility becomes the susceptibility of vacuum and the fields in that (and only that) direction can be described as a superposition of plane-waves[6] with magnetic vector aligned with $\hat{z}$.

From Sec. B.1 it is possible to find an approximate value for the field inside the semi-infinite volume when the empty space on $x < 0$ sees a pulsed magnetic field as in the present experiments. Figure B-3 shows the field evolution inside a material having the conductivity of Ni–Mn–Ga. It is important to note two points in this

[4] This is a representative frequency in the spectrum of the field-pulses used in this work.
[5] Compare this value to the thickness of the samples, about 5 mm.
[6] Transverse electromagnetic waves.

regard. First, the field at the center of the material lags the field at the surface. Second, there can be a significant field amplitude inside the material even though the pulse has subsided outside, and it can persist for about twice the pulse duration.

It is possible to find a correction (hereafter referred to as *skin-depth correction*) to the pulse shape obtained from the field in air by analyzing the difference between the latter and the average field across the sample thickness. Figure 4-3 shows a modified version of Fig. 4-1. The extension vs. driving force shown in Fig. 4-1 is

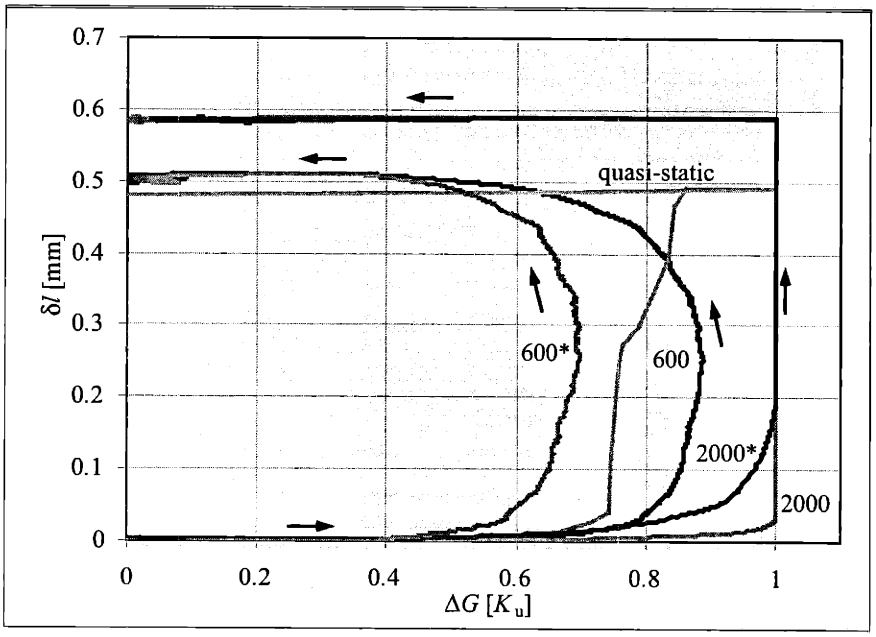

Figure 4-3: Real time plots of the extension δx vs. driving force ΔG for a 2 kV pulse and a 600 V pulse from Fig. 4-2(a), and the same data plotted vs. the corrected field (as per Eq. (B.37), see Sec. B.3), labelled 600 V* and 2000 V* respectively. The effect of the eddy currents is to lower the effective field inside the sample.

reproduced together with the extension vs. $\langle H \rangle_{\text{thickness}}$, the average field inside the material, as inferred from the measured field and the procedure detailed in App. B (curves with superscript "*".) The extension curves are shifted to lower fields, and in particular the onset field resembles more the data obtained in the quasi-static case (considering a possible small disparity with the threshold field of the quasi-static data[7]). Nevertheless, in the case of weaker pulses (600 V) it would seem that the correction is excessive. Notice that the correction gives a lower bound for the field

[7]This data was obtained with a different crystal of similar dimensions [61].

inside the material, because it is obtained assuming that the field penetrates the sample on a single face[8].

Figure 4-4 displays the extension vs. the peak driving force and the average driving force, along with the data from [61]. Again it is apparent that the correction is

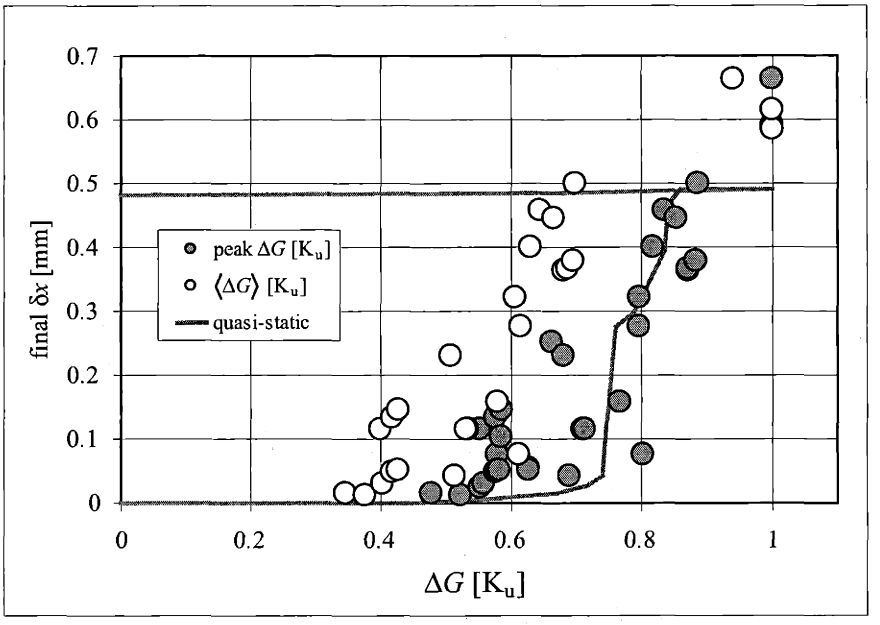

Figure 4-4: Plots of the final extension vs. the peak driving force (for various pulses) in filled circles. The same data is plotted vs. the average driving force (with empty circles, which includes skin-depth correction.) The line represents the quasi-static data from [61].

excessive.

This means that the field inside the Ni–Mn–Ga sample closely resembles the field in air. A direct implication for the design of Ni–Mn–Ga-based actuators is that in samples of about 5 mm thickness the effect of eddy currents can be neglected in a first approximation for frequencies of up to $\omega \simeq 5\,\mathrm{kHz}$ or pulse rise times greater than $620\,\mu\mathrm{s}$.

[8]This is because the model assumes a semi-infinite conductor.

4.2.2 Sample inertia

The objective of this section is to estimate the effect of the mass of the crystal on the speed at which the extension can occur. A simple Newtonian equation of motion for the center of mass of the crystal can be proposed as follows.

Consider the arrangement of Fig. 4-5. It depicts a slab of Ni–Mn–Ga of thickness

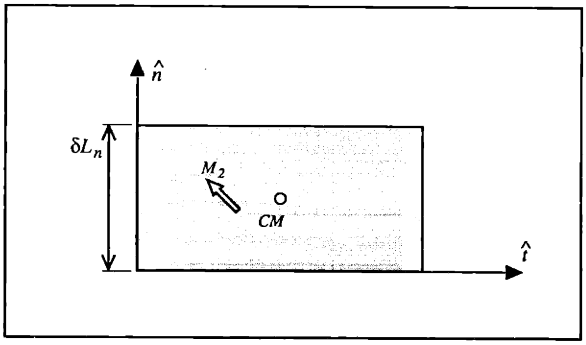

(a)

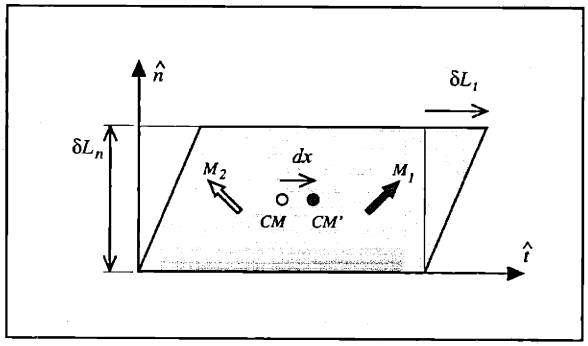

(b)

Figure 4-5: (a) Schematic of a crystal piece of thickness δL_n. CM is its center of mass and M_2 its magnetization. $\hat{n}$ and $\hat{t}$ are the twin plane normal and twinning direction respectively. (b) $dx\,\hat{t}$ displacement of the center of mass from CM to CM' when a fraction $\chi = \Delta L_n / L_n$ of material is twinned. The top right tip of the crystal piece is displaced $\delta L_t\,\hat{t}$.

δL_n, with its center of mass at CM, and a magnetization M_2. The base of the slab is a twin-boundary, and thus the slab can shear under the action of a field of suitable intensity and direction as the twin-boundary moves vertically. The twinning shear will involve atomic motion along the twinning direction $\hat{t}$ (of a magnitude proportional

to the distance to the base.) In that case the center of mass will experience a shift of dx to the right, taking on the position CM'.

Imagine that for $\delta L_n \simeq d_{(202)}$ this process were allowed to happen quasi-statically[9], by pulling from the center of mass in direction $-\hat{t}$ with strength f, exactly balancing the magnetic forces that cause the twin-boundary motion. With A, the area of the base of the slab, and the volume fraction χ of material that transformed to the reciprocal twin, it is[10]:

$$\begin{aligned} f dx &= \delta W = \Delta G V \frac{d\chi}{dx} dx \\ \Rightarrow f &\simeq \frac{\Delta G A}{\epsilon_o} \end{aligned} \tag{4.2}$$

where ϵ_o is given in Eq. (1.1). Thus, the driving force for twin-boundary motion calculated in Chapter 1 is related to the force f on the center of mass of a slab of Ni–Mn–Ga next to a twin-boundary through Eq. (4.2). The forces on all the twin-boundaries of the crystal will ultimately cause its center of mass to move as if the sum of the forces on the twin-boundaries were applied to it. In other words, for n_t mobile twin-boundaries,

$$\ddot{x} = \frac{\Delta G}{\rho \epsilon_o} n_t \tag{4.3}$$

Based on the measured or modelled ΔG, it is straightforward to solve Eq. (4.3) for a given number of mobile twin-boundaries. Because these results must be compared with a measured quantity, i.e. the extension, an expression that relates x_{CM} with the displacement ΔL_t of the top right tip of the crystal has to be obtained. This depends, of course, on the number of mobile twin-boundaries n_t and their position along the crystal.

Consider the case of a single mobile twin-boundary ($n_t = 1$), and assume that it is originated at one of the ends of the crystal. Figure 4-6 describes the two possibilities.

[9]This means that the kinetic energy can be neglected.

[10]Calculating δW at any point of the shearing stress requires a detailed description of the mechanism. Instead, it is possible to obtain an estimate for the average force needed to shear a mono-layer twin, by rewriting the expression when dx is the displacement corresponding to the twinning shear.

In Fig. 4-6(a) twin-boundary motion proceeds by the downward motion of a twin-

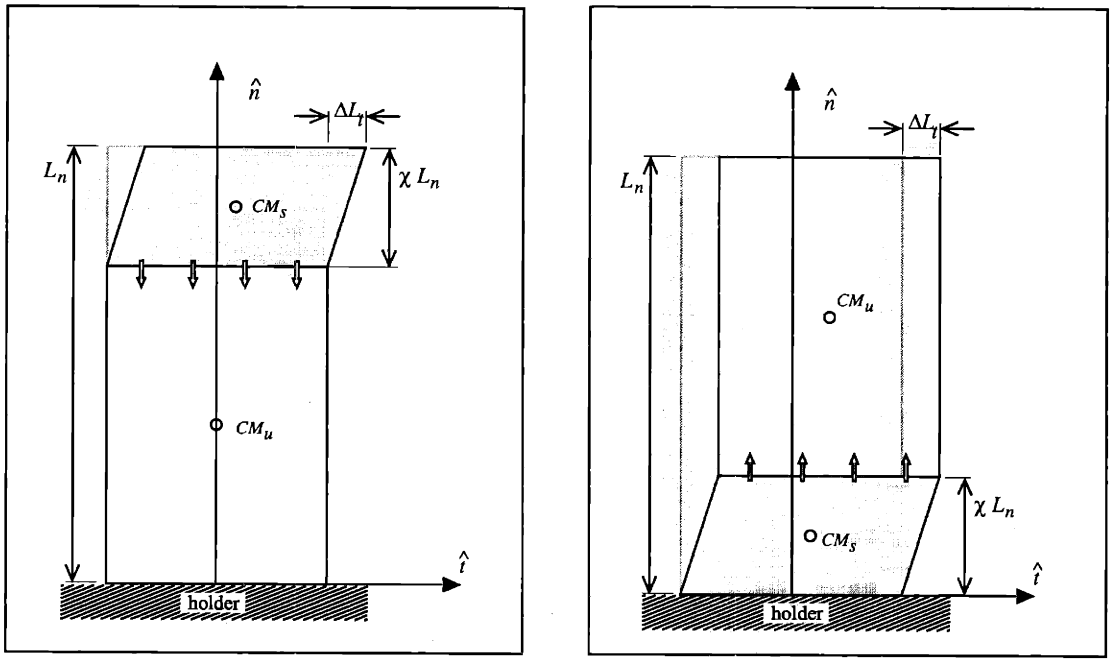

(a) "top case"

(b) "bottom case"

Figure 4-6: Two possible positions of a single mobile twin-boundary in a crystal of Ni–Mn–Ga. In (a) twin-boundary motion proceeds by the motion downward of a twin-boundary. Only the center of mass CM_s of the sheared volume fraction is displaced. In (b) twin-boundary motion proceeds by the motion upward of a twin-boundary. The center of mass CM_u of the untransformed volume fraction is displaced by the same amount as the tip of the sheared volume fraction, twice the amount that CM_s was displaced.

boundary generated at the free end. This will be referred to as the *top case*. The center of mass (CM_s) of the sheared region (a volume fraction χ of the crystal of height L_n) has moved a distance $\chi L_n \epsilon_o$, and the untransformed volume fraction did not move. In Fig. 4-6(b) twin-boundary motion proceeds by the motion upward of a twin-boundary generated at the holder. This will be referred to as the *bottom case*. In this case the sheared region's center of mass CM_s is displaced by $\chi L_n \epsilon_o$, as in the previous case. However, the center of mass of the untransformed part is displaced as well, by $2\chi L_n \epsilon_o$.

The center of mass of the crystal is therefore:

$$x_{CM} = \begin{cases} \epsilon_o L_n \chi^2 & \text{top case} \\ \epsilon_o L_n (2\chi - \chi^2) & \text{bottom case} \end{cases} \tag{4.4}$$

where naturally $\chi \in [0, 1]$. Equivalently, the volume fraction transformed as a function of x_{CM} may be obtained,

$$\chi = \begin{cases} \sqrt{\frac{x_{CM}}{\epsilon_o L_n}} & x_{CM} \leq \epsilon_o L_n, \text{ top case} \\ 1 - \sqrt{1 - \frac{x_{CM}}{\epsilon_o L_n}} & x_{CM} \leq \epsilon_o L_n, \text{ bottom case} \\ 1 & x_{CM} > \epsilon_o L_n \end{cases} \tag{4.5}$$

With these equations, the displacement of the tip of the crystal, ΔL_t is readily computed as:

$$\Delta L_t = 2\epsilon_o L_n \chi \tag{4.6}$$

It is now possible to plot the time elapsed since the pulse onset at which the extension reaches a threshold value of 0.005 mm, since it is directly related to ΔL_t:

$$\delta x = \Delta L_t \sin \alpha \tag{4.7}$$

where α is the angle that the twin plane subtends with the crystal's long axis, (see Fig. 2-18) and L_n accordingly becomes $L_n = L \cos \alpha$. Figure 4-7 shows the onset time expected from the model for the top case (t_o^{top}) and bottom case (t_o^{bottom}), superimposed on the data from Fig. 3-11 (discrete points.) Figure 4-7 actually describes the influence of two factors on the field-dependence of the onset time. One is the time t_{th} it takes the field to reach the threshold value for twin-boundary motion, 1.5 kOe. The other is the position along the crystal's long axis where twin-boundary motion starts. This defines lower and upper bounds for the onset time in the case of a single mobile twin-boundary (the top and bottom cases respectively.) Note that the driving force increases linearly with the number of active twin-boundaries, resulting in an acceleration of the center of mass of the crystal, and corresponding lowering of the

onset time. It can be assumed that the number of twin-boundaries that can move at lowest driving forces is small. This explains the good agreement with experiment, since only onset-times are considered.

Note that there are no fitting parameters in the model. It is also possible to introduce a modification in the model and set the threshold field to 2 kOe. In that case Fig. 4-8 is obtained. It is apparent that with the modification the model brackets the data better. The discrepancy between the threshold field measured and the numerical value that better brackets the data is not yet understood, but could be attributable to an uncertainty in the measurement of the threshold field.

These results suggest that the most important factor limiting the onset of the extension in the sample studied is the mass inertia.

4.2.3 Formation and pinning of twin-boundaries

The motion of the twin-boundaries in the direction of the twin plane normal[11] occurs through the expansion of partial dislocation loops[12]. The mechanisms governing the motion of these partial dislocations will therefore affect the motion of the twin-boundary.

Although having a driving force for twin-boundary motion implies a driving force for the motion of the partial dislocations, other driving forces not accounted for so far also affect their motion. In particular, energy is spent in the creation of a partial dislocation loop[13], because atoms are displaced from their equilibrium positions against the action of a force. It means that the partial dislocation loops have to be nucleated[14]. It is thus conceivable that even though a driving force for twin-boundary motion exists, the actual twin-boundary motion will only occur when sufficient "suc-

[11]Throughout this document the twin plane normal has been labelled $\hat{n}$. It corresponds to the direction [101], which is the normal of the (202) planes of the austenitic $Fm\bar{3}m$ lattice.

[12]The Burgers vector is a displacement along the twinning direction $[\bar{1}01]$, of magnitude $2\epsilon_o d_{(202)} \simeq 1.5\,\text{nm}$.

[13]There is a line-tension associated to the partial dislocation, and a surface energy associated to the stacking fault concurrently created.

[14]Nucleation is governed by hetero-phase fluctuations, the rate at which nucleation *attempts* take place, and the fraction of such attempts that creates a stable partial dislocation loop. Temperature greatly affects these rates, and one can refer to these as thermally activated processes.

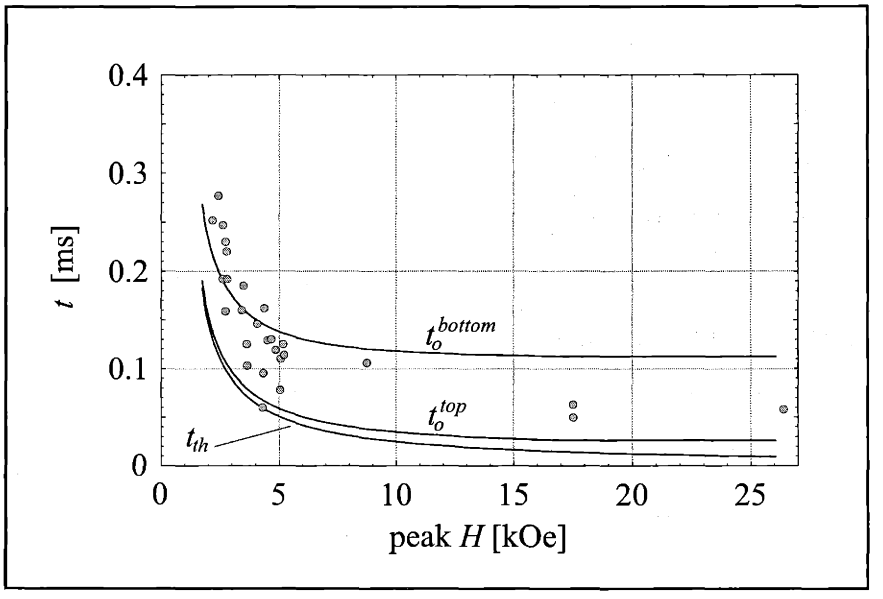

(a)

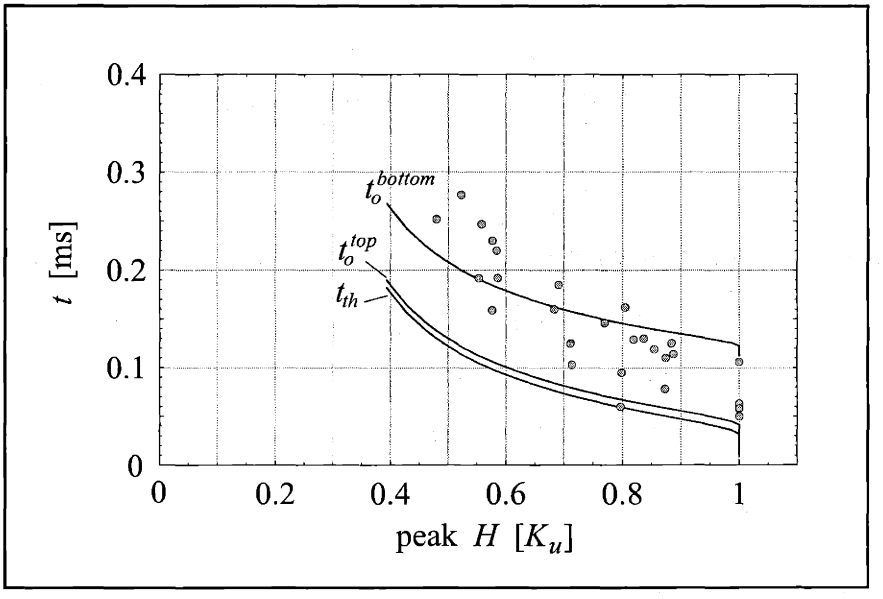

(b)

Figure 4-7: (a) Onset time vs. peak field and (b) onset time vs. peak driving force for various pulses and for the model of this section. The discrete points are from Fig. 3-11 and the continuous lines are the model result.

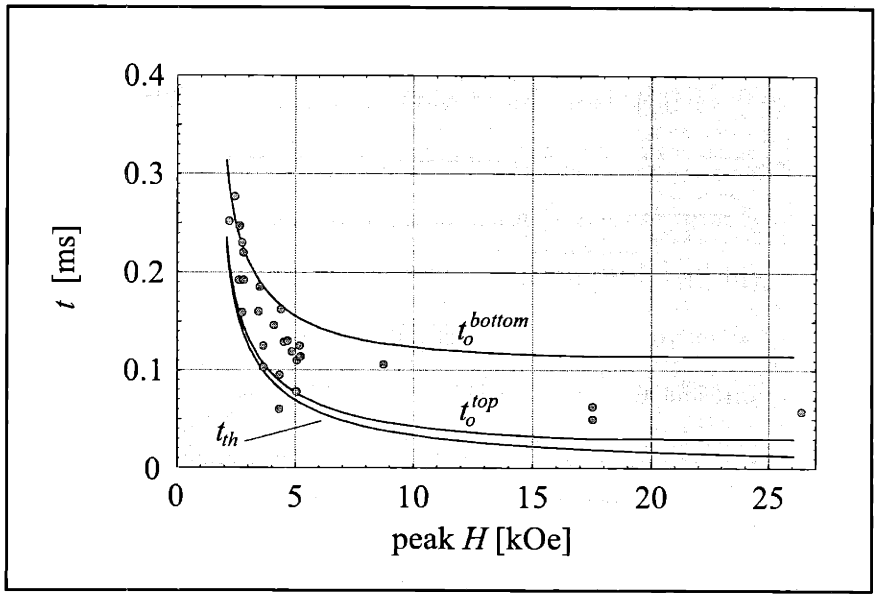

(a)

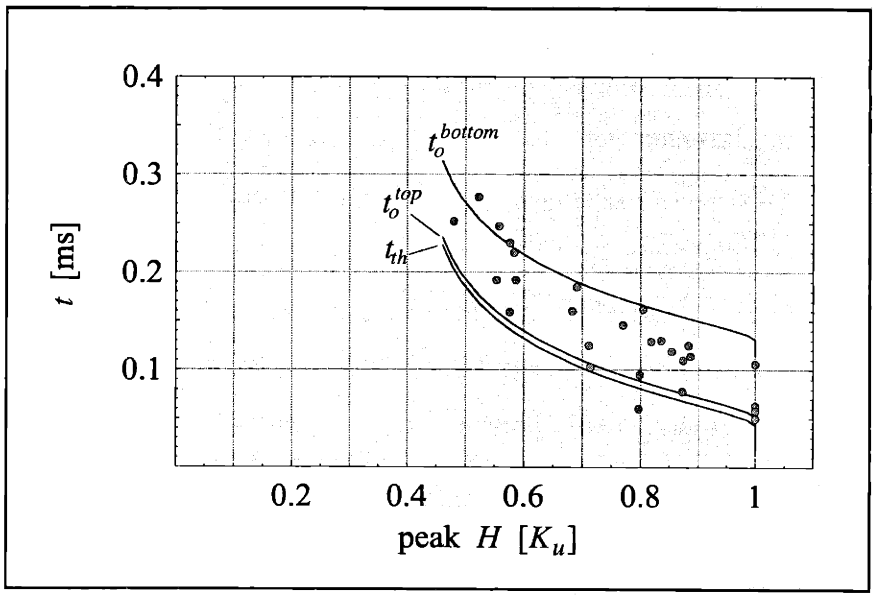

(b)

Figure 4-8: (a) Onset time vs. peak field and (b) onset time vs. peak driving force for various pulses and for the model of this section. The discrete points are from Fig. 3-11 and the continuous lines are the model result, for $H_{th} = 2\,\mathrm{kOe}$.

cessful" nucleation attempts have occurred.

Forces not yet considered in this discussion could act on partial dislocation loops that have already been nucleated. Such is the case of *pinned* partial dislocations that are precluded from further motion even though there exists a driving force for twin-boundary motion[15]. Once again, overcoming the energy barrier represented by the pinning obstacle requires work, and the rate at which attempts to overcome the barrier take place will be of importance.

It is necessary to estimate the impact that these processes have on the twin-boundary velocity and the rate of extension of the crystal.

4.2.4 Partial dislocation average velocity and twin-boundary velocity

In their 1959 paper, Johnston and Gilman [64] were able to estimate average dislocation velocities and densities in lithium fluoride single crystals after applying stress pulses of varying intensity and duration by observing the displacement of etch pits at the dislocations' intersection with the crystal surface. The magnetic field pulses applied to the Ni–Mn–Ga single crystals in the experiments here described also result in plastic flow, but it occurs by the motion of a different kind of defect, viz. twin-boundaries. It was mentioned[16] that these advance in direction $\hat{n} \equiv [101]$ when partial dislocations with Burgers vector along $\hat{t} \equiv [\bar{1}01]$ nucleate and expand on (202). They cannot be observed directly in the present experimental setup however, so a comparison with [64] is not possible.

A way to obtain estimates of the velocities of the partial dislocations is to relate the measured the rate of extension of the crystal v to the average twin-boundary velocity $\overline{v}^{tb}$, and by extension to the partial dislocation average velocity, $\overline{v}^{\perp}$. The meaning of these different velocities is clarified in Fig. 4-9. As indicated, the rate of extension v is the time derivative of the extension of the crystal. It is parallel to the

[15] See for example [63].
[16] See also App. C.

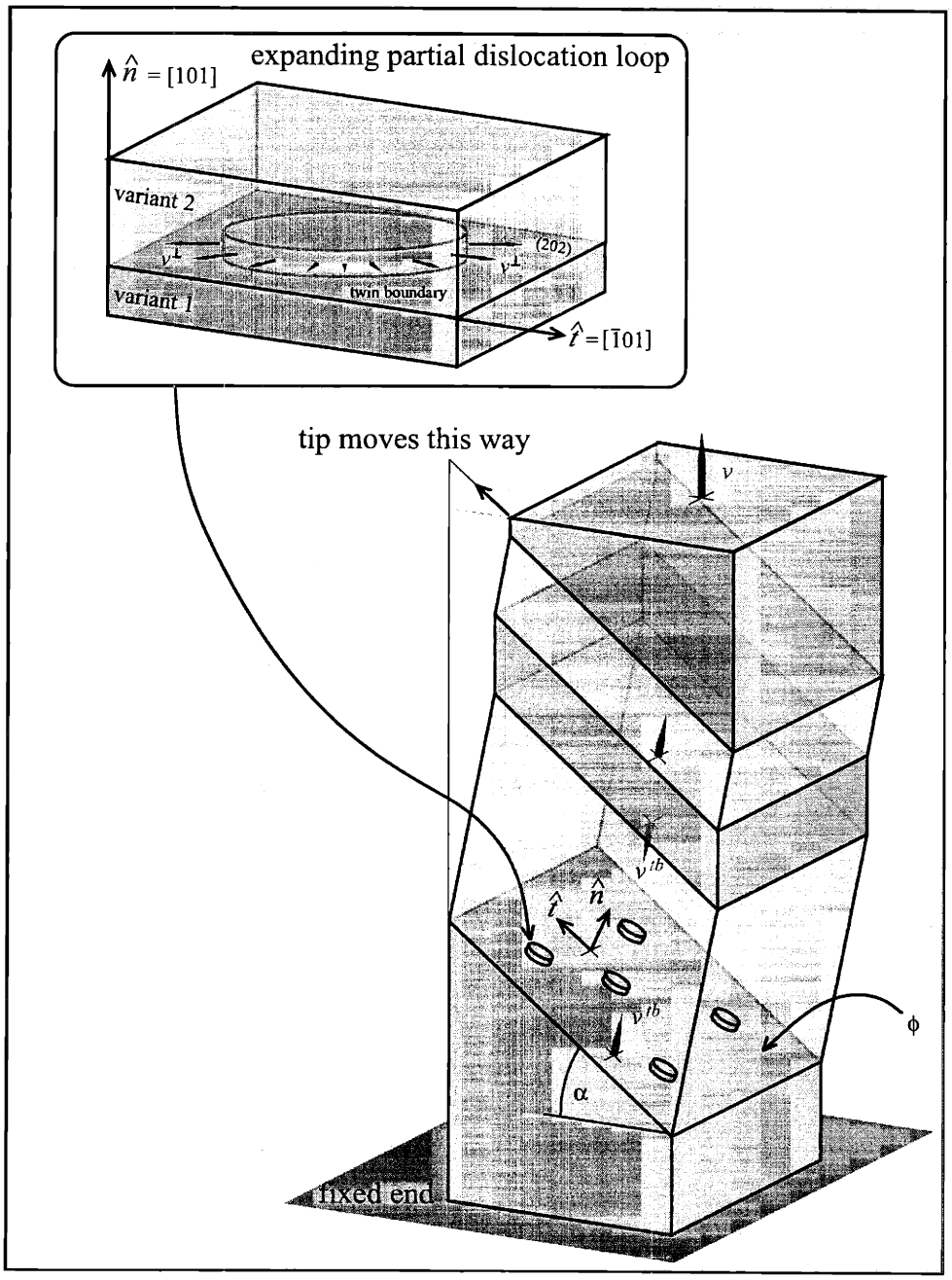

Figure 4-9: Schematic of the relation between the rate of extension v, the twin-boundary velocity $\overline{v}^{tb}$ and the partial dislocation average velocity $\overline{v}^{\perp}$. v is the time derivative of the extension of the crystal. $\overline{v}^{tb}$ is the twin-boundary velocity, normal to the twin plane. $\overline{v}^{\perp}$ is the velocity of the partial dislocation loops as they expand on the twin plane.

crystal long axis. The atomic motion during the movement of a twin-boundary occurs along the twinning direction $\hat{t} \equiv [\bar{1}01]$. Consequently, the free end of the crystal will be displaced in that direction, an amount δL_t (see Fig. 4-6.) It can be seen that v is related to this displacement by the relation:

$$v = \sin\alpha \frac{d\Delta L_t}{dt} \tag{4.8}$$

The clear regions in Fig. 4-9 are twin bands, whose borders define the twin-boundaries. Some of the twin-boundaries may be mobile at given time and move in direction $\pm\hat{n} \equiv \pm[101]$ by an amount ΔL_n. This is the basis for the relation between v and $\overline{v}^{tb}$:

$$m\,\overline{v}^{tb} = \frac{d\Delta L_n}{dt} \tag{4.9}$$

where the assumption was made that there are m mobile twin-boundaries and that the twin bands are inclined by an angle α (see Fig. 4-9)[17]. A motion ΔL_n of the twin-boundaries can only occur through the transformation of twin variant 2 into twin variant 1 through the twinning shear, so that the displacement $\Delta L_t = 2\epsilon\,\Delta L_t$ occurs. Consequently,

$$v = (2\epsilon_o m \sin\alpha)\,\overline{v}^{tb} \tag{4.10}$$

To obtain a relation between $\overline{v}^{\perp}$ and $\overline{v}^{tb}$, it is convenient to consider the time employed by a twin-boundary to move the distance between consecutive (202) planes, $\delta t_{(202)}$, which his simply:

$$\delta t_{(202)} = \frac{d_{(202)}}{\overline{v}^{tb}} \tag{4.11}$$

$\delta t_{(202)}$ can be equated to the time required by partial dislocations to completely sweep out a twin plane. It is assumed that the same average number $\mathcal{N}$ of partial dislocations is created on every (202) plane that is crossed by the twin-boundary. In the absence of homogeneous field-induced nucleation (see Sec. C.1.1) this is reasonable because partial dislocations are annihilated after expanding and covering the sample's

[17]Usually 45° in applications that seek to obtain an as large as possible extension, as is the present case.

twin plane area[18]. The boundary of the partial dislocation loop is assumed to expand at constant velocity $\overline{v}^{\perp}$. In time $\delta t_{(202)}$, each loop will have swept out a twin-boundary area equal to $\pi(\overline{v}^{\perp}\,\delta t_{(202)})^2$, so that $\mathcal{N}$ loops will have swept out the entire the twin plane area ϕ (see Fig. 4-9.) Consequently,

$$\delta t_{(202)} = \sqrt{\frac{\phi}{\pi\mathcal{N}}}\frac{1}{\overline{v}^{\perp}} \tag{4.12}$$

From Eq. (4.11) and Eq. (4.12),

$$\overline{v}^{\perp} = \sqrt{\frac{\phi}{\pi\mathcal{N}d_{(202)}^2}}\,\overline{v}^{tb} \tag{4.13}$$

Equation (4.13) together with Eq. (4.10) furnishes the desired relations between the velocities. It can be useful to write the relation between $\overline{v}^{\perp}$ and v explicitly:

$$\overline{v}^{\perp} = \underbrace{\left(\frac{\sqrt{\phi}}{2\sqrt{\pi}\,\epsilon_o\,\sin\alpha\,d_{(202)}}\right)}_{\equiv A}\frac{v}{m\sqrt{\mathcal{N}}} \tag{4.14}$$

where the numerical value of the constant A is evaluated to be 2.1×10^9.

It is instructive to consider Eq. (4.13) from a different point of view. Suppose there is a single mobile twin-boundary ($m = 1$), and that a single partial dislocation loop is formed during the time δt ($\mathcal{N} = 1$.) With a rate of extension of about 300 cm/s that partial dislocation front would have to move at speeds[19] of the order of $6 \times 10^{11}\,\mathrm{cm\,s^{-1}}$ which proves that $\mathcal{N} \gg 1$.

Conversely, the value of $\mathcal{N}$ can be estimated when the partial dislocations move at the speed of sound in Ni–Mn–Ga, some $\sqrt{E_Y/\rho_{\mathrm{NiMnGa}}} \simeq 2.9 \times 10^4$ cm/s. At the same rate of extension it follows $\mathcal{N} \simeq 4.8 \times 10^{14}$, which appears to be an unusually large number. As can be seen from a quick estimate[20] it is about three orders of magnitude

[18]When partial dislocation loops "touch" each other coalesce.

[19]i.e. $\overline{v}^{\perp}$.

[20]$\mathcal{N}$ is the number of loops existing on the plane of area ϕ. Roughly $\sqrt{\mathcal{N}}$ loops will be crossed by a line of length $\sqrt{\phi}$. Etching a surface perpendicular to the twin plane and parallel to the line would reveal $2\sqrt{\mathcal{N}}$ etch pits, that is, 8.6×10^7 pits per cm. In comparison, the square root of dislocation

larger than in heavily cold worked metals. The real number of partial dislocations is likely to be smaller (because of annihilation and because not all loops are created at the same instant).

The reason such large values for $\mathcal{N}$ are obtained is the assumption that twin planes are swept out sequentially. In fact, it would be possible for partial dislocations to nucleate on (202) planes immediately above an expanding loop, since the faulted area inside the loop constitutes the local twin-boundary. Several consecutive twin planes could be transformed concurrently.

A method to account for this effect is outlined in Sec. C.4. With it, the values of the N required for given $\overline{v}^{\perp}$ would be smaller.

In conclusion, the estimates of the prior section show that a magnetic field can move existing twin-boundaries but not form new ones inside a single variant. There is a large number of partial dislocations concurrently sweeping out a given twin plane. Furthermore, the picture of an interface between twin variants comprising a single crystal plane across the crystalline sample has to be abandoned when it is desired to relate the average velocity to the rate of extension. Instead, the twin-boundary comprises several successive twin planes which are swept out by partial dislocations at the same time.

Expression for the average velocity

In the previous section the nucleation mechanism as rate of extension-limiting process was discussed. It is also possible to consider the case where nucleation is not the limiting mechanism. As discussed in Sec. C.3 dislocations are pinned at defects, and depending on the defect pinning strength, the dislocations could remain immobile for a significant portion of their overall movement. To resume motion once pinned, a dislocation needs to overcome the energy barrier represented by the defect. This is a thermally activated process.

Let us consider a single active twin-boundary and faults expanding on it. It can

densities of heavily cold worked metals [65] is of the order of 10^6.

be shown[21] [66] that even though there exist a variety of defects and pinning barriers, the partial dislocation average velocity $\overline{v}^{\perp}$ still follows an exponential law for the driving force:

$$\overline{v}^{\perp} = \overline{v}_o^{\perp}\ e^{-\Delta G^{\ddagger}/kT} \tag{4.15}$$

Here $\overline{v}_o^{\perp} \simeq \frac{\overline{\lambda}\, b\, \nu_D}{\overline{l}_{\sigma,T}}$, being: $\overline{l}_{\sigma,T}$ the average distance between pinning sites on the dislocation line, b the Burgers vector of the partial dislocation, ν_D the Debye frequency of the crystal, $\overline{\lambda}$ the average distance from the energy valley to the saddle point of activation, and $\Delta G^{\ddagger}$ is the barrier height at the point of activation, also known as the *transition state* energy. This $\Delta G^{\ddagger}$ is given by the defect pinning strength $U_{barrier}$ and the driving force for twin-boundary motion, in this case:

$$\Delta G^{\ddagger} = U_{barrier} - V\Delta G \tag{4.16}$$

where V is the volume of material changing from one variant to the other (for the sake of definiteness $2 \rightarrow 1$) as the dislocation breaks away from the pinning site,

$$V = \overline{l}\,\overline{\lambda}\, d_{(202)} \tag{4.17}$$

Using the result from Eq. (4.14), the partial dislocation average velocity ($\overline{v}^{\perp}$) can be related to that of the advancing twin-boundary ($\overline{v}^{tb}$) simply as:

$$\overline{v}^{tb} = A^{-1}\overline{v}_o^{\perp}\ e^{-\Delta G^{\ddagger}/kT} \tag{4.18}$$

or likewise:

$$\ln v = C_1\Delta G + C_2 \tag{4.19}$$

both of which are exponential, and where the constants C_1 and C_2 are given by:

$$C_1 \;=\; -\frac{d_{(202)}\,\overline{l}\,\overline{\lambda}}{kT}$$

[21] See Sec. C.3.

$$C_2 = \ln\left(\frac{2\,d_{(202)}\overline{v}_o^{\perp}\epsilon_o \sin\alpha}{\sqrt{\phi}\,m}\right) + \frac{U_{barrier}}{kT} \tag{4.20}$$

where $\overline{v}_o^{\perp}$ must be given in the same units as rate of extension.

With these expressions in mind, the rate of extension data in Fig. 4-10 is reconsidered. It is apparent that the peak rate of extensions *can* be modeled with Eq. (C.55)

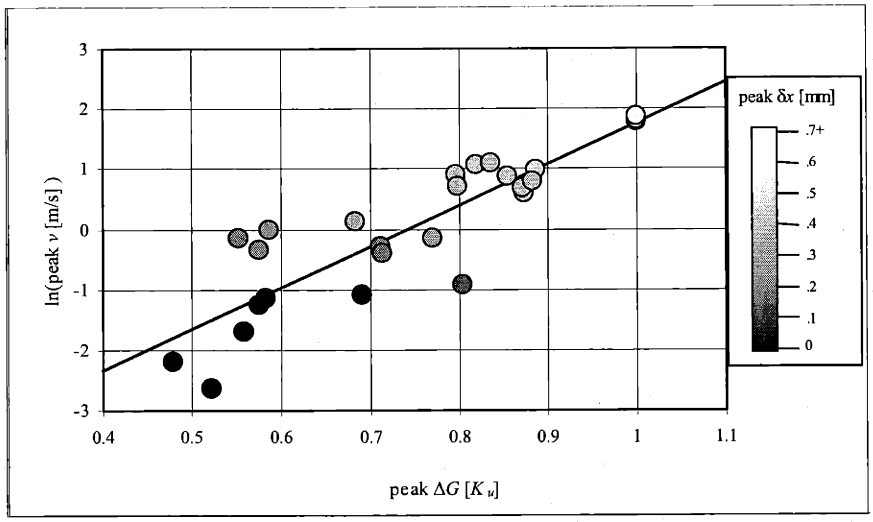

Figure 4-10: Plot of the logarithm of the peak rate of extension vs. the peak driving force. The gray level codes the final extension. The straight line through the plots is the linear regression of the data, yielding a slope of 13.2 $\frac{\text{cm}^3}{\text{erg}}$ and an ordinate of -5.1.

with constants $C_1 = 13.2\frac{\text{cm}^3}{\text{erg}}$ and an ordinate of $C_2 = -5.1$. Several factors contribute to the dispersion in the plot, but it must be pointed out that $U_{barrier}$ is an average barrier height pinning the partial dislocation during its motion.

This result is important on two accounts. First, it allows to obtain an effective mobility for the twin-boundary in the given sample and geometry as $\frac{\partial \overline{v}^{tb}}{\partial \Delta G}$. Second it indicates that the mobility is a non-linear function of the driving force (note the exponential dependence.)

Certainly, for small driving force one can expand the exponential in the law for $\overline{v}^{tb}(\Delta G)$, and obtain a mobility of $C_1\,e^{C_2}$ but the validity of such approximations is questionable given that the twin-boundaries remain pinned at low driving forces. This points to the fact that a small number of large pinning sites (in the sense of large $U_{barrier}$) is not contemplated in Eq. (C.53).

4.2.5 Initial conditions for the pulsed-field experiment

The deformation history of the sample will determine an evolution in the distribution of the pinning defects, both in terms of barrier heights, and their number and position in the crystal. Specifically, it is seen from [66] that the average rate $\overline{\nu}$ at which a partial dislocation overcomes a pinning barrier of height $U_{barrier}$ will be

$$\overline{\nu} = \nu_o \, e^{-(U_{barrier}+\Delta G)/(kT)} \tag{4.21}$$

so that the waiting time at the pinning site[22] is larger for greater barrier heights. It is also clear that it should decrease as the driving force is increased. This points out the relevance of the defects in determining the field-induced twin-boundary motion. Particularly, it is likely that $U_{barrier}$ and the spatial distribution of the pinning defects changes somewhat from one experiment to the other, contributing to the dispersion observed so far in the pulsed field-induced extension results. Evidence of this fact can be found from comparisons of the (macroscopic) twin-structure formed in Ni–Mn–Ga, as seen in Fig. 4-11. It is apparent that the evolution of the twin-bands changed with large number of actuation cycles. In Fig. 4-11(a) field-induced twins formed few, thick twin bands on the surface of the sample. This structure evolved into one with a large number of thin twin bands, as in fig 4-11(b). The field-induced actuation was almost completely suppressed at this point. A subsequent annealing process (see Sec. 2.2.2) "rejuvenated" the sample, restoring twin-boundary mobility with the field. The annealed sample can be seen in Fig. 4-11(c). Again, twins manifest as thick bands, few in number[23]. In this regard, it is to be pointed out that Henry [48] observed a degradation in the AC-performance after 10^3–10^5 cycles in a similar crystal. However, actuators without apparent performance degradation for a cycle number well in excess of 10^6 have recently been tested and produced [67]. This indicates that the characteristics of the pinning defects in the as-received crystals and their role in the generation of additional pinning defects is important.

[22] $1/\nu$ from Eq. (4.21).

[23] Note the different orientation of the twin bands when compared with images prior to annealing, Fig. 4-11(a) and Fig. 4-11(b).

With the same framework it is possible to understand some of the features in the series of photographs in Fig. 3-14. They are in accord with the notion that the likelihood of de-pinning has an exponential dependence on the effective barrier height $U_{barrier} - \Delta G$. If during the deformation process (stress- or field-induced twin-boundary motion) a partial dislocation is pinned, a reset attempt via a field (or, for that matter a stress) may not necessarily de-pin it, since a characteristic time is needed for the process to occur. The regions of the crystal that surround the twin plane of the pinned partial dislocation may reset however, so that no twin bands are immediately visible (cf. Fig. 3-14(a).)

When a pulsed field is applied to the sample, the pinned partial dislocation may find that at a sufficiently high field the effective barrier to its motion may decrease or disappear. Twin boundary motion then takes place, as the twin plane is swept out by the the partial dislocations and the process is repeated in subsequent twin planes.

Eventually the field will drop to a level that causes the motion of the partial dislocations at the twin-boundary to be pinned by effective barriers, and the twin-boundary motion will cease. As a new pulse (of the same height) is applied, the process is repeated.

A disparity from pulse to pulse in the lengths that a given twin-boundary advanced is understood as arising from the different barrier height of the defects that pin the partial dislocations at the onset of each pulse. In particular, it is conceivable that at peak fields of 2.2 kOe some pinning defects are able to pose an effective barrier to partial dislocation motion. This explains why irrespective of the number of pulses applied, some twin-boundaries did not move, while others did.

The degree of pinning of the twin-boundaries can increase with time, as was mentioned above. It is also possible that some twins have thinned during the resetting procedure, but did not completely disappear. This is analogous to the existence of *reversal domains* in ferromagnets [4], and would contribute to lowering the threshold field. Both effects could affect the outcome of a pulsed-field measurement, and contribute to the scatter observed.

At a given distribution of barriers in direction perpendicular to the twin plane, the

final crystal extension in this framework is determined essentially[24] by the maximum driving force supplied by the field.

As for the barrier distribution, it would appear from Fig. 3-14 that the twin-boundaries are pinned at relatively few[25] sites. In this case, the solutions provided by [66] will not be accurate because the ensemble of large pinning sites is too small and the probability distribution of their existence is not smooth.

4.3 Implications for the design of actuators

The results obtained from the pulsed-field experiments have implications for the design of actuators based on the ferromagnetic shape memory alloy Ni–Mn–Ga. The field of ferromagnetic shape memory alloys and Ni–Mn–Ga in particular has proven to be very fruitful since large magnetic field-induced twin-boundary motion was first reported [19]. However, the development of specific applications is still a nascent field. Major issues in the design involve the performance characteristics of Ni–Mn–Ga-based actuators vis-à-vis alternative "smart" technologies (such as ordinary shape memory alloys, magnetostrictive materials and piezo-electric materials) include switching times and energy consumption as well as stress output. In this regard the results from this work have implications in the design of the material and associated devices.

A first observation is that a full variant transformation is possible in under 1 ms with peak pulse-fields of order 5 kOe (Fig. 4-2(a)) for samples of approximate geometry $5.08 \times 5.08 \times 9.85\,\text{mm}$[26]. Secondly, the full transformation was achieved with the use of a pulsed field, and did not require maintaining a strong magnetic field over extended periods of time (minutes, [47].) A compact ($220\,\text{cm}^3$), light (air-core) Helmholtz coil was used. With the driving force for twin-boundary motion bounded

[24] If two separate pinning sites presented unsurmountable barriers to partial dislocation motion, and no active twin-boundaries existed between them, it is expected that the region between the defects would remain untransformed.

[25] Compared with the number of (202) planes where pinning could occur, which is of the order of 2×10^7.

[26] Fastest (full) twinning — $\simeq 250\,\mu\text{s}$ — was demonstrated with almost square driving force-pulses with rise times under $60\,\mu\text{s}$.

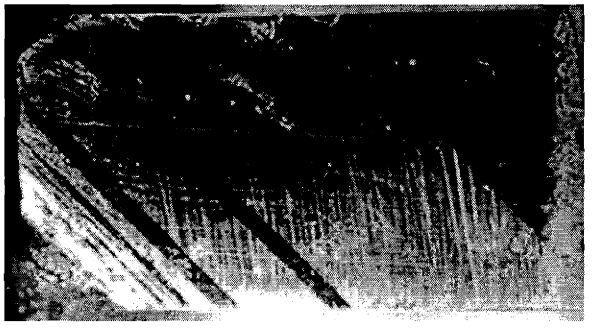

(a)

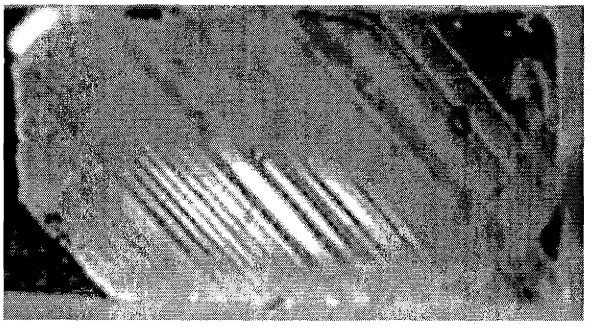

(b)

(c)

Figure 4-11: Figures of a crystal at different points of its deformation history. (a) Initial actuation from the as-received crystal. Notice the few, coarse twin bands. (b) after several actuation and reset cycles the twin structure has changed. Notice the profusion of thin twin lines. The overall extension is reduced significantly with respect to (a). (c) After the rejuvenation process described in Sec. 2.2.2 a twin-band structure similar to (a) is regained. The overall extension is also comparable. However, notice the different twin plane inclination with respect to the sample long direction.

by the magnetocrystalline anisotropy energy, it is seen that most of the 480 J of energy dissipated by the pulse does not contribute to the twin-boundary motion for the pulses that achieved the full transformation. Considering that the extension occurs in about half the pulse duration, and limiting the current to the value that saturates the driving force (about 880 A), only 43 J would be required.

It is also clear that the effective response of Ni–Mn–Ga crystals to an applied field would improve with the development of alloys with fewer and weaker pinning defects. Further, while at low fields the driving force for twin-boundary motion could be increased if the saturation magnetization M_s of Ni–Mn–Ga was increased, the driving force will saturate at a value equal to the anisotropy (K_u.) This suggests that in order to increase the blocking stress in Ni–Mn–Ga, alloys with larger magnetocrystalline anisotropy ought to be developed.

The mass of the crystal affects the ability of the material to quickly follow the applied driving force with an extension, as is evidenced by the field-dependence of the measured onset time. Reducing the size of the crystals would naturally improve the response, but at the expense of the extension, which is proportional to the length. Conversely, the forces accelerating the sample[27] could be increased. It has been established that increasing the field is ineffective beyond the saturation field. Nevertheless, notice can be taken of the fact that the force scales with the number of active twin-boundaries. Accordingly, seeding mobile twin-boundaries uniformly along the crystal length would increase the driving force and improve the crystal response. This calls for improved methods of "training" the crystal (cf. Sec. 2.2.1.)

4.3.1 Example: energy efficient field for twin-boundary motion

For simplicity, consider a step pulse of duration τ. As well, let the current i generating the magnetic field be constant during the duration of the pulse. The field will be

[27] $\frac{\Delta G}{\rho \epsilon_o}$.

proportional to the current[28]: $H = c_{cal} i$. Accordingly, the reduced field $\eta = \frac{M_s H}{2K_u} = \frac{c_{cal} M_s i}{2K_u} \equiv \eta_{cal} i$. Writing ΔG in terms of η, the extension will be given from Eq. (C.55) as:

$$\delta x = \int_0^\tau \overline{v}_0^{tb} \; e^{m \; \min[2\eta_{cal} i - \eta_{cal}^2 i^2, 1]} \; dt = \tau \overline{v}_0^{tb} \; e^{m \; \min[2\eta_{cal} i - \eta_{cal}^2 i^2, 1]} \tag{4.22}$$

When the circuit's resistance[29] is R, the total energy spent is simply

$$\Delta U = \tau R i.^2 \tag{4.23}$$

If a fixed energy U can be used for driving, a natural question to ask is what is the maximum displacement that could be achieved. It can be seen that the maximum displacement will be obtained for a current $\hat{i}$ lower than the one saturating the driving force, $i_{th} = 1/\eta_{cal}$.

$$\hat{i} = i_{th} \left(\frac{1}{2} + \frac{1}{2} \sqrt{1 - \frac{4}{b_2 i_{th}^2}} \right) \tag{4.24}$$

This suggests that the optimal current (in the sense of maximum extension per unit energy) is always below the saturation value. It reflects the fact that increasing the current (or the field intensity) will increase the driving force, and thus the elongation rate, but will deplete the energy faster.

The maximum displacement is, in this case:

$$\hat{\Delta x} = \frac{U}{R\hat{i}^2} \overline{v}_0^{tb} \; e^{m \; \min[2\eta_{cal} \hat{i} - \eta_{cal}^2 \hat{i}^2, 1]} \tag{4.25}$$

[28]The constant c_cal is obtained from the coil calibration. For the coil used in Chapter 3 it is $c_{cal} = 8.9 \, \frac{\text{Oe}}{\text{A}}$.

[29]In the present system it is about $0.195 \, \Omega$.

Chapter 5

Conclusion

5.1 Conclusions from this work

The large ferromagnetic shape memory effect in Ni–Mn–Ga was first reported in 1996 [28]. Since then up to 6% field-induced strain in single-crystal Ni–Mn–Ga samples, essentially the full transformation strain, has been demonstrated by various authors. However the future development of the material begins to depend more critically on the specific applications that can be found.

The work in this thesis has demonstrated the development of the full ferromagnetic shape memory effect of a Ni–Mn–Ga single crystal of $5 \times 5 \times 9.85\,\mathrm{mm}^3$ in $200\,\mu\mathrm{s}$ (This implies a stroke of $\approx 0.65\,\mathrm{mm}$.) These results prove the feasability of actuators operating at frequencies in excess of 1 kHz at room temperature for this geometry. Moreover, it has been shown that the actuation can be accomplished without employing massive magnets, using instead a compact air-core Helmholtz coil operated in pulsed mode. These are important achievements in that they expand the range of possible applications of Ni–Mn–Ga-based actuators.

The experimental apparatus developed here also allows the measurement of the magnetic field-induced extension with temporal accuracy in the order of few μs over a 1 ms time span. Fields of up to 27 kOe have been demonstrated in pulses lasting $620\,\mu\mathrm{s}$. The driving force for twin-boundary motion saturates at a field of 7.85 kOe and an additional field beyond this level is irrelevant. For pulses reaching $\approx 15\,\mathrm{kOe}$

the driving force profiles are close to square. The extension is detected optically and there is no mechanical coupling between the sample and the detector. Therefore sample-characteristic properties can be obtained without recourse to models of the interaction with the measurement device. Inasmuch, this work has produced a valuable experimentation tool.

It was found that pulses of $620\,\mu$s width experience only a small eddy-current attenuation in the Ni–Mn–Ga crystals of the geometry measured. Lamination of the Ni–Mn–Ga crystals does not appear to be necessary from this point of view.

The field-induced extension does not begin at the same time as the field. It was found that the delay in the onset of the field-induced deformation has two components. Firstly, there is a component due to the time it takes for the field to rise to the threshold level for actuation. Secondly, the mass-inertia of the sample results in an additional delay. This delay depends on the position of the twin-boundaries with respect to the fixed end of the crystal, as well as of their number, because the force that drives the crystal's extension is proportional to the number of twin-boundaries. The delay is maximum for a single twin-boundary moving from the fixed end of the crystal. Faster extension response to an applied field is obtained for twin-boundaries moving from the free end of the crystal toward the fixed end and for several twin-boundaries more uniformly distributed along the crystal. The peak acceleration observed is $50 \pm 10\,\mathrm{ms}^2$.

The field-induced creation of twin-boundaries through homogeneous nucleation of partial dislocations was found not to be possible for typical twin-boundary energies, of the order of $40\,\mathrm{erg/cm}^2$. Accordingly, to obtain a faster extension response to an applied field twin-boundaries would have to be seeded uniformly in the crystal through the action of a mechanical stress.

High speed video images have demonstrated that field-induced twin-boundary motion is not uniform along a Ni–Mn–Ga single crystal. The motion of discrete twin-boundaries has been inferred from photographs. It is shown that the motion of the twin-boundaries is interrupted when they reach certain positions of the crystal, and that they remain pinned there unless a sufficiently larger field is applied. Some

pinning positions have been identified with small cracks in the crystal. It is possible to relate the observed scatter in the data of field-induced extension to the existence of pinning sites.

Further, it is shown that the rate of extension can be expressed as an exponential function of the driving force, which reflects the average hindrance to partial dislocation motion imposed by many low-energy pinning sites. Accordingly the twin-boundary mobility (the relation between the rate of extension and the driving force) is not linear with the driving force. A relation between the rate of extension and the driving force makes possible the optimization of pulse profiles.

Pinning sites of large pinning strength appear in relatively few positions along the crystal length and cannot be described by the above approach. Their influence is more marked at low driving forces. The maximum rate of extension measured is 6 m/s for saturated driving force.

5.2 Suggestions for further research

The results from this work suggest possible lines of research.

5.2.1 Direct observation of partial dislocations and their pinning

It would be of great value for the design of Ni–Mn–Ga-based ferromagnetic shape memory alloys with improved twin-boundary mobility to have a direct confirmation of the partial dislocation pinning in the crystals, and the most relevant mechanism. TEM micrographs would allow to determine the most influential cause of pinning[1]. Possible candidates include retained austenite, second-phase precipitates from impurities, strain fields from imperfect ordering, dislocations, incompatible twin systems retained, voids and micro-cracks. Recently [67] crystals have been grown that show a yield stress of less than 1 MPa. A comparison could be made between the defects

[1] Account taken of the differences between electron-transparent areas and bulk material, so as to avoid thin-foil artifacts that are not characteristic of the bulk behavior.

observed in these crystals and in crystals previously employed, which showed yield strengths slightly larger than a MPa. Note that composition differences and varying compositional homogeneity have to be accounted for. It would also be interesting to compare the twin structure of the as annealed crystals with that of crystals that have undergone several actuation cycles.

In the same vein, an electron microscopy examination of the twin bands would allow it to be determined if the transformation occurred across the full thickness of the band or if untransformed regions remain interleaved, and whether micro-cracks are precluding further motion of the twin-boundaries.

Furthermore, TEM observation could provide measures of the stacking fault energy, to corroborate the conjecture that homogeneous nucleation of partial dislocations is not likely in these alloys based on energy considerations (cf Sec. C.1.)

5.2.2 Activation of twin-boundaries

In Sec. 4.3 it was mentioned that the onset of the extension would be expected to occur at earlier times provided mobile twin-boundaries were seeded in the crystal. The procedure with which this is usually accomplished is far from being standard. As indicated in Sec. 2.2 the crystal is subject to alternating stresses and fields, until the twin bands appear regularly throughout the crystal length. The conditions under which this occurs are not controlled. As a result, it is likely that defects[2] are introduced concurrently with the activation of the twin-boundaries. This offsets the benefit of introducing the twin-boundaries in the first place, and are in part responsible for the difficulty in resetting the sample with perfect repeatability[3].

The increased performance of Ni–Mn–Ga-based actuators would therefore require a controlled activation technique. To the extent that magnetic fields are incapable of nucleating twins homogeneously, stress will be the preferred activation method. A device capable of applying shear stresses in the $\hat{t}$-$\hat{n}$ plane needs to be developed.

[2]In the form of micro-cracks, dislocations, faults corresponding to twin planes other than the main activated one.

[3]The creation of defects is expected to be exacerbated by existing ones (micro-cracks in particular) that could concentrate stress or simply pin the partial dislocations.

5.2.3 Optimal sample size

Use of different sample cross sections

In the context of the present experiments the existence of pinning obstacles has been discussed. Their spatial distribution, as well as their strength, will ultimately determine the effectiveness of a field in producing twin-boundary motion.

How the mean distance of obstacles of given pinning strength compares with the sample cross section (measured parallel to the twin plane) could have an impact on the performance and reliability of a Ni–Mn–Ga based actuator. Specifically, the existence of a strong pinning obstacle at one point of the crystal length could effectively preclude the passage of a twin-boundary past it across the full width of the twin plane. Dividing the cross section in smaller pieces would free some pieces of the pinning obstacle, and result in improved overall performance.

This fact would become increasingly important as the volume of actuator material is increased to meet the output force demands placed on the actuator.

It is therefore important to consider the effect of sample size on the ability of Ni–Mn–Ga to support field-induced twin-boundary motion. At a constant driving force, the field-induced strain of single-crystalline samples and of bundles of several crystals adding up to the same cross section should be compared. The bundles should not be fitted very tightly together, lest they present blocking stresses to each other[4].

Ni–Mn–Ga polycrystals

So far the discussion has remained circumscribed to the single-crystalline samples employed. Polycrystalline Ni–Mn–Ga is in general easier to produce than single crystals, and the possibility of displaying a significant field-induced strain in them is of interest. In 2000 Pasquale et al. [68] showed 0.012% field-induced strain in a polycrystalline sample. The level of strain was raised to 0.29% in 2001 by Ullakko et al. [69]. These strains are far from the ones that have been achieved in single crys-

[4]Early attempts to produce field-induced strain with laminates failed. This could be due to inactive crystals, but was most likely due to having the laminates in tight contact.

tals (see Sec. 1.1), but the careful control of texture could improve the performance of Ni–Mn–Ga polycrystals. The texture dependence of the strain complicates the comparison of the field-induced extension of a polycrystalline sample with that of a single-crystalline one. Expressions for the lower and upper bounds to the strain have been found [70] in uniform crystals with linear programming. Analytic expressions for the texture-dependence of the upper bound for the strain in a polycrystal have also been found[5] [71].

It is interesting to experiment with different textures and compare the obtained values with the expected values from the analytical model. A better convergence of the measured value to the upper bound given by the model should be expected particularly for low effective stiffness, which is occurs in polymer-Ni–Mn–Ga composites recently developed [72–74]. Likewise, as pointed out by Bhattacharya, lowering the symmetry of the martensite particles (eg. from tetragonal to orthorhombic, which can be accomplished by tailoring the composition [41, 42]) should raise the Taylor (i.e. lower) bound for the overall strain, by providing a set of distinct compatible twin systems.

Based on these expressions, it would also be possible to quantify the amount in the polycrystal's strain that can be ascribed to texture, and therefore also if there is a benefit stemming from the reduced cross section.

5.2.4 Field inside the sample

The present work has outlined a method for obtaining a measure of the field inside the material based on strong approximations. It would be convenient to obtain a finite-difference[6] or finite-element solution to the propagation of the field inside the crystal. The result would be of increasing importance as the magnetic pulse length is made shorter.

In the event that this more detailed calculation yields corrections to the measured

[5] See App. D.

[6] Note the convergence problems. The condition on the finite differences Δt and Δx for time and position respectively ($\Delta t < \Delta x/c$) force us to use very short times. As well, it would be necessary to include in the model the fact that the twin-boundaries are not stationary.

Table 5.1: Alternative coil designs for the generation of sub-ms pulses.

Parameter/result	coil 1	coil 2	coil 3
duration [ms]	0.013	0.028	0.197
peak field [kOe]	10.8	13.7	35.1
radius [cm]	2.86	2.86	2.86
V [kV]	3	3	3
capacitance [μF]	40	40	360
loops per coil	2	4	10
AWG	20	10	16

field which continue to show that the field intensity at the center of the sample significantly lags the field in the outside, information can be obtained about the generation of the twin bands. Given that an extension *is* observed in the present experiments, one would conclude that the field near the sample surfaces is the driver for twin-boundary motion, and therefore that the latter is initiated at the sample surfaces.

5.2.5 Transient nature of the extension

As alluded to in Sec. 4.1, the pulsed-field experiments allow us to explore the characteristic times in the relaxation of a set of twin-boundaries toward equilibrium positions in the presence of a given driving force. In this work, the rates at which the driving forces were applied to the crystals was varied only by controlling the amplitude of the pulse. This approach does not fully benefit from the method in that the duration of the driving force has not been varied (except because in some cases the saturation was reached at earlier times), only its amplitude. The shortcoming is really only a matter of manufacturing coils capable of producing shorter pulses, for example with the designs suggested in Table 5.1.

One experiment that could be done is to subject the crystal to pulses that have the same driving force amplitude as a given pulse "V" from the present coil, but subside in a time shorter than the time for the onset of the extension in "V." In particular,

a field capable of saturating the driving force would provide the best comparison conditions since most pinning defects can be overcome in this case.

5.2.6 Barrier height spectrum

Following the discussion in Chapter 4, it would be important to assess the distribution and strength of the obstacles that pin partial dislocations. Two different experiments could be envisaged to obtain information about the barrier height and distribution.

Static fields

In one experiment, a Ni–Mn–Ga sample prepared as was indicated in Sec. 2.2 is placed in a DC magnetic field. Beginning with very small field intensities, the displacements following small field increments would be measured after any transients[7] subsided. It is expected, that when the driving force of the field exceeds that height of the lowest barrier, partial dislocations should move and an extension be observed. The extension would continue until a barrier of height exceeding the driving force is encountered, and then stop. A further increase of the field would be needed to get the twin-boundary to resume its motion.

The height of the field at which the extension is observed to occur will determine the height of the barriers, and the extension between pinning events (at different fields) would give a mesure of the spacing between barriers of comparable height.

Work in this direction is already under way.

Pulsed fields

The above experiment would provide a sort of "envelope" for the barrier energy distribution. Once a barrier of given height is overcome, the partial dislocations would move beyond the lower energy pinning obstacles without getting pinned. Ideally, it would be convenient for the partial dislocations to stop right after overcoming an obstacle of given strength, so that the field can be lowered again, and the exact height

[7] See [47].

of the next barrier can be assessed. One way to achieve this is with a succession of very short magnetic field pulses. The present work has shown that applying a saturated driving force for a few hundred μs is capable of essentially transforming the crystal of 250 mm^3 fully. Shorter pulses would be needed so as to preclude the long range motion of the twin-boundaries. With the present power source, a few coil designs can be proposed that could provide pulses that are almost two orders of magnitude shorter than the present ones (See Table 5.1.)

In the experiment, magnetic field pulses would be applied to a crystal without resetting, beginning with a low-intensity pulse (1.5 kOe peak intensity.) The field intensity would be increased in subsequent pulses until a extension is recorded. If that happens, the next pulse should be again a weak one. The distance between pulses would be a measure the distance between pinning sites, and the peak field that caused the extension the barrier height.

The equivalence between magnetic field- and stress-originated driving forces could perhaps be exploited. In this case the magnetic field pulses could be replaced by stress pulses obtained from other actuators.

5.2.7 Temperature dependence of the extension

To date, the temperature dependence of the field-induced twin-boundary motion has received little attention. It has been studied in the quasi-static case [75, 76]. In the present experiments, the temperature was kept within ± 1°C from 23°C.

It is important to extend these studies to a range of temperatures up to the martensitic transition temperature, about 32°C. On the one hand, pulsed-field experiments would be able to provide the maximum rate of extension as a function of the peak field. Data analogous to that of Fig. 4-10 would be available for the different temperatures, and the validity of Eq. (C.55) could be confirmed through the inverse relation between temperature and the constants C_1 and C_2 in Eq. (4.20).

On the other hand, the impact of the temperature on the performance of Ni–Mn–Ga could be assessed vis-à-vis efforts underway to raise the martensitic transition temperature. The data could also be used to determine performance margins, and

determine the usefulness of Ni–Mn–Ga as a low temperature actuator material.

5.2.8 Alloy design

As is apparent from Eq. (1.10) and from other efforts on modelling the driving force for field-induced twin-boundary motion in cases where external stresses and other contributions to the total energy are present [60, 77], the maximum magnetic energy that can be coupled to the mechanical actuation is given by the magnetocrystalline anisotropy. It was speculated that distortions of the austenite lattice greater than the one observed during the martensitic transformation of Ni–Mn–Ga of the present composition could lead to larger values of the anisotropy. The assumption that these distortions could be augmented via the substitution of different atomic species for Ga led to the substitution of In for Ga in $Ni_{49}Mn_{29}Ga_{22-x}In_x$ [78]. These alloys did not show improvement in any of the key properties of a ferromagnetic shape memory alloy with respect to Ni–Mn–Ga. However, it is still interesting to improve the performance of Ni–Mn–Ga in this fashion.

The design of ferromagnetic shape memory alloys is a field of its own, and shows promise in the longer term. Some guidelines are available (for example [79].) Research in the field is greatly aided by the ability to produce large[8] batches of alloys to ease obtaining good homogeneity[9].

5.2.9 Devices

Switches

The results from this work suggest a new concept for the operation of Ni–Mn–Ga-based actuators. The air-core Helmholtz coils could be used to produce compact and fast mechanical switches, with strains of 6% developed in 200 μs and less. The addition of reset coils, that is, coils oriented at 90° from the main coil could allow

[8] Several hundred gram.

[9] It would appear that suction casting techniques are inadequate. Samples so obtained tended to be exceedingly brittle because of a radial grain structure. Homogenization treatments often resulted in unacceptable composition deviations.

the magnetic (at least equally fast) switching time. It is important that the reset coil be able to produce fields of sufficient intensity. Prototypes that did not exceed 4 kOe field-intensities failed to produce a measurable resetting, and must be revised.

Stepper motor

By the same principle, a stepper actuator could be constructed, based on magnetic field pulses, as opposed to a continuous actuator based on on an AC field. The main advantage of this design would be the replacement of the heavy magnet cores with compact, air-core Helmholtz coils.

Appendix A

Additional Material

A.1 Coil used in the experiments

A.1.1 Expressions for the inductance

The inductance can be obtained from the expression for the inductance L_s of each identical sub-coil s and the mutual inductance M_{ss} as:

$$L = 2L_s + 2M_{ss} \tag{A.1}$$

L_s can be written in terms of the self-inductance of a loop carrying a uniform current L_u and a correction ΔL_u, as $L_s = L_u + \Delta L_u$. The latter accounts for the fact that rather than a single loop, each sub-coil consists of n discrete loops spanning a cross section of $b_1 \times b_2 \equiv b^2$. It is:

$$\begin{aligned} L_u &= \frac{4an^2\pi}{c^2}\left(1 - y_1 + \frac{b^2 y_2}{16a^2} + \frac{b^2 \log(\frac{4\sqrt{2}a}{b})}{24a^2}\right) \\ \Delta L_u &= \frac{4an\pi}{c^2}\left(0.13806 + \log(\frac{\Phi}{\phi})\right) \end{aligned} \tag{A.2}$$

where it was assumed that the cross section of the sub-coils is a square of side b, Φ is the diameter of the wires with insulation, ϕ the diameter without insulation, and y_1

and $y2$ have the numeric values:

$$\begin{aligned} y_1 &= 0.84834 \\ y_2 &= 0.8162 \end{aligned} \tag{A.3}$$

The mutual inductance is $M_{ss} = M_1 + n^2 \Delta M_1$. Here M_1 is the mutual inductance of two loops and ΔM_1 corrects for the geometry of the sub-coil's n loops, in the same fashion as ΔL_u.

$$\begin{aligned} M_1 &= \frac{4a\pi}{c^2}\left(-\sqrt{5}E + \left(\frac{-2}{\sqrt{5}} + \sqrt{5}\right)K\right) \\ \Delta M_1 &= \frac{8a\pi}{\sqrt{5}\,c^2}\left(\frac{131}{22500}\frac{b^4}{a^4}E + \left(\frac{1}{24}\frac{b^2}{a^2} + \frac{131}{90000}\frac{b^4}{a^4}\right)(K-E)\right) \end{aligned} \tag{A.4}$$

where for convenience E and K have been written for the complete elliptical integrals of $2/\sqrt{5}$ of first and second kind respectively. In practice the corrections ΔL_u and ΔM_1 are neglected, and

$$L = 2L_u + 2M_1 \tag{A.5}$$

is used directly.

A.1.2 Coil drawings

Figure A-1 indicates the exact dimensions of one of the coils used in the present work, which produced the field-pulses described in chapter 3.

A.1.3 DAC-voltage reference

The signal output from the photo-detector (photodiode or photomultiplier) was mounted on a DC offset. In order to make use of the full amplification range available from the preamplifier[1], the offset must be subtracted. It is desirable to set the voltage that is to be subtracted from within the optics calibration program. The control of all

[1]See footnote 10 on page 50.

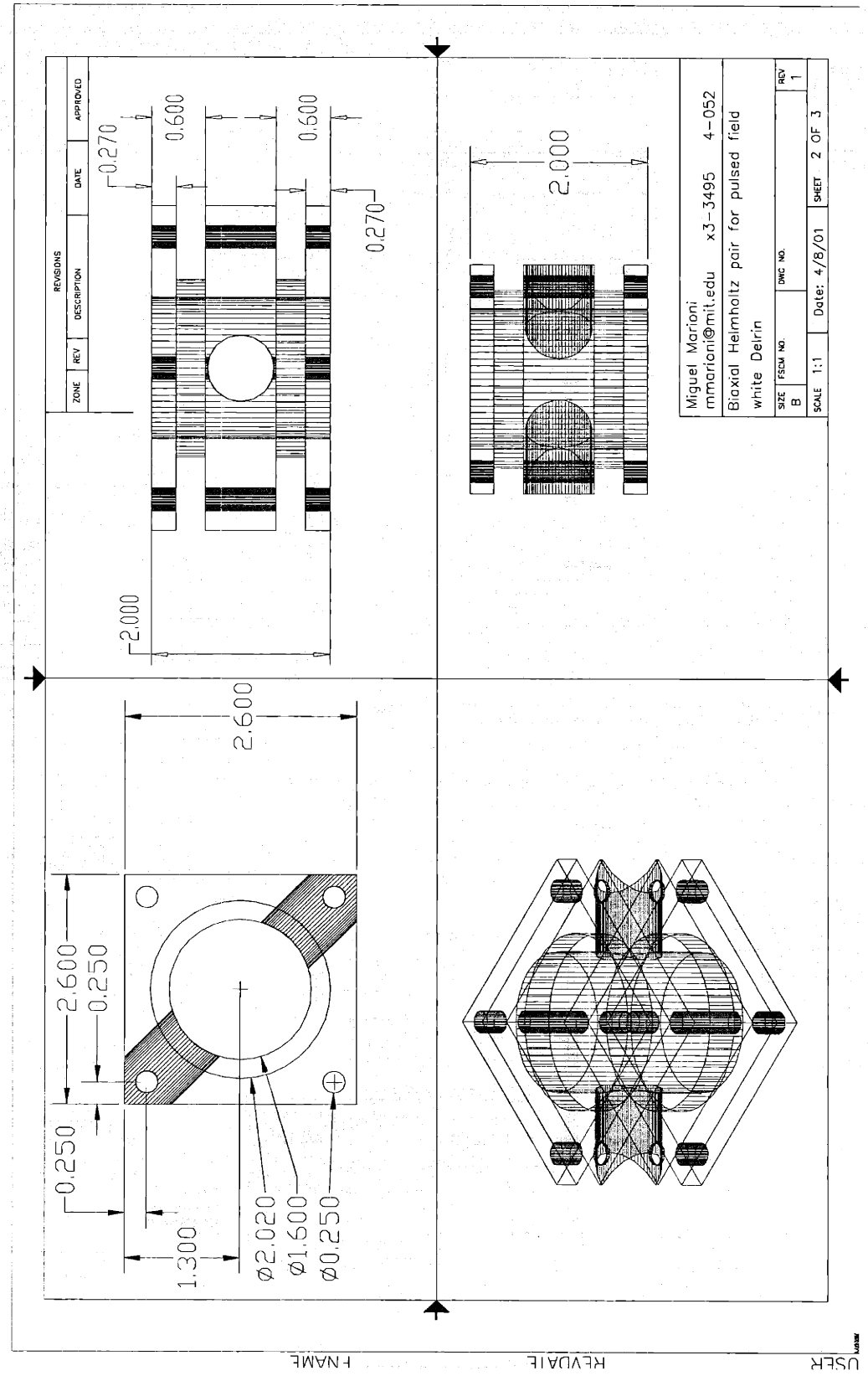

Figure A-1: Drawings of the coil used in chapter 3. The slots are filled with 25 windings of AWG #15- gage insulated copper wire. Dimensions in inches.

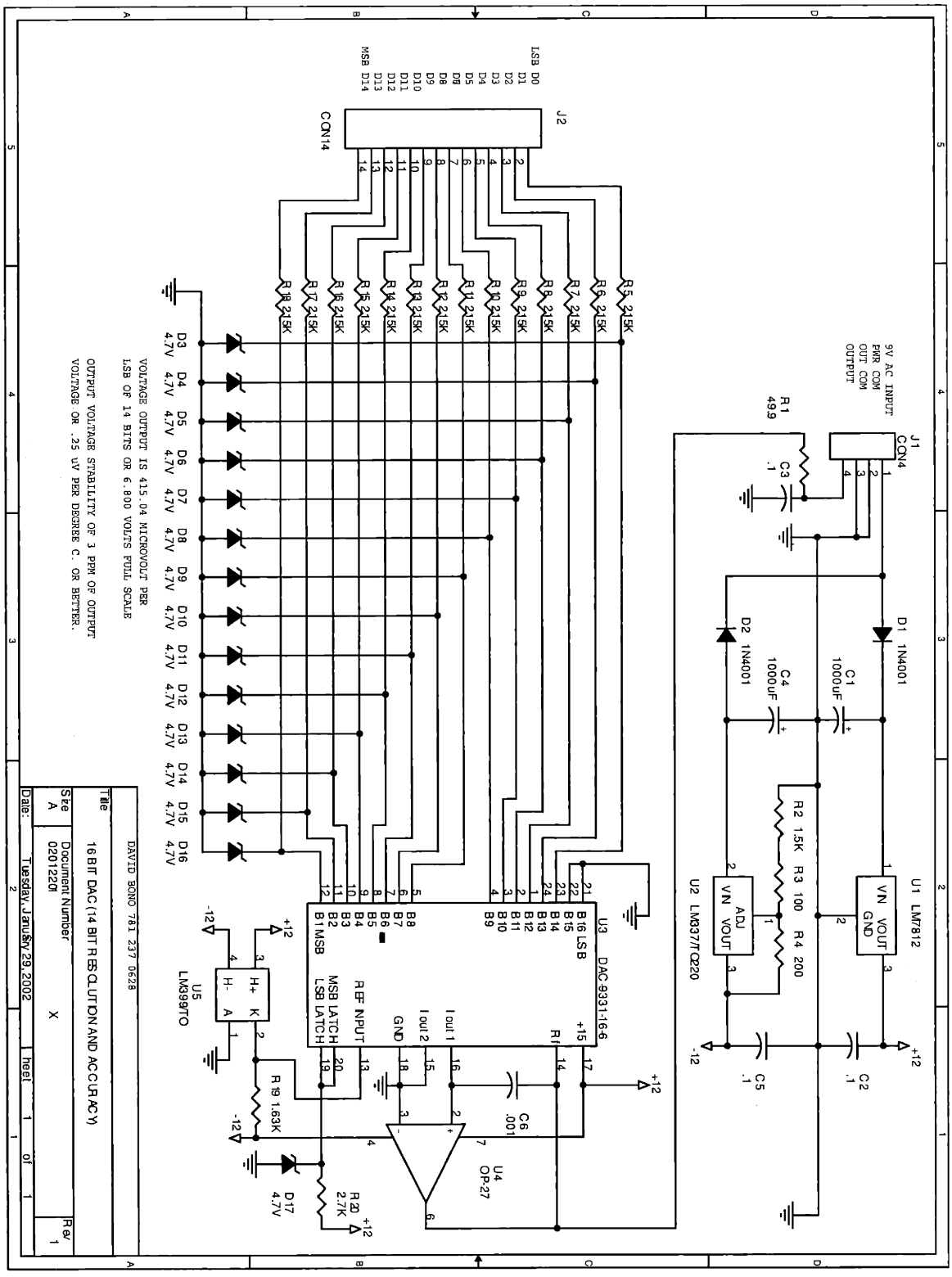

Figure A-2: DAC-voltage reference used to subtract the offset from the photomultiplier signal (design: courtesy of D. C. Bono.) This circuit has low noise and low drift, and accuracy equivalent to 18 bits. The least significant bit corresponds to a voltage of $3\,\mu$V.

the elements in the system is done via individual modules[2] connected to the RS232 interface of the computer, but it is not possible to use the output of these devices directly. Not only is the resolution limited to 10 mV, but more importantly, the noise coupled to the optic measurement though the RS232 would increase the noise level by several orders of magnitude. A low-noise, low-drift voltage reference is necessary. The custom made DAC-voltage reference of Fig. A-2 is used. It has excellent stability and 12 bit resolution, with the least significant bit corresponding to 3 μV.

[2]Weeder Technologies WTDAC-M. See also footnote 20 on page 53.

Appendix B

Time-dependent magnetic field in a conductor

B.1 About a pulsed magnetic field inside a conductor

B.1.1 Waves in dielectric and conductive media

Assuming that the materials are (locally) homogeneous, linear, and in the absence of free charges and free currents, Maxwell's equations take on the form:

$$\nabla \cdot \mathbf{E} = 0 \tag{B.1}$$

$$\nabla \cdot \mathbf{H} = 0 \tag{B.2}$$

$$\nabla \times \mathbf{E} = -\frac{\mu}{c}\frac{\partial \mathbf{H}}{\partial t} \tag{B.3}$$

$$\nabla \times \mathbf{H} = \frac{4\pi}{c}\sigma \mathbf{E} + \frac{1}{c}\frac{\partial \mathbf{E}}{\partial t} \tag{B.4}$$

$\nabla\times$ is applied to Eq. (B.3) and Eq. (B.4). Using Eq. (B.1) and Eq. (B.2) and the identity

$$\nabla \times (\nabla \times \mathbf{F}) = \nabla(\nabla \cdot \mathbf{F}) - \nabla^2 F \tag{B.5}$$

one obtains

$$\nabla^2\mathbf{E} - \frac{4\pi\sigma\mu}{c}\frac{\partial\mathbf{E}}{\partial t} - \frac{\epsilon\mu}{c^2}\frac{\partial^2\mathbf{E}}{\partial t^2} = 0 \tag{B.6}$$

$$\nabla^2\mathbf{H} - \frac{4\pi\sigma\mu}{c}\frac{\partial\mathbf{H}}{\partial t} - \frac{\epsilon\mu}{c^2}\frac{\partial^2\mathbf{H}}{\partial t^2} = 0 \tag{B.7}$$

which are the well-known homogeneous wave equations for the **E** and **H** fields in conductive media. This equation is satisfied for various (including constant) fields [80], but only plane transverse elector-magnetic wave solutions will be considered, i.e.:

$$\mathbf{F} = \mathrm{Re}\left(\mathbf{F_0}e^{i\mathbf{k}\cdot\mathbf{x}-i\omega t}\right) \tag{B.8}$$

where $\mathbf{F_0}$ is the amplitude of a field, ω is the angular frequency of the wave, and $\mathbf{k} = \mathbf{k}(\omega)$ is the wave vector, $|\mathbf{k}| = 2\pi/\lambda$.

Placing the above Eq. (B.8) (where **F** can be either the electric or magnetic field) into the appropriate wave equation (B.6) or (B.7), the *dispersion relation* is obtained

$$\|\mathbf{k}\|^2 \equiv k^2 = \frac{\mu\epsilon\omega^2}{c^2}\left(1 + i\frac{4\pi\sigma}{\omega\epsilon}\right) \tag{B.9}$$

k can be written as

$$k = \beta(\omega) + i\,\alpha(\omega) \tag{B.10}$$

where α and β are given by:

$$\left.\begin{matrix}\beta(\omega)\\ \alpha(\omega)\end{matrix}\right\} = \sqrt{\mu\epsilon}\,\frac{\omega}{c}\left[\frac{\sqrt{1+\left(\frac{4\pi\sigma}{\omega\epsilon}\right)^2}\pm 1}{2}\right]^{1/2} \tag{B.11}$$

In the case where the problem is 1D, the wave equation takes on the form:

$$\frac{\partial^2 F}{\partial x^2} - \frac{4\pi\sigma\mu}{c}\frac{\partial F}{\partial t} - \frac{\epsilon\mu}{c^2}\frac{\partial^2 F}{\partial t^2} = 0 \tag{B.12}$$

for propagation along the x-axis, which has solutions of the form

$$F = \mathrm{Re}\left(F_{0+}\, e^{i\,kx - i\omega t}\right) + \mathrm{Re}\left(F_{0-}\, e^{-i\,kx - i\omega t}\right) \tag{B.13}$$

Here the subscripts + and − indicate the direction of propagation of the wave solution, toward positive or negative x respectively. The constants F_{0+} and F_{0-} are determined with the initial conditions.

B.1.2 Field in a semi-infinite conductive medium

Consider the problem of figure B-1.

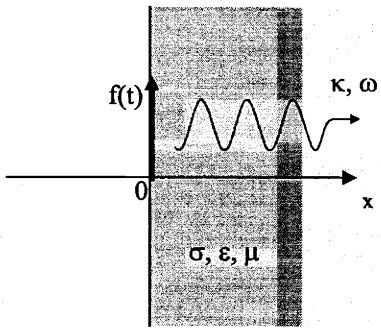

Figure B-1: Schematic of a wave with wave vector k and frequency ω propagating in a semi-infinite medium of conductivity σ, dielectric constant ϵ and permeability μ.

The statement of the problem must include specification of the boundary and initial conditions. To simplify the discussion, the field will be written as $H_2(x,t)$ in $x > 0$ and as $H_1(x,t) + H_3(x,t)$ in $x < 0$. The intention behind this choice is to identify $H_1(x,t)$ as a pulse incident on the $x = 0$-interface coming from $x = -\infty$, and $H_2(x,t)$ and $H_3(x,t)$ as a transmitted and a reflected pulse respectively. Note that waves travelling toward $x = 0$ from $x = +\infty$ would need to have infinite amplitude to reach the origin and not vanish. This is because in that semi-space the medium is conductive and fields attenuate exponentially with a characteristic length δ,

$$\delta(\omega) = \alpha(\omega)^{-1} \simeq \frac{c}{\sqrt{2\pi\,\sigma\,\mu\,\omega}} \tag{B.14}$$

Further, if the medium in $x < 0$ is non-dispersive, plane waves for all frequency

components travel at the speed of light, $c(\mu_1\epsilon_1)^{-1/2}$, and a pulse retains its shape. This allows us to identify H_1 and H_3, as

$$H_1(x,t) = \mathrm{Re}\left(\int_0^{+\infty} H_1^0(\omega)e^{ik_1(\omega)x-i\omega t}d\omega\right) \tag{B.15}$$

$$H_3(x,t) = \mathrm{Re}\left(\int_0^{+\infty} H_3^0(\omega)e^{-ik_3(\omega)x-i\omega t}d\omega\right) \tag{B.16}$$

with

$$k_1(\omega) = k_3(\omega) = \sqrt{\mu_1\epsilon_1}\,\frac{\omega}{c} \tag{B.17}$$

and

$$H_2(x,t) = \mathrm{Re}\left(\int_0^{+\infty} H_2^0(\omega)e^{ik_2(\omega)x-i\omega t}d\omega\right) \tag{B.18}$$

with

$$\begin{aligned} k_2(\omega) &= \beta(\omega) + i\alpha(\omega) = \\ &= \sqrt{\mu\epsilon}\,\frac{\omega}{c}\left\{\left[\frac{\sqrt{1+\left(\frac{4\pi\sigma}{\omega\epsilon}\right)^2}+1}{2}\right]^{1/2} + i\left[\frac{\sqrt{1+\left(\frac{4\pi\sigma}{\omega\epsilon}\right)^2}-1}{2}\right]^{1/2}\right\} \end{aligned} \tag{B.19}$$

$H_1^0(\omega)$, $H_2^0(\omega)$ and $H_3^0(\omega)$ have to be chosen according to the initial and boundary conditions. With the identity

$$\mathrm{Re}\left(F_0(\omega)e^{ik(\omega)x-i\omega t}\right) = \frac{1}{2}\left(F_0(\omega)e^{ik(\omega)x-i\omega t} + F_0^*(\omega)e^{-ik^*(\omega)x+i\omega t}\right) \tag{B.20}$$

it is found:

$$H_j(x,t)_{j=1,2,3} = \frac{1}{2}\left(\underbrace{\int_0^{+\infty} H_j^0(\omega)e^{ik_j(\omega)x-i\omega t}d\omega}_{I_+} + \underbrace{\int_0^{+\infty} H_j^{0*}(\omega)e^{-ik_j^*(\omega)x+i\omega t}d\omega}_{I_-}\right) \tag{B.21}$$

Changing variables in expression I_- above to $u = -\omega$:

$$I_- = \int_{-\infty}^{0} H_j^{0*}(-u)e^{-ik_j^*(-u)x-iut}du \tag{B.22}$$

Notice that in the above expressions $H_j^0(\omega)$ as well as $k_j(\omega)$ are defined only on $\omega \in (0, +\infty)$, since physical sense is ascribed to positive frequencies. Mathematically, these definitions can be extended by constructing new functions $\tilde{H}_j^0(\omega)$ and $\tilde{k}_j(\omega)$ in the following manner:

$$\tilde{H}_j^0(\omega) \equiv \begin{cases} H_j^0(\omega) & \text{if } \omega > 0 \\ H_j^{0*}(-\omega) & \text{if } \omega < 0 \end{cases} \tag{B.23}$$

$$\tilde{k}_j(\omega) \equiv \begin{cases} k_j(\omega) & \text{if } \omega > 0 \\ -k_j^*(-\omega) & \text{if } \omega < 0 \end{cases} \tag{B.24}$$

With these definitions, Eq. (B.22) is rewritten as

$$I_2 = \int_{-\infty}^{0} \tilde{H}_j^0(u) e^{i\tilde{k}_j(u)x - iut} du \tag{B.25}$$

and the expression for the pulse becomes

$$H_j(x,t)_{j=1,2,3} = \frac{1}{2}\left(\int_{-\infty}^{+\infty} \tilde{H}_j^0(\omega) e^{i\tilde{k}_j(\omega)x - i\omega t} d\omega\right) \tag{B.26}$$

Note that $\tilde{k}_j(\omega)$ has to be used, not $k_j(\omega)$.

It can easily be seen that $\tilde{H}_j^0(\omega)$ is proportional to the Fourier transform $\hat{H}_j^0(\omega)$ of the real function $H_j(x,t)$:

$$\tilde{H}_j^0(\omega) = \sqrt{\frac{2}{\pi}} \hat{H}_j^0(\omega) = \frac{1}{\pi} \int_{-\infty}^{+\infty} H_j(x,t)\, e^{i\tilde{k}_j(\omega)x - i\omega t} d\omega \tag{B.27}$$

Notice that the restriction $\tilde{H}_j^0(-\omega) = \tilde{H}_j^{0*}(\omega)$ is satisfied by the Fourier transform because $H(x,t) \in \Re$.

Finally, since per definition (Eq. (B.24)) $\tilde{H}_j^0(\omega)|_{\omega>0} \equiv H_j^0(\omega)$, and dropping the tilde in $\tilde{k}$ because the expression does not depart from the definition of k for $\omega > 0$ it is obtained:

$$H_j(x,t)_{j=1,2,3} = \sqrt{\frac{2}{\pi}} \mathrm{Re}\left(\int_0^{+\infty} \hat{H}_j^0(\omega) e^{ik_j(\omega)x - i\omega t} d\omega\right) \tag{B.28}$$

This is the result sought.

B.2 Application: pulsed field experiment

It is necessary to discuss the conditions under which the results of the previous section are applicable. Maxwell's equations are linear, and consequently the linear combination of functions that satisfy them individually will also satisfy them. This makes the direct application of Eq. (B.28) difficult on two accounts: Firstly, in ferromagnetic shape memory alloys the relation between H and B is not linear, so superposition is not valid. Secondly, the boundary conditions must also be linear if the superposition is to be a solution to the problem. This is not the case when there are moving twin-boundaries.

Inherent to the considerations of this section is the assumption that the conducting material occupies a semi-infinite volume. Since the typical skin depth in the present case is of the order of the sample dimensions, any results derived from Eq. (B.28) will only provide a lower bound for the field.

Consider a material with the electrical properties of Ni–Mn–Ga, but where twin-boundary motion is precluded. Let the material have a single martensite variant, with the easy axis in the $\hat{z}$ direction. A field applied along $\hat{z}$ will not apply a torque on the magnetization because both are colinear. Therefore $\partial M/\partial B = 0$ in this case and the system responds to the field as vacuum would do, that is with susceptibility $\chi = 0$. It means that the aforementioned superposition technique can be employed in this case.

Likewise, there are configurations that give rise to constant (albeit not zero) susceptibility for weak enough fields, and in these cases the superposition method could be used as well. [1] For example, when a single variant has the easy axis pointing in $\hat{x}$ direction, and the direction $\hat{z}$ corresponds to a possible easy axis for a different variant, then the projection of the magnetization along $\hat{z}$ is proportional to the field

[1] Clearly, for intense enough fields the magnetization is oriented along the field direction and then $\chi = 0$ as well, but there will always be a transient during which the magnetization is reorienting itself.

along that direction. This implies that the effective susceptibility would be constant, resulting in linear wave equations, that admit the solution of Eq. (B.28). In the real case twin-boundary motion is likely to ensue in this condition. When this occurs the susceptibility could diverge as the easy axis of a material volume element changes abruptly.

As indicated in Sec. B.1.2 above, a pulse $H_1(x,t)$ corresponding to a field in the $\hat{z}$ direction will be considered. It impinges on the $x = 0$ plane coming from $x = -\infty$. The pulse refracts, and the transmitted pulse has amplitude $H_2(x,t)$ in the domain $x \geq 0$. As well, there will be a reflected part, which will be labeled $H_3(x,t)$ and exists in the domain $x < 0$.

The field in $x < 0$ and in $x \geq 0$ is a superposition of simple plane waves (the propagators), i.e.:

$$\begin{aligned} H(x<0,t) &= L.C.\left\{e^{ik_1(\omega,\mu_1,\epsilon_1)x-i\omega t}\right\} \\ H(x\geq 0,t) &= L.C.\left\{e^{ik_2(\omega,\mu_2,\epsilon_2,\sigma)x-i\omega t}\right\} + L.C.\left\{e^{-ik_1(\omega,\mu_1,\epsilon_1)x-i\omega t}\right\} \end{aligned} \quad \text{(B.29)}$$

where:

$$\begin{aligned} k_1 &= \sqrt{\mu_1\epsilon_1}\,\frac{\omega}{c} \\ k_2 &= \sqrt{\epsilon_2\,\mu_2}\,\frac{\omega}{c}\left(\sqrt{\frac{\sqrt{1+s^2}+1}{2}} + i\,\mathrm{sign}(\omega)\sqrt{\frac{\sqrt{1+s^2}-1}{2}}\right) \\ s &= \frac{4\pi\,\sigma}{\epsilon_2\,\omega} \end{aligned} \quad \text{(B.30)}$$

and $L.C.$ stands for "linear combination."

The coefficients for the linear combination in Eq. (B.35) are obtained via Eq. (B.28) from the spectral decomposition $A(\omega)$ of the temporal profile of the field at $x = -\infty$ and appropriate reflection and transmission coefficients, R and T. For simplicity, instead of taking a numerical version of $A(\omega)$ directly from the measured field data,

the experimental pulse[2] profile is first fit with an amplitude function $A(t)$ of the form

$$A(t) = \begin{cases} h\sin(\pi t/b)e^{-at} & \text{if} \quad 0 \le t \le \tau \\ 0 & \text{if} \quad \tau \le t \end{cases} \tag{B.31}$$

and then this $A(t)$ IS decompose. For definiteness, the field from a 2 kV pulse is used. The parameters h and b are close to the peak field the pulse duration respectively. The transform $A(\omega)$ of $A(t)$ is readily computed as:

$$A(\omega) = \frac{b\,e^{-\left(\frac{a\,\pi}{b}\right)-\frac{i\,x\left(-1+\sqrt{\epsilon_1\,\mu_1}\right)\omega}{c}}\left(e^{\frac{a\,\pi}{b}}+e^{\frac{i\,\pi\,\omega}{b}}\right)h}{\sqrt{2\,\pi}\left(b^2+(a-i\,\omega)^2\right)} \tag{B.32}$$

The reflection and transmission coefficients for the amplitude are:

$$\begin{aligned} R(\omega) &= \frac{1-\frac{\mu_2}{\mu_1}\frac{k_1}{k_2}}{1+\frac{\mu_2}{\mu_1}\frac{k_1}{k_2}} \\ T(\omega) &= \frac{2}{1+\frac{\mu_2}{\mu_1}\frac{k_1}{k_2}} \end{aligned} \tag{B.33}$$

For the 2 kV pulse of Fig. B-2 the parameters h, b and a are:

$$\begin{aligned} h &= 20.7\,\text{kOe} \\ b &= 609\,\mu\text{s} \\ a &= 601\,\text{s} \end{aligned} \tag{B.34}$$

The final step is the integration[3]

$$H(x<0,t) = \frac{1}{2}\sqrt{\frac{2}{\pi}}\int_0^\infty A(\omega)\left(e^{ik_1x-i\omega t} + R(\omega)\,e^{-ik_1x-i\omega t}\right)d\omega$$

[2]The pulse does not start exactly at $t = 0$ (there is a 10 μs delay.) Therefore the data is shifted in time so that the pulse-onset is at t=0.

[3]By necessity the integral is done numerically. The upper integration limit was replaced by $40\pi/\tau$.

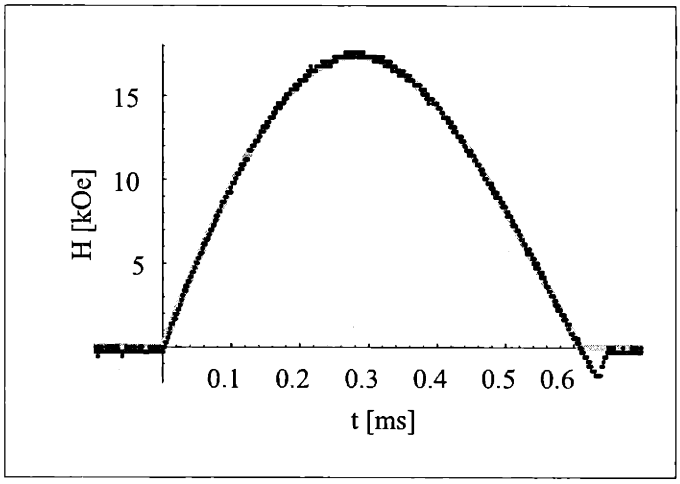

Figure B-2: Field profile for a 2 kV pulse (dots) and fit with Eq. (B.31) (gray.)

$$H(x \geq 0, t) \;=\; \frac{1}{2}\sqrt{\frac{2}{\pi}} \int_0^\infty A(\omega)\, T(\omega)\; e^{ik_2 x - i\omega t} d\omega \tag{B.35}$$

Fig. B-3 shows the field inside the material computed as per Eq. (B.35). It is interesting to note that the field lingers inside the material for times as long as twice the pulse duration. As well a delay is apparent.

B.3 Corrections to the measured field

Once it is determined that the field inside the sample can differ from the applied field a correction to the results obtained in Chapter 3 needs to be developed. The simplest possible approach to the problem is to take an average over some representative length of the sample. In the present work, the average over *half* the sample width, ie. 2.5 mm is taken, that is:

$$\langle H \rangle(t) = \int_0^{2.5\,\mathrm{mm}} H(x,t) dx \tag{B.36}$$

where $H(x,t)$ is given by Eq. (B.35) and calculated for a 2 kV field $H_{2\,\mathrm{kV}}$.

The correction for a pulse of given peak field H^{peak} will be:

$$\Delta H(t) = H(t) + \frac{H^{peak}}{H^{peak}_{2\,\mathrm{kV}}} \left(\langle H \rangle(t) - H_{2\,\mathrm{kV}}(t) \right) \tag{B.37}$$

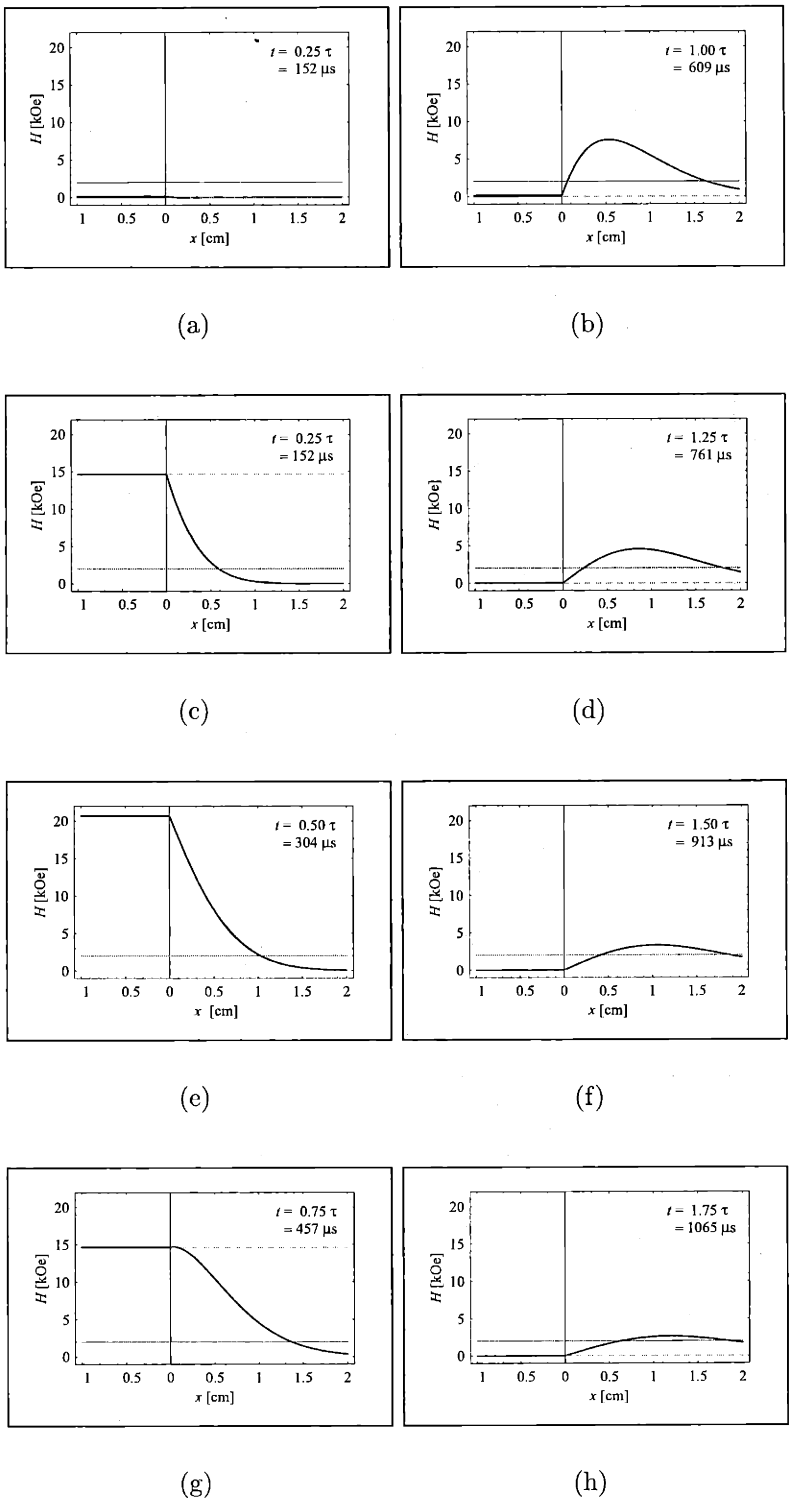

Figure B-3: Field profile for various times, simulated from a 2 kV pulse. The region $x < 0$ corresponds to free space, and the region in $x \geq 0$ corresponds to a linear conductor. The solid grayline indicates the threshold field.

Fig. B-4 shows the averaged field and driving force. It is apparent that the field and driving force so described lag the values outside the material.

B.3.1 Application to pulses of varying intensity

Solutions that are linear superposition of plane waves possess an advantage in that in the experiments of this thesis the field profile scales with the peak field. This means that the evolution inside the Ni–Mn–Ga will be the same as that of a reference pulse multiplied by the ratio of peak fields. The solution found in the previous section can be scaled to represent the solution to the field of other pulses.

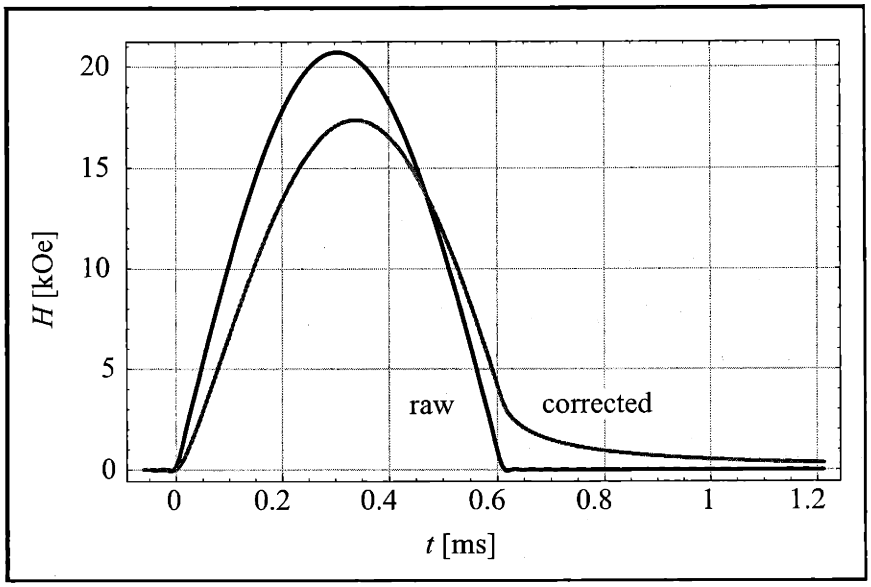

(a)

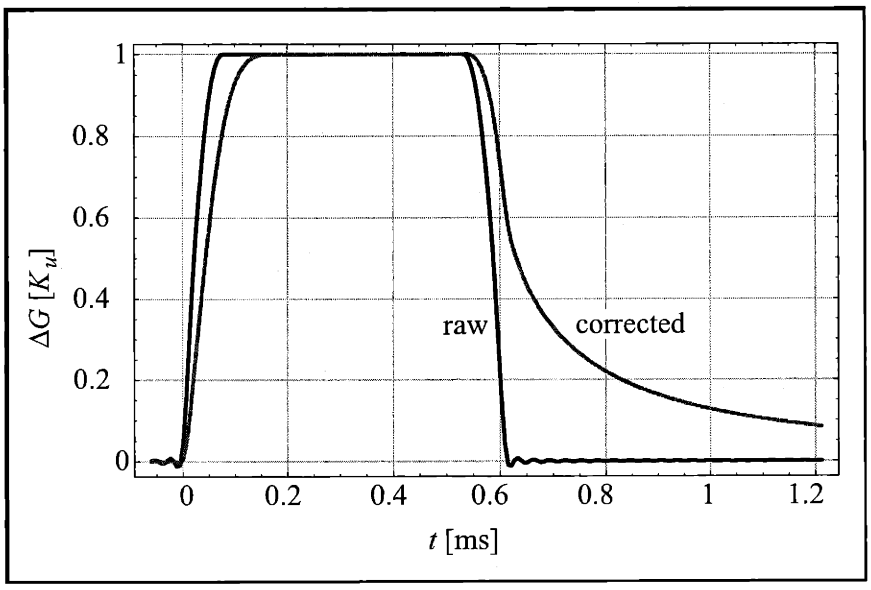

(b)

Figure B-4: (a) Plots of the field and (b) driving force vs. time. In black a fit to the measured field and defdG for a 2 kV pulse respectively is plotted. In gray the average over half the width of the samples used in the experiments of Chapter 3 is shown.

Appendix C

Time dependent processes affecting twin-boundary motion

In this appendix the influence of time dependent processes on twin-boundary motion is considered. The processes here considered include nucleation of partial dislocations and the de-pinning of partial dislocations.

Section C.1 discusses the kinetics of partial dislocation nucleation, mainly focusing on the nucleation rates. The latter could be a rate-limiting process in the motion of twin-boundaries, a possibility that is discussed in Sec. C.2. In Sec. C.3 it is assumed that the rate-limiting process for twin-boundary motion is the pinning and de-pinning of the twin-boundary and expressions are obtained for the twin-boundary velocity.

The results of Sec. C.2 and Sec. C.3 can be viewed as extreme cases. The intermediate case of concurrent nucleation and expansion of partial dislocations is addressed in Sec. C.4.

C.1 Nucleation of twin-boundaries

Consider the generation of partial dislocation loops in a variant 2 of a single crystal of Ni–Mn–Ga. The twinning process that transforms variant 2 into variant 1 causes a certain number of atoms to change their positions, and attain new ones that have the same lattice orientation as variant 1. In the region bound by the loop, atoms

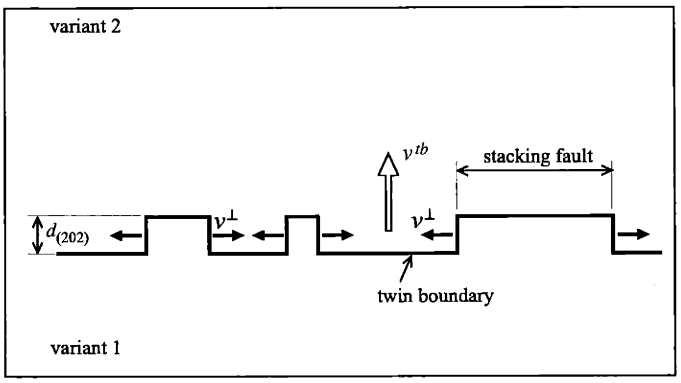

Figure C-1: Schematic of the twin-boundary motion process and definition of the twin-boundary- and partial dislocation velocities.

are displaced a distance $b = [\bar{1}01]\epsilon_o$ in the $\hat{t} \equiv [\bar{1}01]$ direction from their original equilibrium positions: they constitute a stacking fault from the perspective of variant 2. This stacking fault can be regarded as a mono-layer twin.

Twin boundaries advance when $[\bar{1}01]$ partial dislocations are created on the (202) twin plane and expand on it, eventually sweeping out its area. The process is depicted in Fig. C-1.

It is important to determine the rates at which the partial dislocations are created. Depending on the kinetics of this process, a Ni–Mn–Ga crystal's rate of extension could be not only a function of the driving force but explicitly of time. In this section the theory of nucleation is used to find the rates at which heterophase fluctuations can give rise to stable partial dislocation loops. It will be considered that a partial dislocation loop will stabilize if it exceeds a critical radius, later to be determined, in what constitutes a nucleation event.

C.1.1 Calculation of the critical quantities

In essence, the nucleation process affects the free energy of the system in three ways. There is a lowering of the system's free energy through the formation of a region of the variant that has a magnetic easy axis better aligned with the field. Therefore the driving force for twin-boundary motion ΔG for twin-boundary motion promotes the nucleation and expansion of partial dislocation loops. Concurrently, the line tension

of the created partial dislocation means that work is required to expand it to a given size. It opposes the partial dislocation nucleation. Further, creation of a partial dislocation loop involves the formation of a faulted region in the crystal, so there will be a contribution to the total free energy coming from the fault energy γ. It is a positive quantity, because work is required to move the atoms out of their equilibrium stacking in the lattice. Therefore both the line tension and the fault energy constitute a barrier to the formation of a (partial) dislocation loop in the single-variant bulk, i.e. the homogeneous nucleation of partial dislocations. When the stacking fault forms on an existing twin-boundary, that is, if in so doing it extends the region of variant 1 at the expense of variant 2 on an existing twin-boundary, no increase in surface energy is incurred.

As the radius of a partial dislocation increases from zero, an increase of the total energy is observed, because initially the contributions from the surface and line-tension energies dominate. When the volume contributions (in this case associated with a decrease of ΔG of magnetic origin) begin to dominate, a peak in the energy is reached. The radius at which this occurs is termed *critical radius*. Beyond it the system's free energy lowers. Partial dislocation loops with radii smaller than r_c are called embryos. A nucleation event consists in the addition of one atom to an embryo of critical radius — further additions (or increase in loop radius) lower the system's free energy. Within the framework of the Volmer-Weber [81] nucleation theory, which will be employed here, nuclei will not transform back to the embryonic state[1].

The effective rate of extension will be determined by the net rate of partial dislocation formation. The motion of partial dislocations beyond the nucleation stage does not concern the considerations of this section.

Throughout this development the quasi-steady state nucleation model will be used, and a steady nucleation rate is therefore implied. This is generally not an accurate representation of the problem in the case when the driving force is quickly varied, since in this case the system will be far from equilibrium. Nevertheless, a lower bound

[1]This approximation is lifted in the Becker-Döringer theory [82], but this refinement does not augment the insight of the problem.

for the time-dependent nucleation rate [83] can be obtained with this approach.

Magnetic driving force

For simplicity it is assumed that there are two twin variants, 1 and 2. Variant 1 has its magnetic easy axis aligned with the field. The field causes variant 1 to grow at the expense of variant 2. The specific free energy change of this process will be:

$$\Delta G^{2\to 1} = \begin{cases} -K_u(2\eta + \eta^2) & \text{if } 0 \le \eta \le 1 \\ -1 & \text{otherwise} \end{cases} \tag{C.1}$$

where K_u is the magnetocrystalline anisotropy and η is the reduced magnetic field, $\eta = M_s H/(2K_u)$. The formation of a loop of radius r will therefore cause the total free energy to drop by $\pi r^2 d_{(202)} \Delta G^{2\to 1}$, where $d_{(202)}$ is the distance between contiguous (202)-planes[2].

Line tension

Let us consider first the line tension of the dislocation loop and the corresponding self energy. Following Hirth and Lothe [84] it is obtained from the formula by Blin [85] for the interaction energy of two arbitrary dislocation loops,

$$\begin{aligned} W_{12} \;=\; & -\frac{\mu}{2\pi}\oint_{\mathcal{C}_1}\oint_{\mathcal{C}_2}\frac{(b_1\times b_2)\cdot(dl_1\times dl_2)}{r} + \frac{\mu}{4\pi}\oint_{\mathcal{C}_1}\oint_{\mathcal{C}_2}\frac{(b_1\cdot dl_1)\cdot(b_2\cdot dl_2)}{r} + \\ & + \frac{\mu}{2\pi(1-\nu))}\oint_{\mathcal{C}_1}\oint_{\mathcal{C}_2}(b_1\times dl_1)\cdot T\cdot(b_2\times dl_2) \end{aligned} \tag{C.2}$$

In this equation, b_1 and b_2 are the Burgers vectors of dislocation loops $\mathcal{C}_1$ and $\mathcal{C}_2$, dl_1 and dl_2 are the curve elements thereof, and R is the distance between them. μ is the shear modulus, and ν is Poisson's modulus. The tensor T is defined by its components, $T_{ij} = \partial^2 r/\partial x_i \partial x_j$.

[2]See Fig. 1-1. Using the $Fm\bar{3}m$ lattice notation facilitates the comparison with structures other than the tetragonal $I4/mmm$-symmetric structure proper of the Ni–Mn–Ga compositions used in this work. Of course, in the $Fm\bar{3}m$ lattice (202) is not a twin plane. From inspection it is seen that in austenite ($Fm\bar{3}m$) the (202) is a plane of mirror symmetry.

In order to get the self-energy of the dislocation loop, b is replaced for b_1 and b_2, as well as $\mathcal{C}$ for $\mathcal{C}_1$ and $\mathcal{C}_2$, and the result divided by 2. For a circular loop, this exercise leads to

$$\begin{aligned} W_s &= -\frac{\mu b^2}{8\pi}\oint_{\mathcal{C}} \sin\phi_0 dl_0 \int_{l_0+\rho}^{l_0+2\pi r-\rho} \frac{\sin\phi}{r'} dl + \\ &+ \frac{\mu b^2}{8\pi(1-\nu))}\oint_{\mathcal{C}} \cos\phi_0 dl_0 \int_{l_0+\rho}^{l_0+2\pi r-\rho} \frac{\cos\phi}{r'} dl \end{aligned} \tag{C.3}$$

where r is the vector going from the loop center to the loop element dl, ϕ is the polar angle of r, dl_0 is another curve element corresponding to angle ϕ_0, and r' is the separation between dl and dl_0. ρ is the a cut-off distance, below which two dislocation line elements do not interact. [3] With the substitutions:

$$r' = 2r\sin\frac{\phi-\phi_0}{2} \qquad dl = rd\phi \qquad dl_0 = rd\phi_0 \quad , \tag{C.4}$$

one obtains

$$W_s = 2\pi r \frac{2-\nu}{2(1-\nu)}\frac{\mu b^2}{4\pi}\left(-\ln\left(\tan\frac{\rho}{4r}\right) - 2\cos\frac{\rho}{2r}\right) \tag{C.5}$$

Note that this expression for W_s becomes negative for $r < r_{lim} \simeq 2.57557\rho$. This is because the approximation of an elastic material breaks down. Consistently, for $r < r_{lim}$ $W_s = 0$ is taken. From a comparison of the energy of two infinite dislocations that are put at a distance r from each other, $\rho = b/2\alpha$, where α is defined by the core radius, $r_{core} = b/\alpha$, and is of the order of 1.

$$W_s = \begin{cases} 0 & \text{if} \quad r < r_{lim} \\ 2\pi r \frac{2-\nu}{2(1-\nu)}\frac{\mu b^2}{4\pi}\left(-\ln\left(\tan\frac{b}{8r}\right) - 2\cos\frac{b}{4r}\right) & \text{if} \quad r > r_{lim} \end{cases} \tag{C.6}$$

for $\alpha = 1$.

For twinning b is but a small fraction of the lattice constant: $b \simeq \epsilon_0 d_{(202)_{Fm\bar{3}m}}$, about 1/10. On the other hand, r is at least one lattice constant, but typically larger

[3] It reflects the fact that for distances closer to a threshold, the elastic approximation breaks down. This region is the core of the dislocation, which by definition does not sustain elastic stress.

than that. Hence $\tan b/(8r)$ is replaced by $b/(8r)$ and

$$W_s = \Delta G_{line}(r) = 2\pi r \frac{2-\nu}{2(1-\nu)} \frac{\mu b^2}{4\pi} \left(\ln \frac{4r}{\rho} - 2 \right) \tag{C.7}$$

It is apparent that if $\ln \frac{4r}{\rho} < 2$ then W_s becomes negative. The problem arises from the above approximation of small b, and is easily circumvented by requiring:

$$W_s = \begin{cases} 0 & \text{if} \quad r < \frac{1}{4} r_{lim} e^2 \\ 2\pi r \frac{2-\nu}{2(1-\nu)} \frac{\mu b^2}{4\pi} \left(\ln \frac{4r}{\rho} - 2 \right) & \text{if} \quad r \geq \frac{1}{4} r_{lim} e^2 \end{cases} \tag{C.8}$$

Surface energy

When a stacking fault is nucleated on an existing twin-boundary, no additional surface energy need be supplied. In other words, the only contribution of the fault energy to the total free energy occurs during homogeneous nucleation. The distinction is important in view of the observation[4] that the extension of an FSMAs occurs mostly by the thickening of *existing* twin bands. Formally, the increase of total free energy due to γ would simply be:

$$\Delta G_\gamma(r) = \begin{cases} \gamma & \text{homogeneous nucleation} \\ 0 & \text{nucleation on existing twin boundary} \end{cases} \tag{C.9}$$

(per unit fault surface.) Putting eqs. C.1 — C.9 together, the total energy is:

$$\Delta g(r) = \underbrace{\pi (d_{(202)} \Delta G^{2\to 1}_{mag}(H) + \Delta G_\gamma)}_{(1)} r^2 + (2\pi \Delta G_{line}) r \tag{C.10}$$

The part termed (1) in the above equation must be < 0, otherwise nucleation is not possible. A threshold field can readily be extracted from the resulting condition

$$d_{(202)} \Delta G^{2\to 1}_{mag}(H) < -\Delta G_\gamma \tag{C.11}$$

[4]High speed video of Ni–Mn–Ga single crystal actuation, Fig. 3-13.

since it implies that

$$H > \frac{2K_u}{M_s}(1 - \sqrt{1 - \frac{\Delta G_\gamma}{d_{(202)}\, K_u}}) \tag{C.12}$$

Note also the condition on the fault energy, $\gamma < d_{(202)}\, K_u$, imposed on homogeneous nucleation processes. From Fig. 1-5, for a tetragonality $\chi \equiv c/a = 0.94$, $d_{(202)} \simeq 0.25\,\text{nm}$ and the above condition becomes $\gamma \leq 0.03\,\text{erg/cm}^2$. For comparison one can take the intrinsic stacking fault energy for nickel [86], $\gamma = 125\,\text{erg/cm}^2$ or its twin-boundary energy [87], $\gamma = 43\,\text{erg/cm}^2$. It is concluded that either

- γ in Ni–Mn–Ga is much[5] smaller than in pure Ni or,
- homogeneous (field-induced) nucleation of twin-boundaries is not possible in Ni–Mn–Ga. This latter point is supported by the observation that it is necessary to "train" the FSMA by applying stress before field-induced strain can be observed (cf. Sec. 2.2.) It suggests that micro-twins are introduced in the otherwise perfect structure through stress, and that these micro-twins are sites for magnetically induced heterogeneous nucleation of monolayer twins. Recently, estimates for the magnetic field effects on dislocations placed the Peierls stress[6] at about 20 MPa [63]. Put in these terms, it is apparent that homogeneous nucleation should not be possible on the basis that the upper bound for the magnetic pressure on the twin-boundary is given by the magnetocrystalline anisotropy, and is $\approx 3.1\,\text{MPa}$.

[5] At least three orders of magnitude.
[6] The estimate was done for ferrous alloys.

If the driving force is < 0 however, one defines the critical radius as $r_c \equiv r : \Delta g(r)$ is maximum, and the barrier to nucleation Δg_c as the resulting energy increase[7]:

$$r_c = -\frac{\Delta G_{line}}{d_{(202)}\Delta G^{2\to 1}_{mag}(H)+\Delta G_\gamma}$$
$$\Delta g_c = -\frac{\pi \Delta G^2_{line}}{d_{(202)}\Delta G^{2\to 1}_{mag}(H)+\Delta G_\gamma} \qquad \text{(C.13)}$$

Numerical values for the critical radius can be obtained for the parameters of Table C.1.

Consider for example Fig. C-2. It is apparent from Fig. C-2(a) that for peak fields, when the driving force is saturated, the critical radius of a partial dislocation loop is about 7 nm (assuming that the stiffness in the material is 700 MPa — see Table C.1.) For larger stiffness (2000 MPa) the figure shows a correspondingly larger critical radius at the same driving force, about 25 nm. As the field increases during the progression of the pulse, the critical radius decreases. It is also apparent that the critical radius is initially quite large, requiring a large number of atoms to form a partial dislocation loop through a heterophase fluctuation. When the driving force saturates, there are about 1500 atoms in one such loop.

Note that the critical radius has a strong dependence on the elastic modulus (see Fig. C-3.)

C.1.2 Calculation of the nucleation flux

A nucleation events consists in an embryo of critical size increasing its radius. This happens through the addition of one atom to the faulted area (the embryo) when it is

[7]The definition of W_l in terms of a limit radius presents the possibility of barrier-less loop expansion. In general, as the radius of the partial dislocation loop is increased from zero, W_l is zero but the magnetic driving force is smaller than zero, driving the loop expansion. When the loop radius increases beyond $\frac{1}{4}/r_{lim}e^2$ there is a sharp increase in W_l that offsets the magnetic driving force in a certain range, rendering the total energy change positive (but increasing at ever slower rates with r, until it reaches the maximum at the critical radius) But for small W_l, r_c could become as small as to reach $\frac{1}{4}/r_{lim}e^2$. In that case, the line-tension never offsets the magnetic driving force and the formation of stacking fault loops requires no nucleation.

[8]As an approximation the value measured for Nickel [87] has been used.

Table C.1: Constants and properties of Ni–Mn–Ga used for the estimates of nucleation rates and critical quantities.

Symbol	Value	Description
K_u	1.9×10^6 erg cm^{-3}	magnetocrystalline anisotropy
M_s	484 emu cm^{-3}	saturation magnetization
H_{th}	(1.5 ± 0.2)kOe	threshold magnetic field for twin-boundary motion
ρ	8.1 g cm^{-3}	mass density
ϕ	0.508^2 cm^2	sample cross section
γ[8]	43 erg cm^{-3}	stacking fault energy
W_m	0.5 eV	barrier to atomic twinning shift
a	5.825×10^{-8} cm	lattice constant in $Fm\bar{3}m$
χ_γ	0.94	tetragonality in $Fm\bar{3}m$
ν	0.3	Poisson's modulus
EY	700 MPa	Young's modulus
ν_D	5×10^{13} s^{-1}	Debye frequency
kB	1.38×10^{-16} erg K^{-1}	Boltzmann constant
T	300 K	experiment temperature
ϵ_o	0.0619	twinning strain
$d_{(202)}$	2.45414×10^{-8} cm	distance between twin planes
b	3.03895×10^{-9} cm	twinning Burgers vector
ρ_l	3.43348×10^7 cm^{-1}	linear atomic density (perp. to t.d.)
ρ_a	8.58962×10^{14} cm^{-2}	surface atomic density (on tp.)
μ	2.69231×10^{11} erg cm^{-2}	shear modulus
W_l	4.1577×10^{-6} erg	dislocation line energy
γ_a	5.00604×10^{-14} erg cm^{-2}	per atom surface free energy

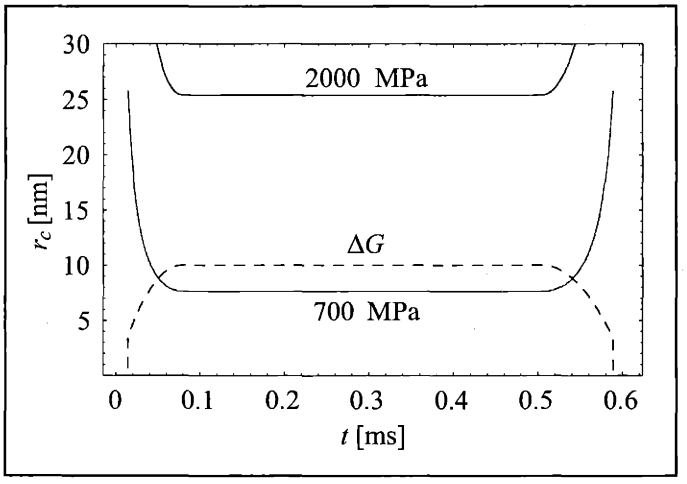

(a)

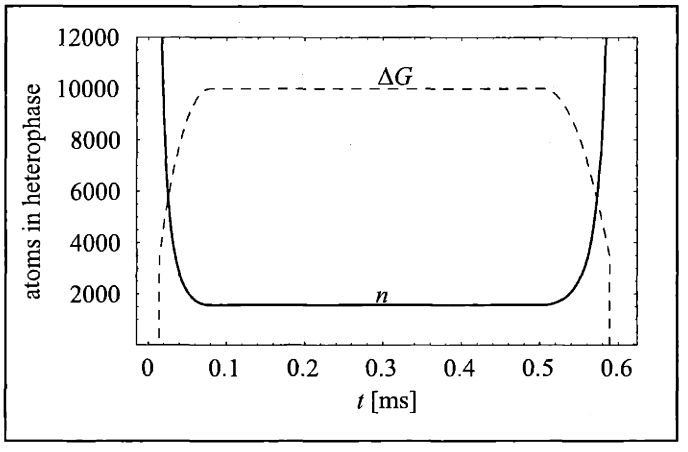

(b)

Figure C-2: (a) Radius of a critically sized partial dislocation loop (embryo) as a function of time during the evolution of the magnetic pulse from a 2 kV discharge (the driving force for twin-boundary motion it generates is indicated by the dashed curve, in arbitrary units.) The solid black curve is obtained for an elastic modulus of 2000 MPa, whereas the gray is obtained for a value of 700 MPa. (b) Atoms in an embryo of critical size vs. time during the evolution of the magnetic pulse of (a), for an elastic modulus of 700 MPa. At maximum driving force a critical embryo contains about 40 atoms. The dashed line corresponds to the applied magnetic field, which peaks at about 17.9 kOe (arbitrary scale.)

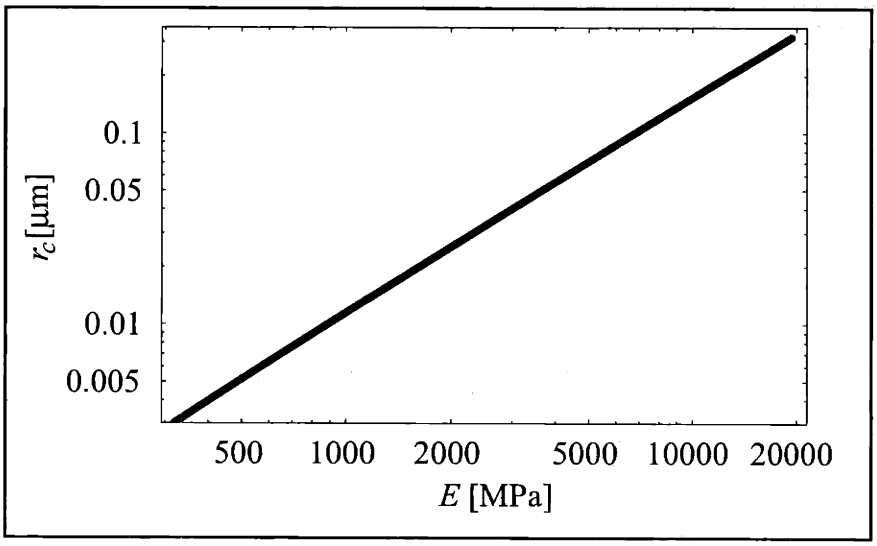

Figure C-3: Critical radius dependence on the stiffness E_Y of the material.

shifted by the Burgers vector for twinning. The theory of nucleation provides a way to estimate the rate at which nucleation events will take place.

A few assumptions have to be made to simplify the calculation of the nucleation rates:

- Nucleation events effectively remove the corresponding atoms from the ensemble of variant 2 atoms. This problem is formally the same as that in standard nucleation theory of liquids from a vapor phase [81]. The more careful treatment by Becker and Döring [82] is a correction to the former, which will not alter greatly the desired estimates for the nucleation rate.

- In the model, additional atoms are supplied to the ensemble for each nucleus formed, so that from this point of view a steady state may be attained. This approximation is called *quasi-steady state*[9] and is valid, strictly speaking, only at the onset of the nucleation process.

- The number of embryos of radius r_c that exist in this quasi-steady state can be approximated by the number existing in thermal equilibrium.

As can be seen for martensitic Ni–Mn–Ga in Fig. 1-1, there are 4 atoms on a given $(202)_{Fm\bar{3}m}$ plane per unit cell. Hence the atomic density on the twinning planes is:

$$\rho^{at}_{(202)} = 4/(3.19 \times 10^{-15}\,\mathrm{cm}^2) \simeq 1.25 \times 10^{15}\mathrm{at/cm}^2 \tag{C.14}$$

Consequently the number of atoms in an embryo will be

$$n(r) = \pi r^2 \rho^{at}_{(202)} \tag{C.15}$$

and likewise, there will be

$$N_2 = \phi \rho^{at}_{(202)} \tag{C.16}$$

atoms on a section of the sample with area ϕ, parallel to the (202) plane. These are the atoms that constitute the ensemble in which the nucleation theory calculates

[9] However, nucleation rates *can* vary if the driving force changes.

equilibrium distributions of embryos. The nucleation rate I = (nucleation events per unit time) will therefore be proportional to the probability λ_+ of such additional shift per unit time, and the number of existing embryos of critical size,

$$I = \lambda_+ N(r_c) \tag{C.17}$$

As required in the quasi-steady state approximation, the number of critical nuclei is given by:

$$N(r_c) = N_2\, e^{-\Delta g_{tot}(r_c)/kT} \tag{C.18}$$

To compute λ_+ an atom is considered which vibrates around its equilibrium position along the twinning direction, $[\bar{1}01]$), with frequency ν. ν can be approximated by the Debye frequency,ν_D. For displacements from equilibrium along the twinning direction, the atomic potential is a double-well, so that its position in variant 2 is metastable. A vibration will leave the atom permanently in variant 1 if it crosses an energy barrier of W_m separating the potential wells corresponding to either twin variant. Such vibration will happen with probability [88] $\lambda_{2\to1} = \exp(-W_m/kT)$, so that:

$$\lambda_+ = 4\, r_c\, \rho^{at}_{line}\, \nu_D\, e^{-W_m/kT} \tag{C.19}$$

where ρ^{at}_{line} is the density of atoms along the line perpendicular to the twinning direction, e.g. [010]). There are 2 atoms every 5.825 Å [89] (see. Fig. 1-1.) Therefore $\rho^{at}_{line} = \rho^{at}_{[010]} \simeq 3.4 \times 10^7$ /cm. For Nickel, the Debye temperature Θ_D is about 375 K, so that $\nu_D = k\,\Theta_D/\hbar \simeq 5 \times 10^{13}$ Hz. An estimate for W_m is required.

Substituting the above equations into Eq. (C.17) one arrives at:

$$I = \nu_D\, (4\, r_c \rho^{at}_{line})\, N_2\, e^{-(\Delta g_{tot}(r_c)+W_m)/kT} \tag{C.20}$$

or, in terms of nucleation events per (202)-surface,

$$i = \nu_D\, (4\, r_c \rho^{at}_{line})\, e^{-(\Delta g_{tot}(r_c)+W_m)/kT} \tag{C.21}$$

In Fig. C-4 the number of nuclei formed on a unit surface of the twin plane per unit time is depicted. This rate is the nucleation flux. It can be seen that the flux first

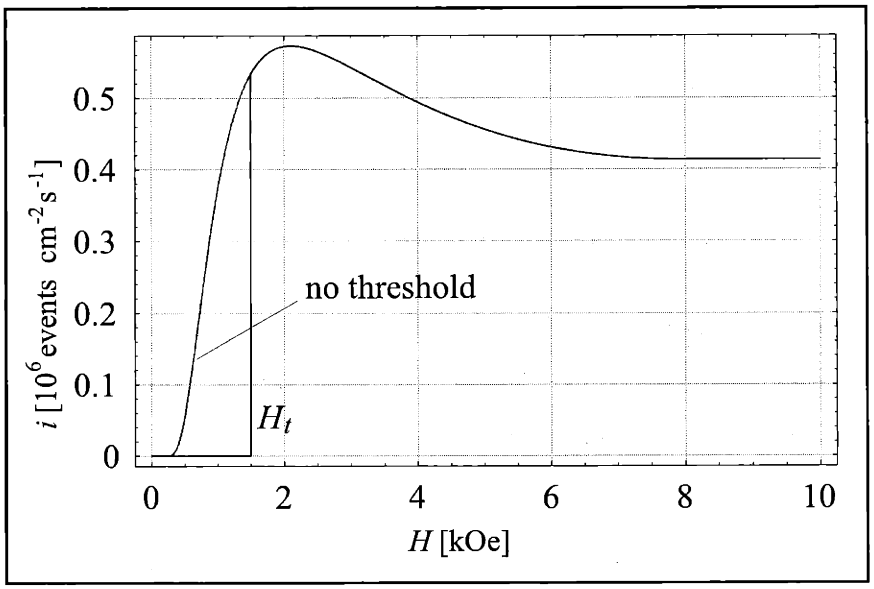

Figure C-4: Nucleation flux in units of nucleation events per cm^2 on a twin plane, per unit time. It first rises with increasing driving force (magnetic field), reflecting the lower nucleation barrier. As expected from Eq. (C.17) and Eq. (C.19), λ_+ also decreases with decreasing size of critical embryo. Therefore the nucleation flux maximum does not correspond with the largest driving force.

increases with increasing driving force (magnetic field) as is expected from the fact that the barrier for nucleation decreases. However, with the decrease of the barrier height comes a decrease in the critical radius, and that translates in a decrease of λ_+ (see Eq. (C.17) and Eq. (C.19).) Both factors contribute to the creation of a maximum of the flux for intermediate driving force.

The flux is extremely sensitive to the value of the parameters K_u, E_Y and W_m, and to the latter especially. This fact has obtained a recent confirmation [90]. Figure C-5 shows the results for variations of these parameters.

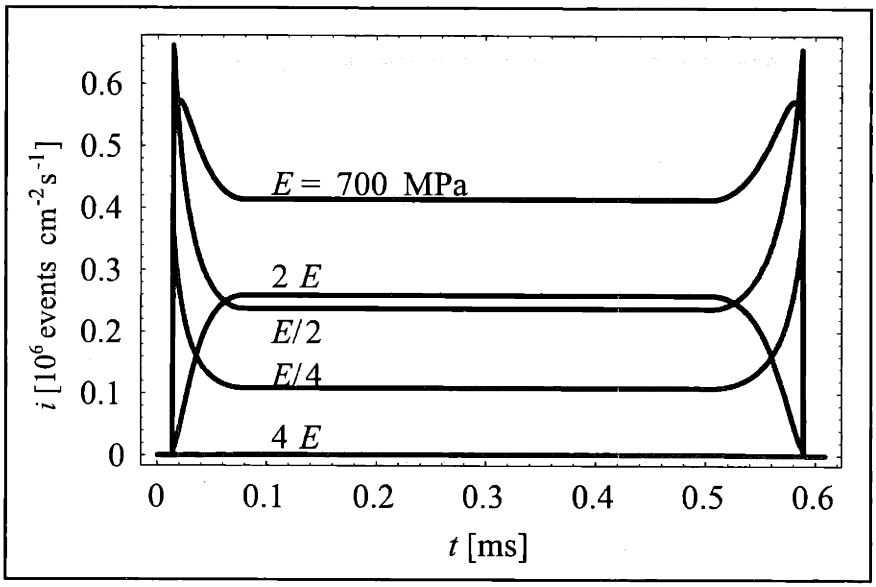

(a)

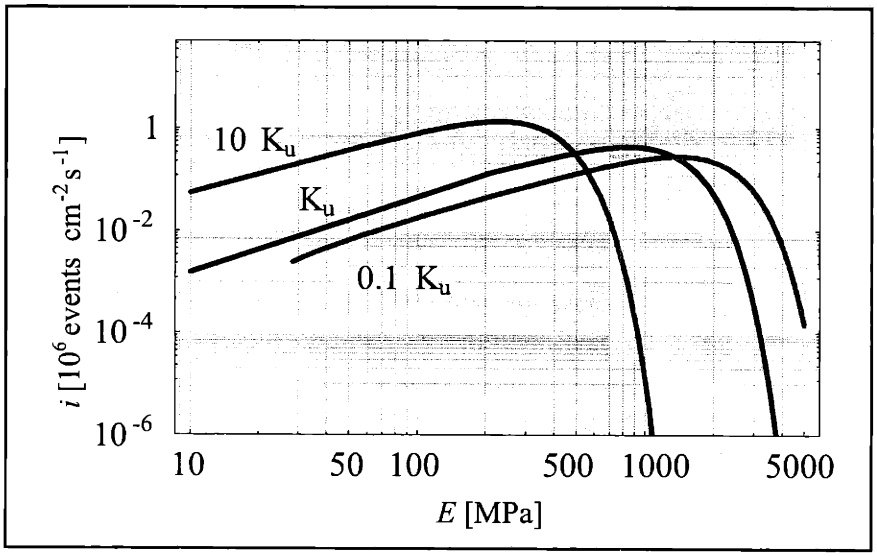

(b)

Figure C-5: Sensitivity analysis. (a) Nucleation flux for a 2 kV pulse for various stiffnesss. (b) Nucleation flux vs. stiffness showing the effect of a change in the order of magnitude of the magnetocrystalline anisotropy. The large effect is apparent.

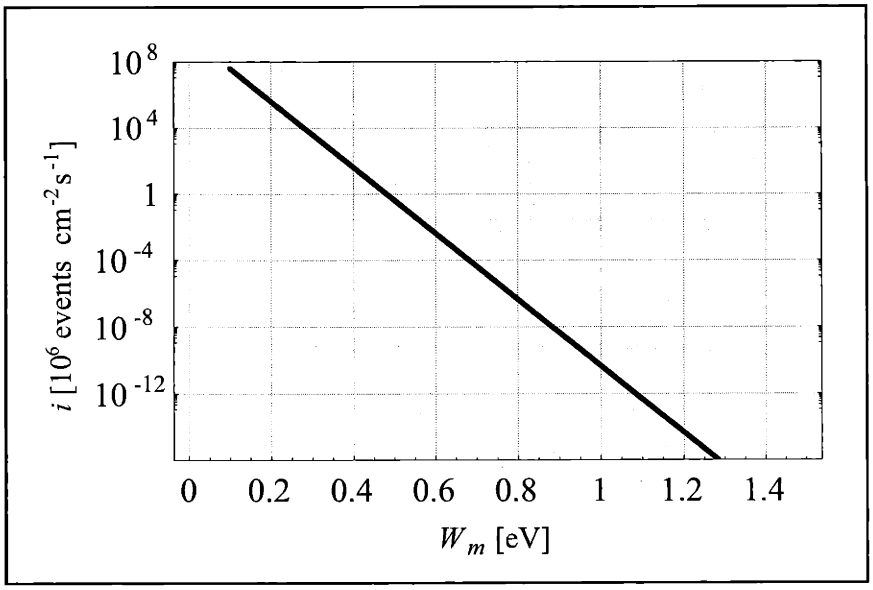

Figure C-5: (cont'd.) Sensitivity analysis. Nucleation flux vs. the energy barrier in the double well seen by an atom along the [$\bar{1}$01] direction. The extreme effect is apparent.

C.2 Nucleation as the rate-limiting process in twin-boundary motion

In this section nucleation as the process limiting twin-boundary motion is considered. Accordingly the assumption is that once nucleated, partial dislocations on a twin-boundary will expand in negligible time to cover its full extension. Consistently, it will be assumed that one nucleation event coincides with the motion of the twin-boundary one distance between (202) planes.

It is possible to distinguish a priori two nucleation channels: homogeneous and heterogeneous nucleation, each of which would contribute to the total nucleation flux. As discussed above, however, homogeneous nucleation can effectively be ruled out.

Let us assume that in the time interval $[t, t+\delta t]$ the probability of a nucleation event taking place on an existing twin-boundary is λ. λ will be determined by the nucleation flux and the length of the time interval δt: $\lambda = i(t)\delta t$. The time period of the experiment τ_e can be divided into δt intervals. There will be $n = \tau_e/\delta t$ such intervals. In a given interval j of these, the twin-boundary will jump one (202) distance if a partial dislocation is nucleated, or remain in the same position if no nucleation takes place. Let $\theta_j = 1$ designate the event "nucleation took place in the i-th interval, and likewise $\theta_j = 0$ designate the lack of nucleation in the i-th interval. With this definition, a collection $\Theta = \theta_1, \theta_2, ..., \theta_n$ will describe the specific sequence of jumps executed by the twin-boundary in the course of its motion, during the period studied, as shown in Fig. C-6.

The expected number of nucleation events n^e over the time period τ_e will be written as

$$\frac{n^e}{n} = \sum_{\Theta} \prod_{i=1}^{n} \lambda(t_i)^{\theta_j} (1 - \lambda(t_i))^{1-\theta_j} \tag{C.22}$$

Taking the nucleation flux to be constant over τ_e, one can compute n^e from the number n_a^e of exactly a nucleation events happening, by counting the number of different paths Θ. It is:

$$n_a^e = \frac{n!}{a!(n-a)!} \lambda^a (1-\lambda)^{n-a} \tag{C.23}$$

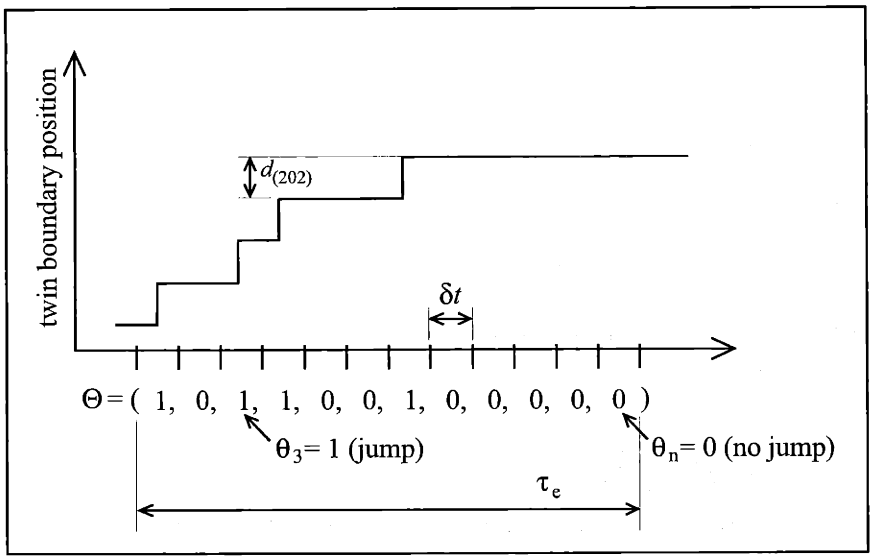

Figure C-6: Schematic of the motion of twin-boundary by jumps. Each time interval δt the twin-boundary either jumps $d_{(202)}$ because a nucleation event occurred ($\theta_j = 1$) or remains at its position ($\theta_j = 0$) when no nucleation took place.

This can be re-written as

$$n_a^e = \frac{1}{a!} \underbrace{n \prod_{j=1}^{a-1}(n-j)}_{(1)} \underbrace{\left(\frac{i\tau_e x}{1-i\tau_e x}\right)^a}_{(2)} \underbrace{(1-i\tau_e x)^n}_{(3)} \tag{C.24}$$

where for convenience $x \equiv 1/n$ was defined, and the sub-expressions (1)—(3) become (for $a \geq 2$):

$$(1) \;=\; n \sum_{j=0}^{a-1} \alpha_j \; n^e = x^{-1} \sum_{j=0}^{a-1} \alpha_j \; x^{-j} \tag{C.25}$$

$$(2) \;=\; (i\tau_e x)^a \sum_{k=0}^{\infty} (-1)^k (-i\tau_e x)^k \tag{C.26}$$

$$(3) \;=\; \left(1 + \frac{1}{-n/i\tau_e}\right)^{-\frac{n}{i\tau_e}(-i\tau_e)} \tag{C.27}$$

For a large number of subdivisions of the interval τ_e, $\delta t \to dt$ and concurrently $n \to \infty$ and $x dt/\tau_e \to 0$. Focusing on the lowest order in x in the product of expressions (1)

and (2) one can replace expression (3) with its limit.

$$\begin{aligned}(1)\times(2) &= (i\tau_e)^a \sum_{j=0}^{a-1} \alpha_j\, x^{a-j-1} \sum_{k=0}^{\infty} (-1)^k (i\tau_e x)^k = (i\tau_e)^a \sum_{j=0}^{a-1} \alpha_j\, x^{a-j-1} \sum_{k=0}^{\infty} (-1)^k (i\tau_e x)^k \\ &= (i\tau_e)^a \sum_{j=0}^{a-1} \alpha_{a-j-1}\, x^j \sum_{k=0}^{\infty} (-1)^k (i\tau_e x)^k = (i\tau_e)^a \sum_{j,k=0}^{a-1,\infty} (-1)^k (i\tau_e)^k \alpha_{a-j-1} x^{j+k} \\ &= (i\tau_e)^a \left(\alpha_{a-1} + (\alpha_{a-2} - \alpha_{a-1} i\tau_e)\, x + O[x^2]\right) \end{aligned} \tag{C.28}$$

where,

$$\begin{aligned}\alpha_{a-1} &= 1 \\ \alpha_{a-2} &= \sum_{j=1}^{a-1} j = \begin{cases} \frac{a^2-3a+2}{2} & \text{if } a \text{ is odd} \\ \\ \frac{a^2-3a+4}{2} & \text{if } a \text{ is even} \end{cases} \end{aligned} \tag{C.29}$$

Now taking $\lim \delta t \to dt\cdot$ on (1) $\times$ (2) and (3) one finds:

$$\begin{aligned}\lim_{\delta t \to dt} (1)\times(2) &= (i\tau_e)^a \\ \lim_{n\to\infty} (3) &= e^{-i\tau_e} \end{aligned} \tag{C.30}$$

Finally:

$$n_a^e = \frac{1}{a!}\,(i\tau_e)^a\, e^{-i\tau_e} \tag{C.31}$$

which can be seen to be the correct expression also for the results for $a = 0, 1$. Now it remains to sum over all possible a's, and so obtain the expected number of monolayer twin transitions, n^e:

$$n^e = \sum_{a=0}^{a_{max}} \frac{a}{a!}\,(i\tau_e)^a\, e^{-i\tau_e} \tag{C.32}$$

Given that $a_{max} = (\text{untransformed length})/d_{(202)}$ one can take $a_{max} \to \infty$:

$$n^e \simeq \sum_{a=0}^{\infty} \frac{a}{a!}\,(i\tau_e)^a\, e^{-i\tau_e}$$

$$= e^{-i\tau_e}(i\tau_e)\frac{d}{d(i\tau_e)}\sum_{a=0}^{\infty}\frac{(i\tau_e)^a}{a!} = i\tau_e \tag{C.33}$$

Note that these expressions are valid for a given point in time τ_e, for which one can replace the actual nucleation flux with a constant. Using the same expression as the expected volume fraction transformed requires an expression for i, namely:

$$i(\tau_e) = \frac{1}{\tau_e}\int_0^{\tau_e} i(t')dt' \tag{C.34}$$

Thus naturally one obtains that the length (along the twin plane normal) of variant 2 transformed is proportional to the integral of the nucleation flux up to the time of interest. Since this result is valid for each moving twin-boundary, when there are m mobile twin-boundaries, the length transformed $\delta x$is:

$$\delta x(t) = d_{(202)}\int_0^t m(t')i(t')dt' \tag{C.35}$$

Of course, the rate of extension is thus just:

$$v = \frac{d\delta x}{dt}(t) = d_{(202)}m(t)i(t) \tag{C.36}$$

A caveat: A good part of the extension seems to happen at the early stages of the field build up, so that there the nucleation flux is not constant.

C.3 Pinning of partial dislocations

Observations[10] suggest that kinetics of overcoming defects can be rate limiting. In this section, this case will be considered, and the existence of that partial dislocations will be assumed.

Following [91] one identifies different times that characterize the motion of a dislocation, as shown in Fig. C-7.

[10]Driving forces that do not cause full transformation of the variant 2 region into variant 1 *can* cause (repeatedly) the apparently unhindered motion of discrete twin-boundaries. For example see Fig. 3-14.

- τ_e is the time of the experiment. In the present case this would correspond to the acquisition time of the oscilloscopes.

- τ_m is the time over which the velocities are measured. This corresponds to the smallest resolved time interval, a few μs in the present experiment.

- τ_f is the time during which a partial dislocation is moving freely. Presumably, this time is shorter than the smallest resolved time in this case.

- τ_w is the time that the partial dislocation spends "waiting" while pinned at a defect.

Accordingly, a partial dislocation that moves under the action of a driving force, may do so unhindered by pinning obstacles at speed v_f over a relatively short *free travel* time τ_f. It then is pinned by a defect that presents itself as a barrier of height ΔG_B, and precluded from further motion for a *waiting* time τ_w until thermal activation or the increase of driving force push it free. The process is then repeated. Consequently, over the time scale τ_m of a measurement[11], the partial dislocation will have an average velocity $\overline{v}^{\perp}$, which can vary throughout the time of the experiment τ_e.

C.3.1 Twin boundary displacement limited by pinning

Consider a twin-boundary (202) that is moving under the action of a field but can be pinned by defects in the crystal[12]. Once the (202) plane has been swept out by the partial dislocations, the twin-boundary will have advanced the distance $d_{(202)}$. Assume further that the twin-boundary velocity will be proportional to the average speed of the partial dislocations that sweep out (202). The specifics of the expansion of partial dislocations on (202) will be considered only inasmuch as they reflect the fact that the pinning of a twin-boundary is really the pinning of the partial dislocations that move across it. The motion will require overcoming an energy barrier ΔG^b (the

[11] In the present case, this would be Δt in Eq. (C.37) (1 μs experimentally.)

[12] For example micro-cracks, voids and incompatible twin systems can stop the motion of partial dislocations.

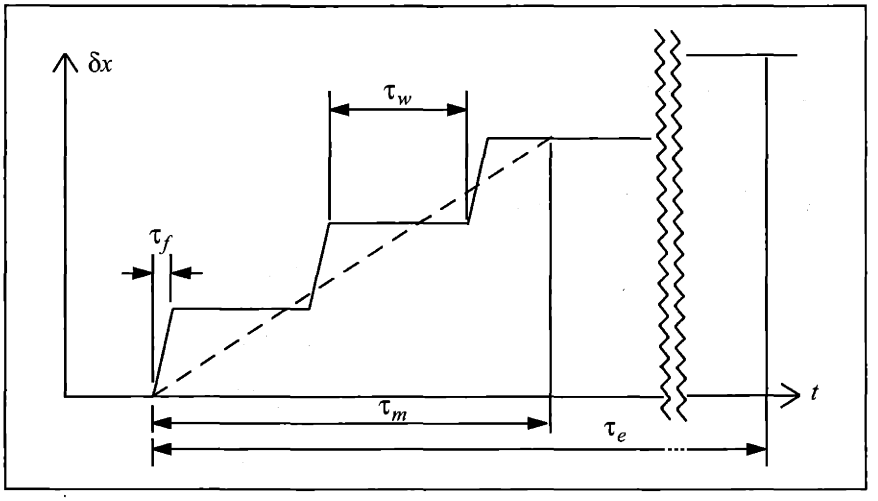

(a)

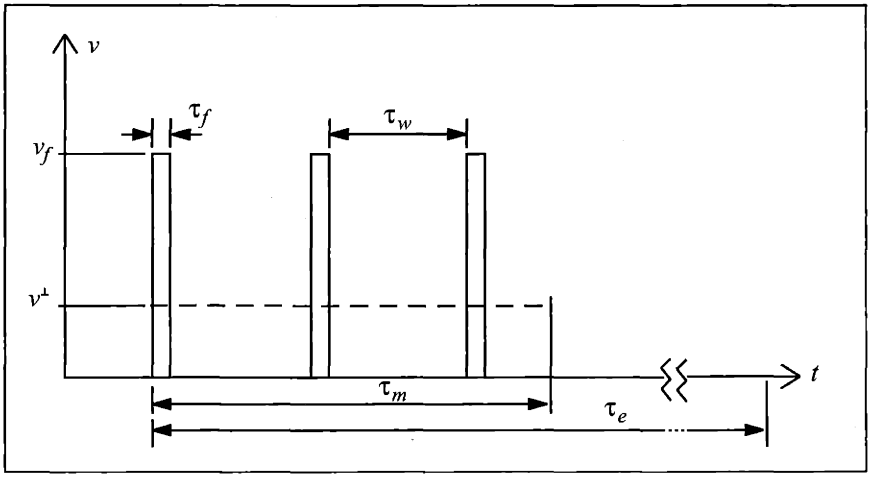

(b)

Figure C-7: (a) Characteristic times during the motion of a dislocation, after [91]. (b) Effective velocity of the dislocation over the characteristic times given in (a).

work done by the forces required to move the partial dislocation past the defect that is pinning it), and will be driven by the driving force for twin-boundary motion ΔG. It can be written for twin-boundary velocity:

$$\overline{v}^{tb} = \frac{\text{distance moved } \perp \text{ (202)}}{\text{unit time}} = c\, e^{-(\Delta G^b + \Delta G)/kT} \tag{C.37}$$

where c is a constant that has the units of velocity, and establishes the relation between the motion of the twin-boundary from one (202) plane to the next and the mechanics of the motion of the partial dislocations on (202). In this section c is taken to be constant. ΔG is an explicit function of t through the field $H = H(t)$. ΔG^b is primarily a function of the position along the twin plane normal of the pinning defects, and depends of the time through the position of the twin-boundary. Note that Eq. (C.37) is then an *instantaneous* velocity. The measured velocities are instead the averages over the measurement time τ_m (see Fig. C-7(a)).

The total displacement x of the twin-boundary during $t < \tau_m$, will be:

$$x = \int_0^t \overline{v}^{tb}(t')\, dt' = c \int_0^t \underbrace{e^{-\Delta G/kT}}_{A(t')} \underbrace{e^{\Delta G^b/kT}}_{B(x(t'))} dt' \tag{C.38}$$

In a manner analogous to Eq. (C.38) one can calculate the displacement during the time interval $\delta t = \tau_f + \tau_w$, defined as the time interval starting when the partial dislocations de-pin up to the point where having waited τ_w they are about to de-pin again, as:

$$\delta x = c \int_t^{t+\delta t} e^{-\Delta G/kT} e^{-\Delta G^b/kT} dt' \tag{C.39}$$

From Fig. C-7 τ_f is the time before the next pinning event, and τ_w the time the boundary remains pinned: $\delta t = \tau_f + \tau_w$. Then Eq. (C.39) can be re-written as:

$$\delta x = c \int_t^{t+\tau_f} e^{\Delta G/kT} \underbrace{e^{\Delta G^b/kT}}_{=1} dt' + \int_{t+\tau_f}^{t+\delta t} e^{\Delta G/kT} e^{\Delta G^b/kT} dt' \tag{C.40}$$

where the term over the braces is equal to 1 because between pinning events it is assumed that the barrier is negligible.

It is convenient now to divide the problem in two limit cases. If the speed of the

moving partial dislocations is very large, then they spend most of their time pinned: $\tau_w \gg \tau_f$. On the contrary, when they move very slowly the converse is true: $\tau_f \gg \tau_w$.

Case $\tau_f \gg \tau_w$

It is possible to expand the above Eq. (C.40) to first order in τ_w.

$$\begin{aligned}\frac{\delta x}{c} &= \int_t^{t+\delta t} e^{\frac{\Delta G(t')}{kT}} dt' + (-\tau_w) e^{\frac{\Delta G(t+\delta t)}{kT}} - e^{\frac{\Delta G(t+\delta t)}{kT}} e^{\frac{\Delta G^b(t+\delta t)}{kT}} (-\tau_w) + O[{\tau_w}^2] \\ &= \int_t^{t+\delta t} e^{\frac{\Delta G(t')}{kT}} dt' + \tau_w e^{\frac{\Delta G(t+\delta t)}{kT}} \left(e^{\frac{\Delta G^b(t+\delta t)}{kT}} - 1 \right) + O[{\tau_w}^2]\end{aligned} \tag{C.41}$$

Assuming that there is one representative pinning strength, $\Delta G^b = E, t \in [t + \delta t - \tau_w, t + \delta t] \; \forall \; t$ (ie. for all pinning events), the sum over all the pin–de-pin intervals δt becomes

$$\frac{x}{c} = \sum_{\delta t} \frac{\delta x}{c} \simeq \int_0^{\tau} e^{\frac{\Delta G(t')}{kT}} dt' + \left(e^{\frac{E}{kT}} - 1 \right) \sum_{\delta t} \tau_w e^{\frac{\Delta G(t+\delta t)}{kT}} \tag{C.42}$$

Consider fig. C-8. With $\tau_w \ll \delta t$ the driving force is approximately constant

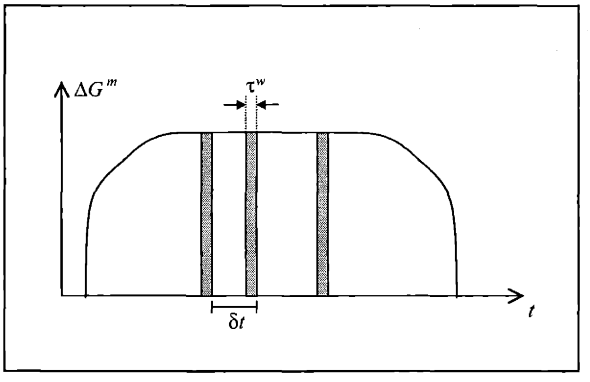

Figure C-8: Driving force for twin-boundary motion vs. time. A time interval δt is defined from the break-away event to the next. The time of free motion is τ_f and the time of pinning is τ_w. The product of τ_w and the driving force at the end of the interval δt is approximately equal to the shaded rectangle of the figure. In turn, for small δt the latter can be approximated by the integral over $[t + \tau_f, t + \delta t]$, or a fraction $\tau_w/\delta t$ of the integral over δt.

during the step δt, and it is possible to use:

$$\tau_w e^{\frac{\Delta G(t+\delta t)}{kT}} \simeq \int_{t+\tau_f}^{t+\delta t} e^{\frac{\Delta G(t')}{kT}} dt' \simeq \frac{\tau_w}{\delta t} \int_{t}^{t+\delta t} e^{\frac{\Delta G(t')}{kT}} dt' \tag{C.43}$$

If the pinning strength is the same for all pinning sites, one can replace τ_w with the average pinning time $\langle \tau_w \rangle$, and get:

$$\frac{x}{c} \simeq \left(1 + \frac{\langle \tau_w \rangle}{\langle \delta t \rangle} \left(e^{\frac{E}{kT}} - 1\right)\right) \int_0^{\tau} e^{\frac{\Delta G(t')}{kT}} dt' \tag{C.44}$$

Case $\tau_f \ll \tau_w$

Expanding Eq. (C.40) to first order in τ_f.

$$\frac{\delta x}{c} \simeq \tau_f \, e^{\frac{\Delta G(t)}{kT}} + \int_t^{t+\delta t} e^{\frac{\Delta G(t')}{kT}} e^{\frac{\Delta G^b(t+\delta t)}{kT}} dt' - \tau_f e^{\frac{\Delta G(t)}{kT}} e^{\frac{\Delta G^b(t)}{kT}} \tag{C.45}$$

Again assuming that there is only one kind of pinning strength, $\Delta G^b(x(t)) = E, t \in [t_i + \delta t - \tau_w, t_i + \delta t] \; \forall \; t_i$ (ie. for all pinning events.) Summing over all the pin–de-pin intervals δt (or corresponding δx),

$$\begin{aligned} \frac{x}{c} &= \sum_{\delta t} \left(\tau_f \, e^{\frac{\Delta G(t)}{kT}}\right) + \sum_{\delta t} \left(\int_t^{t+\delta t} e^{\frac{\Delta G(t')}{kT}} e^{\frac{\Delta G^b(t+\delta t)}{kT}} dt'\right) - \sum_{\delta t} \left(\tau_f e^{\frac{\Delta G(t)}{kT}} e^{\frac{\Delta G^b(t)}{kT}}\right) \\ &= \sum_{\delta t} \left(\tau_f \, e^{\frac{\Delta G(t)}{kT}}\right) + \int_0^{\tau} e^{\frac{\Delta G(t')}{kT}} e^{\frac{E}{kT}} dt' - \sum_{\delta t} \left(\tau_f e^{\frac{\Delta G(t)}{kT}} e^{\frac{E}{kT}}\right) \end{aligned} \tag{C.46}$$

With considerations similar to the prior case,

$$\begin{aligned} \frac{x}{c} &\simeq \frac{\langle \tau_f \rangle}{\langle \delta t \rangle} \int_0^{\tau} e^{\frac{\Delta G(t)}{kT}} dt' + \int_0^{\tau} e^{\frac{\Delta G(t')}{kT}} e^{\frac{E}{kT}} dt' - \int_0^{\tau} \frac{\langle \tau_f \rangle}{\langle \delta t \rangle} \rangle e^{\frac{\Delta G(t)}{kT}} e^{\frac{E}{kT}} dt' \\ &= \left(1 + \frac{\langle \tau_f \rangle}{\langle \delta t \rangle} (1 - e^{\frac{E}{kT}})\right) \int_0^{\tau} e^{\frac{\Delta G(t)}{kT}} dt' \end{aligned} \tag{C.47}$$

Individual twin-boundary motion

From eqs. (C.44) and (C.47) it is seen that regardless of the relative lengths of time that partial dislocations are freely moving or waiting on a pinning site, the total

displacement of a twin-boundary is:

$$x \propto \int_0^{\tau} e^{\frac{\Delta G(t')}{kT}} dt' \tag{C.48}$$

Accordingly, regarding the displacement of individual twin-boundaries in response to a time-varying driving force, a proper choice for the abscissa would be the expression given by the above eq. (C.48). Notice that Eq. (C.48) can always be rewritten as

$$x \propto \tau e^{\frac{\Delta G(\tau^\star)}{kT}} \tag{C.49}$$

where $\tau^\star \in [0, \tau_e]$. Particularly for the larger pulses in the present experiment, $\tau^\star \simeq t(\text{peak } H)$.

C.3.2 Application

Let us consider a single active twin-boundary and faults expanding on it. Faults will be pinned at defects and dwell at the pinning sites until thermal activation causes them to overcome the barrier and de-pin. It can be shown [66] that even though there exist a variety of defects and pinning barriers, the average dislocation velocity $\overline{v}$ still follows an Arrhenius-type law:

$$\overline{v}^{\perp} = \overline{v}^{\perp}{}_0 \, e^{-\Delta G^{\ddagger}/kT} \tag{C.50}$$

Here $\Delta G^{\ddagger}$ is the saddle point separating local minima in the energy of the system:

$$\Delta G^{\ddagger} = \Delta G^b - V\Delta G \tag{C.51}$$

and $\overline{v}^{\perp}{}_0$ is a velocity, given by:

$$\overline{v}^{\perp}{}_0 \simeq \frac{\overline{\lambda} b \nu_D}{\overline{l}_{\sigma,T}} \tag{C.52}$$

where b is the Burgers vector of the stacking fault, ν_D is the Debye frequency of the crystal and $\overline{l}$ is the average distance between pinning sites on the dislocation line, and

$\overline{\lambda}$ is the average distance from the energy valley to the saddle point of activation.

For order of magnitude estimates, one can relate the velocity of the stacking fault ($\overline{v}^{\perp}$) to that of the advancing twin-boundary ($\overline{v}^{tb}$) making simple assumptions about the distances swept out. The twin-boundary will advance a distance equal to the lattice constant along the twin plane normal, $d_{(202)}$ every time the partial dislocation sweeps out the twin plane. Let us assume that this requires a partial dislocation segment to move a distance $\phi^{1/2}$ if the partial dislocation is to sweep out the area ϕ. Consequently,

$$\overline{v}^{tb} = d_{(202)}\phi^{-1/2}{\overline{v}^{\perp}}_0 \; e^{-V\Delta G^{\ddagger}/kT} \tag{C.53}$$

which is also of Arrhenius type.

$$V = \overline{l}\overline{\lambda}d_{(202)} \tag{C.54}$$

With this one can re-write eq. (C.53) as

$$\overline{v}^{tb} = \underbrace{d_{(202)}\phi^{-1/2}{\overline{v}^{\perp}}_0 \; e^{\Delta G^b}}_{\equiv {\overline{v}^{tb}}_0} \; e^{k\,\frac{\Delta G}{K_u}} \tag{C.55}$$

where for convenience ${\overline{v}^{tb}}_0$ above and $k = (K_u V)/(kT)$ have been defined.

The expression of Eq. (C.55) is the basis for the plots of Fig. C.55 in Chapter 4. It is possible to find the slope of plots from the logarithm of the rate of extension vs. the driving force. Because of the difficulty determining the velocity accurately at the onset of the deformation, peak rate of extensions will be considered.

C.4 Concurrent nucleation and expansion of the partial dislocations

When the driving force for twin-boundary motion is constant (in the present experiments this occurs when the driving force saturates at K_u) it is possible to find relatively simple expressions for the progress of a transformation when there is concurrent

nucleation and growth of the transformed phase. For example, one can obtain the well-known Johnson-Mehl-Avrami-Kolmogorov equation [92] for the volume fraction ζ^V transformed:

$$\zeta^V = 1 - e^{-(\pi/3)IG^3t^4} \tag{C.56}$$

where I is the nucleation rate, and G is the growth rate. A conceptually different method leading to the same results was presented more recently by Cahn [93]. This *time-cone* method presents the advantage that the geometry of the volume in which nucleation is taking place is easily incorporated. In it, for a physical space of dimensionality d a space Ω of dimensionality $d+1$ is constructed, where the $(d+1)$-th dimension is time. At a given time t, a point x is considered, and the question is posed of whether this point does or does not belong to the untransformed part of space. The answer depends on whether or not a transformed region nucleated nearby at an earlier time, so that growth accounted for, x will be contained in the transformed volume at time t. The subset of Ω such that any point in it would result in x being transformed at time t is termed Ω_c.

Cahn shows that the volume fraction transformed ζ is related to the average number of nuclei $\langle N_c \rangle$ that could form in Ω_c by:

$$\zeta = 1 - e^{-\langle N_c \rangle} \tag{C.57}$$

The case of interest in twin-boundary motion is the nucleation and growth of stacking faults on a given twin plane, labelled "1". It can be described with the above method using a dimensionality $d = 2$. Accordingly, Ω_c will have a cone-like shape, with a tip at the point (x, t), an axis parallel to the time axis, and a cross section that increases as earlier times are considered.

For a constant nucleation flux I, and a constant growth rate $\overline{v}^{\perp}$, Ω_c becomes strictly speaking conical, and it is obtained for the fraction transformed ζ_1:

$$\zeta_1 = 1 - e^{-I\Omega_c} = 1 - e^{-(\pi/3)\overline{v}^{\perp 2}t^3} \tag{C.58}$$

where the underscore 1 indicates that the fraction transformed in plane 1 is being considered.

The result is useful in expressing the area covered by the stacking faults expanding on a twin plane. Let A_1 be said area, and let ϕ be the total area spanned by the twin plane in the given sample.

Then

$$\frac{A_1(t)}{\phi} = \zeta_1(t) = 1 - e^{-I\Omega_c(t)} = 1 - e^{-(\pi/3)\overline{v}^{\perp 2}t^3} \tag{C.59}$$

directly as before. Equation (C.62) gives a sigmoidal profile for $A_1(t)$.

A criterion to determine the time a set of partial dislocations take to sweep out a given twin plane could be easily developed. A certain area fraction ζ_1^{th} could be set as a threshold that must be exceeded before the twin plane is considered to have been swept out. The corresponding time is then found as $t:\ \zeta_1(t) = \zeta_1^{th}$.

Unfortunately, this criterion does not provide a clear relation between the twin twin-boundary velocity $\overline{v}^{tb}$ and the average velocity $\overline{v}^{\perp}$. The problem resides in the fact that once a finite area A_1 has been swept out on the plane 1, partial dislocations could start being nucleated on the plane right above plane 1. Consequently, by the time plane 1 has been swept out a significant fraction of plane 2 has already been swept out. Underestimating this fact results in unrealistically high $\overline{v}^{\perp}$ for the given experimental values of $\overline{v}^{tb}$ (see Chapter 4.)

As a first approximation to circumventing the above mentioned difficulty, it is possible to calculate the fraction of the area of the twin plane "2" (directly above plane 1) swept out by partial dislocations. Notice that in this case the area on which partial dislocations can nucleate and grow is not constant, but $A_1(t)$. This implies that not all time-cones have the same origin $t = 0$ in time. In fact, they will reach back in time only as far as there was a fault present in the plane below at a given position. Therefore, even at constant nucleation rates and $\overline{v}^{\perp}$, $\langle\Omega_c\rangle = \langle\Omega_c(t)\rangle$.

Approximate solution 1

Equation (C.62) can be used directly if the complication of the time dependence of $\langle \Omega_c(t) \rangle$ is disregarded.

As soon as a partial dislocation loop has stabilized[13] new loops can nucleate on the stacking fault. These loops would generate on the following twin plane, which is $d_{(202)}$ away from plane 1, and will be called plane 2. By similar arguments as before, the fraction of the fault area that is swept out by partial dislocation loops in plane 2 is

$$\zeta_2 = 1 - e^{-\frac{\pi J \bar{v}^{\perp 2} (t-t_2)^3}{3}} \tag{C.60}$$

and it can be seen by induction that in general, for plane i it is:

$$1 - \zeta_i = e^{-\frac{\pi J \bar{v}^{\perp 2} (t-t_i)^3}{3}} \tag{C.61}$$

The area that will not be swept out on the n-th plane at time t will be:

$$\begin{aligned} \frac{A_n(t)}{\phi} &= \frac{A_n}{A_{n-1}} \frac{A_n - 1}{A_{n-2}} \cdots \frac{A_1}{\phi} = \\ &= \zeta_n \zeta_{n-1} \cdots \zeta_1 = \\ &= 1 - e^{-\frac{\pi J \bar{v}^{\perp 2} (t-t_i)^3}{3}} \end{aligned} \tag{C.62}$$

The resulting area fractions are seen in Fig. C-9.

The times for which the area fraction ζ_i reaches a threshold $\zeta_t h$ can serve to determine the passage of a twin-boundary past the twin plane i, and differences between these times leads to an expression for the twin-boundary velocity. Figure C-10 plots the position of the twin-boundary, as the (202) plane that has been 50% swept out by partial dislocations.

There is a problem in that the twin-boundary seems to accelerate. This artifact is a direct consequence of the approximation that Ω_c is independent of t. It could be circumvented by arbitrarily taking only the first few twin planes for the computation

[13] Partial dislocation loops with radii larger than the critical radius are stable, see App. C

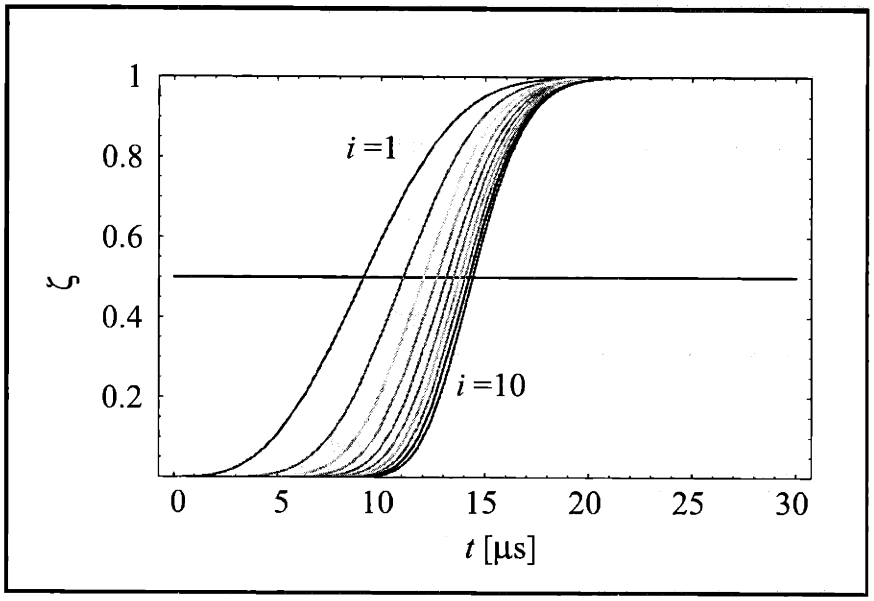

Figure C-9: Area fractions swept out by partial dislocations on successive twin planes, as per Eq. (C.62). The straight line corresponds to an arbitrary level of 0.5. $i = 1$ corresponds to ζ_1 and plotted is also the result for 9 successive twin planes (moving from left to right.) The times at which the curve i reaches the level of 0.5 mark the passage of the twin-boundary past the twin plane i. A nucleation rate of 10^6 nuclei per $\mathrm{s\,cm^2}$ and a $\overline{v}^{\perp}$ of $2.9 \times 10^5\,\mathrm{cm\,s^{-1}}$ has been assumed.

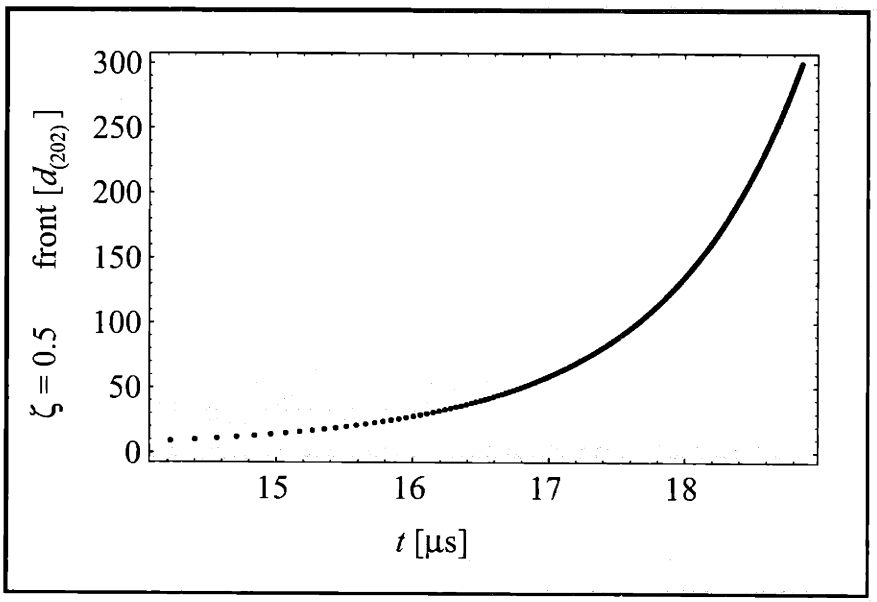

Figure C-10: Position of the twin-boundary — Approximation 1. An acceleration of the twin-boundary is apparent.

of $\overline{v}^{tb}$, but this is tantamount to fitting the $\overline{v}^{\perp}$ to the measured values of $\overline{v}^{tb}$.

Approximate solution 2

As discussed, even at constant nucleation rates and $\overline{v}^{\perp}$, $\langle\Omega_c\rangle = \langle\Omega_c(t)\rangle$. Accounting for this special restriction, the probable untransformed fraction on plane 2, $1-\zeta_2$ will be given by an equation similar to Eq. (C.62), but with a modified expression for $\langle\Omega_c(t)\rangle$. Write first:

$$\langle\Omega_c(t)\rangle = \int_0^t \Omega_c(t-\tau)\wp(\tau)d\tau \tag{C.63}$$

where $\wp(\tau)$ is the probability that a stacking fault actually swept by underneath the point of interest exactly at time τ.

$\Omega_c(t-\tau)$ has the same expression used earlier:

$$\Omega_c(t-\tau) = \frac{\pi}{3}\overline{v}^{\perp 2}(t-\tau)^3 \tag{C.64}$$

To obtain $\wp(\tau)$ consider that integrated from zero to t it gives the area untransformed on plane 1:

$$\int_0^t \wp(\tau)d\tau = 1-\zeta_1(t) \tag{C.65}$$

Therefore:

$$\wp(t) = -\frac{\zeta_1(t)}{dt} \tag{C.66}$$

so that Eq. (C.63) becomes

$$1-\zeta_2 \;=\; -\int_0^t \Omega_c(t-\tau)\frac{d\zeta_1(\tau)}{d\tau}d\tau = \tag{C.67}$$

Equation (C.67) is much better suited to the purpose of estimating average velocity. Again, a threshold fraction of the twin plane can be defined for which the twin-boundary will be said to be located at that plane. The difference between the times at which this happens on plane 1 and plane 2 will the time it takes a twin-boundary to move from one twin plane to the next.

If the threshold is taken to be 0.5[14], it is obtained:

$$\begin{aligned} \zeta_1(t_1) &= 1/2 \\ \zeta_2(t_2) &= 1/2 \\ \delta t &\equiv t_2 - t_1 \end{aligned} \tag{C.68}$$

so that the twin-boundary velocity will be:

$$\overline{v}^{tb} = \frac{d_{(202)}}{\delta t} \tag{C.69}$$

Equation (C.68)–(C.69) relates $\overline{v}^{tb}$ to $\overline{v}^{\perp}$.

[14]Indicating that the twin-boundary passed by a given twin plane if more than half of the twin plane has been swept out by partial dislocations.

Appendix D

Field-induced strain in textured polycrystals

D.1 Introduction

Single crystals of ferromagnetic shape memory alloys have displayed large magnetic field induced strains. A single crystal of $Fe_{70}Pd_{30}$ produced 0.5% strain in a field of 12 kOe at $-17°C$ [31]. More recently, an off-stoichiometry Ni–Mn–Ga crystal gave a reversible strain of 6% in 4 kOe at room temperature [39].

The mechanism of this large field-induced strain in ferromagnetic shape memory alloys is magnetically induced twin-boundary motion. The magnetic moments of an ferromagnetic shape memory alloy are strongly pinned to magnetic easy axes, due to a large magnetocrystalline anisotropy. They are different in each twin variant. The applied field selects between variants, causing the growth of those in which the magnetization is more closely aligned with the field, at the expense of the others.

Models for strain in ferromagnetic shape memory alloys have to date focussed on single crystals. In an extension of a micromagnetic model of magnetostriction in Terfenol, James and Kinderlehrer [94] gave a numerical prediction of the strain $e(\mathbf{H})$ as well as images of the twin variant rearrangements. Due to the complexity of the crystal interactions it has not yet led to analytic expressions for field induced strain. O'Handley [30] used an energy minimization approach in a two-variant system (one

twin-boundary) to get analytical expressions for $\mathbf{M}(\mathbf{H})$ and $e(\mathbf{H})$. This model gives a reasonable fit to the magnetization and strain observed in Ni–Mn–Ga [28].

In spite of the unusually large strains demonstrated in ferromagnetic shape memory alloys, applications in engineering devices may be severely limited if the large strains can only be achieved in single crystals. This paper presents an extension of O'Handley's [30] model for single-crystal ferromagnetic shape memory alloys to arrangements of differently oriented crystallites. The model computes an average strain, and thus gives an upper (Sachs) bound to the field induced strain. In contrast, Bhattacharya et al [70] give a lower (Taylor) bound to the polycrystal problem using linear programming.

D.2 Description of the Model

In the model, each of the single crystals will be influenced by its neighbors only through an effective stiffness C, but there is no explicit coupling. At zero magnetic fields, the crystals are assumed to have equal volume fractions of either twin variant, each of which is subdivided into 180^o domains. For simplicity the magnetocrystalline anisotropy is taken to be large enough for the rotation of the local magnetic moment away from the local easy axes to be negligible. This restriction is stronger than in [30]. Once the field is turned on, there is a driving force for twin-boundary motion in a crystal, arising from the different orientations with respect to H of the magnetization in its two twin variants. However, instead of inducing the rotation of the local magnetic moment M_s, the field causes the crystal structure to shear via twinning. In this process, the volume fraction of the twin variant with easy magnetic axis closer to the field direction increases. This is magnetically induced twin-boundary motion.

The driving force for twin-boundary motion is opposed by elastic restoring forces, so that in equilibrium the imbalance in the volume fraction of the variants is $\Delta x = \frac{H_t M_s \sin\Omega}{C\epsilon_o^2}$, where H_t is the component of the field along the twinning direction, and the other quantities are defined in Fig. D-1. Δx causes a shear in the plane of the twinning direction $\hat{t}$ and twin plane normal $\hat{n}$ of magnitude $\epsilon^{(c)}(H_t) = -\epsilon_0 \Delta x(H_t)$,

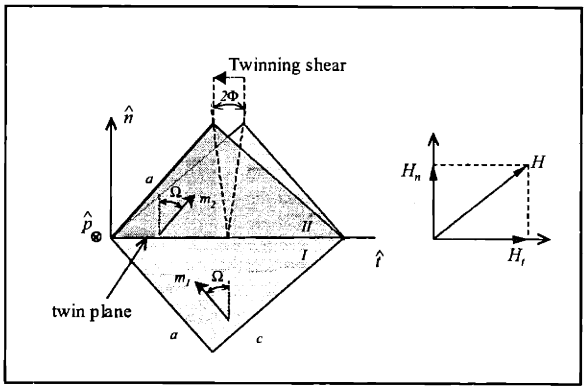

Figure D-1: Geometry of the twin variants considered in the model. The unit cell is tetragonal, with sides a and c. The inclination of the magnetization with respect to the twin plane (of normal $\hat{n}$) is given by Ω. Φ is the angle between the second invariant planes of the twin system, and determine the transformation strain ϵ_o. Plotted also are the projections of the magnetic field along $\hat{n}$ and the twinning direction $\hat{t}$.

where $\epsilon_0 = Tan\,\Phi$ is the twinning shear, see Fig. D-1.

Not explicitly considered in this expression are the forces that pin 180^o domains. Indeed, opposing 180^o domains yield cancelling contributions to the average strain. 180^o domain walls will move along *hatt* until a single domain covers both twin variants, provided that the driving force to do so overcomes the coercivity. This condition is expressed for the free energy change Δg_{dwm} of such a process as $\Delta g_{dwm} = -2\cos\Omega\ M_s H_n < \cos\Omega\ M_s H_c$, where H_n is the component of the field along $\hat{n}$, and H_c measures the coercivity.

It is convenient to define $\mathrm{H} = H\hat{z}$ in a reference frame $\mathcal{S}$. The orientation of $\hat{t}$ and $\hat{n}$ (and thus, the crystal) with respect to $\mathcal{S}$ requires three parameters. Euler angles $\{\phi, \theta, \psi\}$ are chosen. With this a rotation matrix $U_{\phi,\theta,\psi}$ is constructed, which functions as base-change matrix between $\mathcal{S}$ and $\hat{t}\hat{p}\hat{n}$. Thus the average strain is computed for a given orientation distribution (ie. texture) $\mathcal{T}(\phi, \theta, \psi)$ from the sum over all possible orientations $\{\phi, \theta, \psi\}$ as

$$\langle \boldsymbol{\epsilon}^{(r)} \rangle = \int_0^{\pi}\int_0^{\pi}\int_0^{2\pi} \mathcal{T}(\phi,\theta,\psi)\boldsymbol{\epsilon}^{(r)}(H,\phi,\theta,\psi)d\phi d\theta d\psi \qquad \text{(D.1)}$$

using $\boldsymbol{\epsilon}^{(r)}(\mathbf{H},\phi,\theta,\psi) = \mathbf{U}^{\dagger}_{\phi\theta\psi}\cdot\boldsymbol{\epsilon}^{(c)}(\Delta x(\mathbf{U}_{\phi\theta\psi}\cdot\mathbf{H}))\cdot\mathbf{U}_{\phi\theta\psi}$.

The net magnetization $\boldsymbol{m}$ lies along $\hat{n}$ initially, but acquires an extra component

along $\hat{t}$ when $\Delta x \neq 0$. (Note that the component along $\hat{n}$ is constant for all Δx.) It is computed in a manner analogous to eq. (D.1).

D.3 Results and Discussion

With this framework three different orientation distributions are explored and compared to the model results for the single crystal, single 180°-domain actuation, $\Delta x\, \epsilon_0$.

D.3.1 Common Twin Plane Normal

This texture could be expected from ferromagnetic shape memory alloy particles embedded in a soft binder that were aligned with a field prior to curing the binder. Choosing $\phi = 0$ without loss of generality, the orientation distribution is written as $\mathcal{T}^{(n)} = \frac{1}{\pi}\delta(\phi)\delta(\theta - \theta_n)$, where θ_n is the angle between $\hat{n}$ and H. The result can be seen in Fig. D-2.

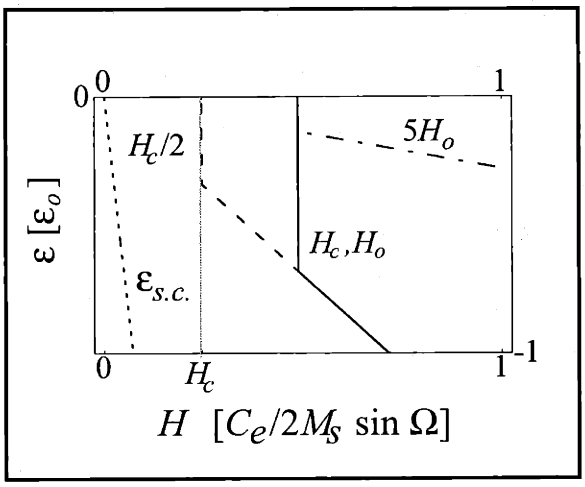

Figure D-2: Principal strain along the field (in units of the transformation strain ϵ_o) as a function of the applied field (in units of the normalization field $C\epsilon_o/(M_s \sin\Omega)$) - solid line - for the texture with constant inclination of the twin plane normal. The dotted line is the strain for a single crystal, single 180°-domain with optimal orientation. Indicated are also the results for smaller coercivity and smaller normalization field.

The principal strains are thus 0 and $\pm\frac{1}{2}h\sin\theta_n$, where the reduced field h is defined from Δx as $h = H[C\epsilon_o/(M_s \sin\Omega)]^{-1}$. The non-zero values of the strain act

on the plane spanned by $\hat{n}$ and $\hat{z}$. The compression axis subtends an angle $\pi/4 - \theta_n$ with the field, and is thus closer to it than the elongation axis, which subtends an angle of $3\pi/4 - \theta_n$. Most notably, the strain than can be achieved is as high as 50% of that of a single crystal in optimal alignment. Best performance is obtained when the field is perpendicular to the twin plane normal except for a component that causes 180 degree domain walls to move. It is also seen that because all the crystals have the same twin plane normal, removal of domain walls occurs at the same threshold field. The result is a sudden motion of the twin-boundaries to the equilibrium volume fraction once that field is reached. Beyond that, the strain is linear with the field.

D.3.2 Common Inclination of Twin Plane Normal

In this case, the angle θ between the field and $\hat{n}$ of the grains is equal to θ_0. This texture could arise in polycrystals subjected to compressive loads. The orientation distribution has the form $\mathcal{T}^{(\theta)} = \frac{1}{2\pi^2}\delta(\theta - \theta_0)$. The principal strain is $-h\cos\theta\sin^2\theta$ (compressive) along the field direction and uniformly tensile in the plane perpendicular to it.

Notably, this texture has an upper bound to the strain that is as large as 38% of the single-crystalline strain for optimum choice of θ ($\theta = \arccos(1/\sqrt{3}) \simeq 55^o$. The result can be seen in Fig. D-3.

A discontinuous threshold-like behavior arises because the component of the field along the twin plane normals is the same for all crystallites, and hence removal of 180^o domain degeneracy occurs simultaneously.

D.3.3 Uniform distribution of orientations

A typical polycrystal or powder composite might have this orientation distribution. $\mathcal{T}^{(u)}(\phi,\theta,\psi) = 1/2\,\pi^3$. The resulting principal strains are compressive in the direction of the field: $-\frac{2}{3\pi}h\sin^3\theta_c$, where $\cos\theta_c \equiv H_c/H$ accounts for the fact that only a fraction of the crystallites is oriented so as to select a single 180^o domain and thus contribute to the strain. In the plane perpendicular to the field the strain is tensile,

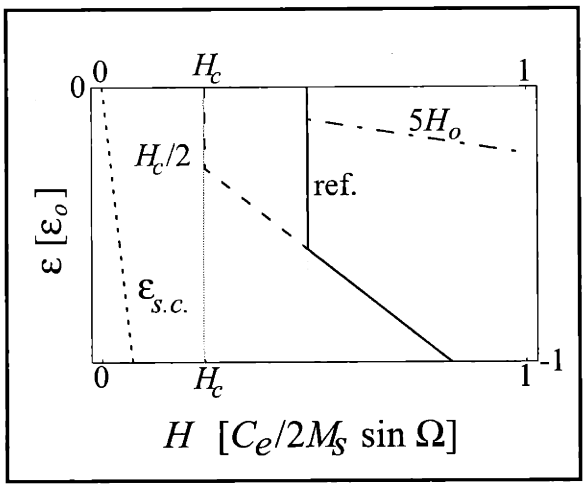

Figure D-3: Principal strain along the field (in units of the transformation strain ϵ_o) as a function of the applied field (in units of the normalization field $C\epsilon_o/(M_s \sin \Omega)$) - solid line - for the texture with common twin plane normal. The dotted line is the strain for a single crystal, single 180°-domain with optimal orientation. Indicated are also the results for smaller coercivity and smaller normalization field.

$\frac{1}{3\pi} h \sin^3 \theta_c$.

Figure D-4 shows a plot of the principal strain along the field direction as a function of the reduced field h, in units of the normalization field $H_o = C\epsilon_o/(M_s \sin \Omega)$. It can be seen that for small fields, the coercivity is not overcome and the material does not strain. As the field increases, for some crystallites the projection of H_n will become large enough to remove their 180°-domain walls. These crystallites then strain an amount proportional to H_t.

The actuation strain is smaller than in single crystals because not all the crystallites are optimally oriented. At best $2/3\pi \simeq 21\%$ of the strain of an optimally oriented single-crystal can be obtained.

D.4 Conclusions

An analytical model for the magneto-elastic response of an arrangement of ferromagnetic shape memory alloys to an applied field has been developed. It was used to compute an upper bound to the strain of several textures of poly-crystal arrangements. It was found that arrangements with common twin plane normal, such as

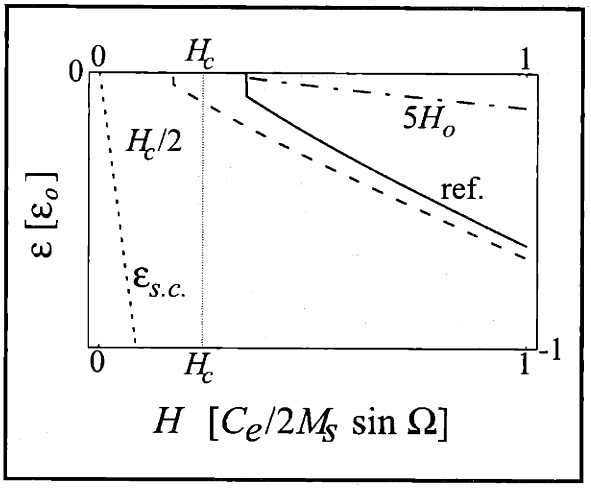

Figure D-4: Principal strain along the field (in units of the transformation strain ϵ_o) as a function of the applied field (in units of the normalization field $C\epsilon_o/(M_s \sin \Omega)$) - solid line - for the texture with uniform distribution of orientations. The dotted line is the strain for a single crystal, single 180°-domain with optimal orientation. Indicated are also the results for smaller coercivity and smaller normalization field.

could be expected for powder composites with magnetically aligned powder, up to 50% of the single crystal strain could be achieved (not including the filling fraction). For textures with unique twin plane normal inclination, to be found for instance in FSMAs cooled under load, the upper bound is 35%, and a uniform distribution yields up to 21% of the single-crystalline result. In all cases the strain is compressive in the direction of the field.

Bibliography

[1] P. J. Webster. Heusler alloys. *Contemp. Phys.*, 10:559–577, 1969.

[2] R. W. Overholser, M. Wuttig, and D. A. Neumann. Chemical ordering in Ni–Mn–Ga heusler alloys. *Scripta Mater.*, 40:1095–1102, 1999.

[3] A. D. Boshko, A. N. Vasil'ev, V. V. Khovailo, I. E. Dikshtein, V. V. Koledov, S. M. Seletskii, A. A. Tulaikova, A. A. Cherechukin, V. G. Shavrov, and V. D. Bushel'nikov. Magnetic and structural phase transitions in the shape memory ferromagnetic alloys $Ni_{2+x}Mn_{1-x}Ga$. *J. Exp. and Theor. Phys.*, 88:954–962, 1999.

[4] R. C. O'Handley. *Modern Magnetic Materials*, chapter 3, page 99. John Wiley & Sons, Inc., 2000.

[5] R. M. Bozorth. *The Theory of Transformations in Metals and Alloys.* D. Van Nostrand Company, New York, 1 edition, 1951.

[6] J. Soltys. The magnetic properties of the heusler alloy Ni_2MnGa. *Acta Phys. Polonica*, A46:383–384, 1974.

[7] A. Ayuela, J. Enkovaara, K. Ullakko, and R. M. Nieminen. Structural properties of magnetic heusler alloys. *J. Phys. Condens. Matter*, 11:2017–2026, 1999.

[8] S. Wirth, A. Leithe-Jasper, A. N. Vasil'ev, and J. M. D. Coey. Structural and magnetic properties of Ni_2MnGa. *J. Magn. Mag. Mat*, 167:L7–L11, 1997.

[9] V. A. Chernenko, A. Amengual, E. Cesari, V. V. Kokorin, and I. K. Zasimchuk. Thermal and magnetic properties of stress-induced martensites in Ni–Mn–Ga alloys. *Acta Mat.*, 5 (C2):95–98, J. de Physique IV.

[10] V. A. Chernenko, C. Segui, E. Cesari, J. Pons, and V. V. Kokorin. Sequence of martensitic transformations in Ni–Mn–Ga alloys. *Phys. Rev. B*, 57:2659–2662, 1998.

[11] L. Mañosa, A. G. Comas, E. Obradó, and A. Planes. Premartensitic phase transformation in the Ni_2MnGa shape memory alloy. *Mat. Sci. Eng. A*, 273-276:329–332, 1999.

[12] A. Gonzalez-Comas, E. Obradó, L. Mañosa, and A. Planes. Premartensitic and martensitic phase transitions in ferromagnetic Ni_2MnGa. *Phys. Rev. B*, 60:7085–7090, 1999.

[13] B. Wedel, M. Suzuki, Y. Murakami, C. Wedel, T. Suzuki, D. Shindo, and K. Itagaki. Low temperature crystal structure of Ni–Mn–Ga alloys. *J. Alloys and Comp.*, 290:137–143, 1999.

[14] V. A. Chernenko, J. Pons, C. Seguí, and E. Cesari. Premartensitic phenomena and other phase transformations in Ni–Mn–Ga alloys studies by dynamical mechanical analysis and electron diffraction. *Acta Mat.*, 50:53–60, 2002.

[15] A. Planes, E. Obradó, A. González-Comas, and L. Mañosa. Premartensitic transition driven by magnetoelastic interaction in bcc ferromagnetic Ni_2MnGa. *Phys. Rev. Lett.*, 79(20):3926 – 3929, 1997.

[16] V. V. Kokorin and M. Wuttig. Magnetostriction in ferromagnetic shape memory alloys. *J. Magn. Mag. Mat*, 234:25–30, 2001.

[17] I. K. Zasimchuk, V. V. Kokorin, V. V. Martynov, A. V. Tkachenko, and V. A. Chernenko. Crystal structure of martensite in heusler alloy Ni_2MnGa. *Phys. Met. Metall.*, 69:104–108, 1990.

[18] V. V. Martynov and V. V. Kokorin. The crystal structure of thermally- and stress-induced martensites in Ni_2MnGa single crystals. *J. Phys. III*, 2:739–749, 1992.

[19] K. Ullakko, J. K. Huang, V. V. Kokorin, and R. C. O'Handley. Magnetically controlled shape memory effect in Ni_2MnGa intermetallics. *Scripta Mater.*, 36:1133–1138, 1997.

[20] M. Matsumoto, T. Tagaki, J. Tani, T. Kanomata, N. Muramatsu, and A. N. Vasil'ev. Phase transformations of heulser type $Ni_{2+x}Mn_{1-x}Ga_{(x=0\ 0.19)}$. *Mat. Sci. Eng. A*, 273 - 275:326 – 328, 1999.

[21] A. N. Vasil'ev, A. D. Boshko, V. V. Khovailo, I. E. Dikshtein, V. G. Shavrov, V. D. Bushel'nikov, M. Matsumoto, S. Suzuki, T. Takagi, and J. Tani. Structural and magnetic phase transitions in the shape memory alloys $Ni_{2+x}Mn_{1-x}Ga$. *Phys. Rev. B*, 59:1113–1120, 1999.

[22] C. M. Wayman. *Introduction to the crystallography of martensites.* The Macmillan Company, New York, 1964.

[23] G. B. Olson and W. S. Owen. *Martensite.* ASM International, 1992.

[24] K. Ullakko, P. G. Yakovenko, and V. G. Gavriljuk. New developments in actuator materials as reflected in magnetically controlled shape memory alloys and high-strength shape memory steels. *Smart Structures and Materials*, Proceedings of SPIE Vol. 2715:42 – 50, 1996.

[25] K. Ullakko. Large stroke and high-strength actuator materials for adaptive structures. *Third International Conference on Intelligent Materials*, Proceedings of SPIE Vol. 2779:505 – 510, 1996.

[26] R. D. James and M. Wuttig. Alternative smart materials. *SPIE*, 2715:420–426, 1996.

[27] K. Ullakko. Magnetically controlled shape memory alloys: a new class of actuator materials. *J. Mat. Eng. Perf. (JMEPEG)*, 5:405 – 409, 1996.

[28] K. Ullakko, J. K. Huang, C. Kantner, R. C. O'Handley, and V. V. Kokorin. Large magnetic-field-induced strains in Ni_2MnGa single crystals. *Appl. Phys. Lett.*, 69:1966 – 1968, 1996.

[29] S. J. Murray, M. Farinelli, C. Kantner, J. K. Huang, S. M. Allen, and R. C. O'Handley. Field-induced strain under load in Ni–Mn–Ga magnetic shape memory materials. *J. Appl. Phys.*, 83:7297–7299, 1998.

[30] R. C. O'Handley. Model for strain and magnetization in magnetic shape-memory alloys. *J. Appl. Phys.*, 83:3263–3270, 1998.

[31] R. D. James and M. Wuttig. Magnetostriction of martensite. *Phil. Mag. A*, 77:1273–1299, 1998.

[32] G. H. Wu, C. H. Yu, L. Q. Meng, F. M. Yang, S. R. Qi, W. S. Zhan, Z. Wang, Y. F. Zheng, and L. C. Zhao. Giant magnetic-field-induced strains in Heusler alloy nimnga with modified composition. *Appl. Phys. Lett.*, 75:2990–2992, 1999.

[33] R. Tickle, R. D. James, T. Shield, M. Wuttig, and V. V. Kokorin. Ferromagnetic shape memory in the nimnga system. *IEEE Magn. Trans.*, 35:4303–4310, 1999.

[34] R. D. James, R. Tickle, and M. Wuttig. Large field-induced strains in ferromagnetic shape memory materials. *Mat. Sci. Eng. A*, 273-275:320–325, 1999.

[35] R. Tickle and R. D. James. Magnetic and magnetomechanical properties of Ni_2MnGa. *J. Magn. Mag. Mat*, 195:627–638, 1999.

[36] O. Heczko, A. Sozinov, and K. Ullakko. Giant field-induced reversible linear strain in magnetic shape memory nimnga at roomt temperature. In *INTERMAG 2000 Digest of Technical Papers. IEEE Trans. Mag.*, Toronto, 2000.

[37] O. Heczko, A. Sozinov, and K. Ullakko. Giant field-induced reversible strain in magnetic shape memory nimnga alloy. *IEEE Magn. Trans.*, 36:3266–3268, 2000.

[38] S. J. Murray, M. A. Marioni, A. M. Kukla, J. Robinson, R. C. O'Handley, and S. M. Allen. Large field-induced strain in single crystalline Ni–Mn–Ga ferromagnetic shape memory alloy. *J. Appl. Phys.*, 87:5774–5776, 2000.

[39] S. J. Murray, M. A. Marioni, S. M. Allen, R. C. O'Handley, and T. A. Lograsso. 6% magnetic-field-induced strain by twin-boundary motion in ferromagnetic Ni–Mn–Ga. *Appl. Phys. Lett.*, 77:886–888, 2000.

[40] S. J. Murray, M. Marioni, P. G. Tello, S. M. Allen, and R. C. O'Handley. Giant magnetic-field-induced strain in Ni–Mn–Ga crystals: experimental results and modeling. *J. Magn. Mag. Mat*, 226:945–947, 2001.

[41] A. Sozinov, A. A. Likhachev, N. Lanska, K. Ullakko, and V. K. Lindroos. Crystal structure, magnetic anisotropy and mechanical properties of seven-layered martensite in Ni–Mn–Ga. In *Smart Structures and Materials*, volume Proceedings of SPIE Vol. 4699, pages 195 – 205, 2002.

[42] A. Sozinov, A. A. Likhachev, N. Lanska, and K. Ullakko. Giant magnetic-field-induced strain in nimnga seven-layered martensitic phase. *Appl. Phys. Lett.*, 80:1746 – 1748, 2002.

[43] C. P. Henry, J. Feuchtwanger, D. Bono, M. A. Marioni, P. G. Tello, M. Richard, S. M. Allen, and R. C. O'Handley. Ac performance and modelling of ferromagnetic shape memory actuators. In *Smart Structures and Materials*, volume Proceedings of SPIE Vol. 4333, pages 151–162, 2001.

[44] I. Suorsa, J. Tellinen, E. Pagounis, I. Aaltio, and K. Ullakko. Applications of magnetic shape memory actuators. In *Int. Conf. New Actuators*, volume A5.2, pages 158 – 161, 2002.

[45] J. Tellinen, I. Suorsa, A. Jääskeläinen, I. Aaltio, and K. Ullakko. Basic properties of magnetic shape memory actuators. In *Int. Conf. New Actuators*, volume P44, pages 566 – 569, 2002.

[46] F. Claeyssen and N. Lhermet. Actuators based on giant magnetostrictive materials. In *Int. Conf. New Actuators*, volume A5.0, pages 148 – 153, 2002.

[47] N. I. Glavatska, A. A. Rudenko, and V. A. L'vov. Time-dependent magnetostrain effect and stress relaxation in the martensitic phase of Ni–Mn–Ga. *J. Magn. Magn. Mater.*, 241:187–291, 2002.

[48] C. P. Henry. *Dynamic Actuation Properties of Ni–Mn–Ga Ferromagnetic Shape Memory Alloys.* PhD thesis, M.I.T., Cambridge, MA, May 2002.

[49] P. J. Ferreira, J. B. Vander Sande, M.A. Fortes, and A. Kyrolainen. Microstructure development during high-velocity deformation. *Materials and Metallurgical Transactions. A*, to be submitted.

[50] J. Soltys. The effect of heat treatment on the atomic arrangement and the magnetic properties in Ni_2MnGa. *Acta Phys. Polonica*, A47:521–523, 1975.

[51] X. Jin, M. A. Marioni, D. Bono, S. M. Allen, R. C. O'Handley, and T. Y. Hsu. Empirical mapping of ni-mn-ga properties with composition and valence electron concentration. *J. Appl. Phys.*, 91(10):8222 – 8224, 2002.

[52] A. N. Vasil'ev, A. Kaiper, V.V. Kokorin, V. A. Chernenko, T. Takagi, and J. Tani. Structural phase transitions induced in Ni_2MnGa by low-temperature uniaxial compression. *JETP. Lett*, 58:306–309, 1993.

[53] S. Y. Chu, A. Cramb, M. De Graef, D. Laughlin, and M. E. McHenry. The effect of field cooling and field orientation on the martensitic phase transformation of Ni_2MnGa single crystal. *J. Appl. Phys.*, 87:0, 2000.

[54] T. McClure. Private communication. MIT, 1999.

[55] J. Pons, C. Seguí, V. A. Chernenko, E. Cesari, P. Ochin, and R. Portier. Transformation and ageing behaviour of melt-spun Ni–Mn–Ga shape memory alloys. *Mat. Sci. Eng. A*, 273-275:315–319, 1999.

[56] W. H. Wang, Z. H. Liu, J. Zhang, J. L. Cheng, G. H. Wu, W. S. Zhan, T. S. Chin, G. H. Wen, and X. X. Zhang. Thermoelastic intermartensitic trasnformation and

its internal stress dependency in $Ni_{52}Mn_{24}Ga_{24}$. *Phys. Rev. B*, 66:052411–1 – 4, 2002.

[57] A. A. Likhachev and K. Ullakko. Quantitative model of large magnetostrain effect in ferromagnetic shape memory alloys. *EPJdirect B2*, pages 1–9, 1999.

[58] R. C. O'Handley, S. J. Murray, M. A. Marioni, H. Nembach, and S. M. Allen. Phenomenology of giant magnetic-field-induced strain in ferromagnetic shape-memory materials. *J. Appl. Phys.*, 87:4712–4717, 2000.

[59] F. W. Grover. *Miscellaneous pamphlets on inductance.* Govt. Print. Off., Washington, 1920.

[60] C. P. Henry, J. Feuchtwanger, D. Bono, M. A. Marioni, P. G. Tello, M. Richard, S. M. Allen, and R. C. O'Handley. AC performance and modeling of ferromagnetic shape memory actuators. In *Smart Structures and Materials 2001*, volume SPIE 4333, pages 151–161, Newport Beach, USA, 2001.

[61] S. J. Murray. *Magneto-mechanical properties and applications of Ni–Mn–Ga ferromagnetic shape memory alloy.* PhD thesis, M.I.T., Cambridge, MA, January 2000.

[62] J. D. Jackson. *Classical Electrodynamics.* John Wiley & Sons, Inc., New York, 2 edition, 1962,1975.

[63] P. J. Ferreira and J. B. Vander Sande. Magnetic field effects on twin dislocations. *Scripta Mater.*, 41:117–123, 1999.

[64] W. G. Johnston and J. J. Gilman. Dislocation velocities, dislocation densities, and plastic flow in lithium fluoride crystals. *J. Appl. Phys.*, 30:129–137, 1959.

[65] R. E. Reed-Hill and R. Abbaschian. *Physical Metallurgy Principles.* PWS Publishing Company, Boston, 3 edition, 1994.

[66] W. Frank. Dislocation dynamics in the presence of a multiple spectrum of thermally surmountable barriers. In *Fundamental Aspects of Dislocation Theory*, volume II, pages 1065–1076, 1969.

[67] E. Pagounis. Private communication. Adaptamat — Helsinki, 2002.

[68] M. Pasquale, C. Sasso, S. Besseghimi, F. Passaretti, E. Villa, and A. Sciacca. Nimnga polycrystalline magnetically activated shape memory alloys. *IEEE Magn. Trans.*, 36:3263 –3265, 2000.

[69] K. Ullakko, Y. Ezer, A. Sozinov, G. Kimmel, P. Yakovenko, and V. K. Lindroos. Magnetic-field-induced strains in polycrystalline Ni–Mn–Ga at room temperature. *Scripta Mater.*, 44:475–480, 2001.

[70] K. Bhattacharya and R. V. Kohn. Symmetry, texture and the recoverable strain of shape-memory polycrystals. *Acta Mater.*, 44:529–542, 1996.

[71] M. A. Marioni, S. M. Allen, and R. C. O'Handley. Analytical model for field-induced strain in ferromagnetic shape-memory alloy polycrystals. *J. Appl. Phys.*, 91:7807–7809, 2002.

[72] J. Feuchtwanger, S. Michael, J. K. Huang, D. Bono, R. C. O'Handley, S. M. Allen, K. Jenkins, J. Goldie, and A. Berkowitz. Energy absorption in Ni–Mn–Ga polymer composites. *J. Appl. Phys.*, 93(10):in press, 2003.

[73] J. Feuchtwanger, K. Griffin, J. K. Huang, R. C. O'Handley, S. M. Allen, and D. Bono. Vibration damping in Ni–Mn–Ga-polymer composites. In *Smart Structures and Materials*, volume Proceedings of SPIE SS/NDA, page in press, 2003.

[74] J. Feuchtwanger, K. Griffin, J. K. Huang, D. Bono, R. C. O'Handley, and S. M. Allen. Mechanical energy absorption in Ni–Mn–Ga polymer composites. *J. Magn. Magn. Mat.*, submitted April 2003.

[75] C. P. Sasso, M. Pasquale, G. Bertotti, V. A. L'vov, and V. A. Chernenko. Temperature dependence of mechanical and magnetic curves in Ni_2MnGa single crystals. *IEEE Trans. Magn.*, DA 03:1–3, 2003.

[76] N. Glavatska, G. Mogylny, I. Glavatsky, A. Tyshchenko, O. Söderberg, and V.K. Lindroos. Temperature dependence of magnetic shape memory effect and martensitic structure in Ni–Mn–Ga alloy. In *Proc. of Conference on Shape Memory Materials and Superelastic Technologies and Shape Memory Materials (SMST-SMM-2001)*, volume Materials Science Forum 394-395, pages 537–540, 2002.

[77] R. C. O'Handley, D. I. Paul, M. A. Marioni, C. P. Henry, M. Richard, P. G. Tello, and S. M. Allen. Field-induced strain in ferromagnetic shape memory actuators: from macroscopic to microscopic models. In *The Fourth Pacific Rim International Conference on Advanced Materials and Processing*, volume PRICM4, pages 2945–2948, 2001.

[78] M. A. Marioni. Magnetic materials, course project. MIT, May 2000.

[79] M. Wuttig, K. Tsuchiya, L. Liu, , and R. James. Occurrence of ferromagnetic shape memory alloys. *J. Appl. Phys.*, 87:4707–4711, 2000.

[80] E. J. Rothwell and M. J. Cloud. *Electromagnetics*, chapter 2, page 94. CRC Press, 2001.

[81] M. Volmer and A. Weber. *Z. Phys. Chem.*, 119:227, 1926.

[82] R. Becker and W. Döring. *Ann. Phys.*, 24:719, 1935.

[83] J. W. Christian. *The Theory of Transformations in Metals and Alloys*, chapter 10. Pergamon Press, Oxford, 2 edition, 1975.

[84] J. P. Hirth and J. Lothe. *Theory of Dislocations*, chapter 6, page 169. John Wiley & Sons, Inc., 2 edition, 1982.

[85] J. Blin. *Acta Met.*, 3:199, 1955.

[86] C. B. Carter and S. M. Holmes. *Phil. Mag.*, 35:1161, 1977.

[87] L. E. Murr. *Interfacial Phenomena in Metals and Alloys.* Adison-Wesley, Reading, MA, 1975.

[88] J. P. Hirth and J. Lothe. *Theory of Dislocations*, chapter 15, page 532. John Wiley & Sons, Inc., 2 edition, 1982.

[89] P. J. Webster, K. R. A. Ziebeck, and M. S. Peak. *Phil. Mag. B*, 49:295, 1984.

[90] D. I. Paul. Colloquium, magnetic materials group. MIT, April 2003.

[91] W. de Rosset and A. V. Granato. Dislocation dynamics in the presence of a multiple spectrum of thermally surmountable barriers. In *Fundamental Aspects of Dislocation Theory*, volume II, pages 1099–1106, 1969.

[92] W. A. Johnson and R. F. Mehl. *Trans. AIME*, 135:416, 1939.

[93] John Cahn. The time cone method for nucleation and growth kinetics on a finite domain. In *Mat. Res. Soc. Symp. Proc.*, volume 398, pages 425–438, 1996.

[94] R. D. James and D. Kinderlehrer. Theory of magnetostriction with applications to $Tb_xDy_{1-x}Fe_2$. *Phil. Mag. B*, 68:237 – 274, 1993.